Experimental Study of the Aerodynamics of a Horizontal Axis Wind Turbine

A thesis submitted to the Universitat Politècnica de Catalunya
for the degree of Doctor of Philosophy in the
Escola Tècnica Superior d'Enginyeries Industrial i Aeronàutica de Terrassa

Vanessa del Campo Gatell

January, 2013

Universitat Politècnica de Catalunya (UPC)

Experimental Study of the Aerodynamics

of a Horizontal Axis Wind Turbine

Author
Vanessa del Campo Gatell
Aerospace Engineer

UPC Tutor
Jasmina Casals Terré
Doctor Mechanical Engineer

Director
Francisco Javier Díez Garias
Doctor Aerospace Engineer

Pero la Historia no admite vacíos: imparable la Vida los llena. Todo ocaso ofrece una ocasión. [...]

Este ocaso es el momento de la acción entre todos porque otro mundo no sólo es posible, es seguro. Si mejor o peor, dependerá de nuestra reacción. Mi mensaje a los jóvenes es que ha llegado el momento de cambiar el rumbo de la nave. Aunque sus líderes sigan en el puesto de mando y al timón, aunque desde allí sigan dando órdenes anacrónicas, los jóvenes puestos al remo pueden dirigir la nave. Sólo necesitan unirse y acordar que a una banda boguen hacia delante mientras en la otra cíen hacia atrás y el barco girará en redondo, poniendo proa hacia un desarrollo humano.

(Debajo de la alfombra, José Luis Sampedro.)

Acknowledgements

Last four years would not have been the same without the people I met...the people that crossed my way and left it full of colours, feelings, ideas, surprises, hugs and smiles. I would like to make use of this yet white page to thank them all...

First of all, I would like to thank my thesis director, Javier Diez, for supporting and guiding me during all this time. He was always there to encourage me when doubts were blocking me. Besides, I would like to give my special thanks to Jaume Gibert, founder of the Aerospace Department at ETSEIAT, who believed in me from the very beginning, and convinced me to try and mix research with a good sense of optimism.

During all this PhD time I have been working at the Escola Tècnica Superior d'Enginyeries Industrial i Aeronàutica de Terrassa, in Barcelona. This is a small Engineering School where one can still feel the passion for teaching and researching. I would like to thank all the people who make this possible everyday, in special Eulalia Griful, the School director, Jasmina Casals, the Research subdirector and Miguel Mudarra, the Aerospace Department coordinator. Thanks to Roberto Castilla and Esteve Codina, from the Fluid Mechanics Department, who oriented and supported my research with their advices during all these years. Thanks to Beatriz Amante and Iria Fraga too, my first friends at ETSEIAT, and to Gisela Detrell, a new department discovery! Thanks to Jordi Font for his art, to Enrique Ortega for his inventiveness, to Lourdes Rondón and Mireia Sala for their yogie peace...All my acknowledgments to my best friends Miquel Sureda and David del Campo, with whom I have the luck of sharing the office: working with you is just like meeting good friends and have a good time, and it is wonderful to feel that everyday... I love you guys!!

And now I will cross the Atlantic and remember my stay at the Mechanical & Aerospace Laboratory at Rutgers University, in New Jersey... My acknowledgment to all the big team there, and specially to my great friends Marita Torregrosa and Ye Cheng. They taught me how to survive in a laboratory (not easy) and have fun with it! Thanks for all the great moments of those Jersey summers....a special dedication to Marc Prat, who never hesitated to leave the lab tools and take a train to go and listen to jazz in a small New Yorker bar...I will never forget your smiling eyes!

Another part of the experiments were done at the Aerodynamics Department at TUDelft, in Delft. Thanks to all the staff, and specially, thanks to Bas van Oudheusden, Fulvio Scarano and Carlos Simao Ferreira, the professors who gave me the opportunity of collaborating with this prestigious and efficient team. I certainly learnt a good deal. Thanks to all the guys at the Department too, who brought laughs and warmth to that rainy summer, special thanks to my brasilian friends Artur Palha and Daniele Ragni.

And thinking of cold weather...I could not go on without mentioning the marvelous snowy weeks spent at the HZDR, in Dresden, where I had the opportunity of working and learning

with Thomas Albrecht, a great friend and best phd-quasi-tutor. Thanks for helping me with so much patience...and for being so exigent with work, you definitely had to be German! Thanks to Tom Weier for inviting me to visit their Research Center.

Finally, thanks to all the friends that, although not directly related with my working places, supported me during all these years, making my days funnier, brighter...and so much more interesting. Many times I was asked, do I prefer Madrid or Barcelona? And honestly, I think of Madrid and my heart melts a bit...it is quite addictive, so many great people inside!!! Thanks to Gabriela Rubio, Esther Contreras, Ana Sierra and Paula Calle, for growing with me; I love exploring life with you girls!!!...Thanks to my little beloved Buddha Eduardo Rodriguez. Thanks to the people I met traveling around the world during this years...Alexandra Estévez, Paz Díaz, Urupagua Villegas, Christian Holtkötter...you were the best of my trips!. Thanks to Rubén Yessayan...your Debussy helped me during so many hours spent in front of the computer! Thanks to the great people I met studying Aerospace Engineering: Ignacio Pardo, Elena Garcia, Inés Fuente, Nora Álvarez, Carlos García and Sergio Nieto. You made my university days unforgettable, and that is quite an honor, given the fact that I forgot almost all the equations we studied!! (in case you are going to continue reading, just wanted to clarify that luckily I didn't forget the momentum equation...). Thanks to the great friends I found in Barcelona, Mark Schuback, Lara Iaconi, Narayan Bulusi, Eva García, Luce Prignano, Jesús García, Ares Gabàs, Blanca Munarriz, Ana Bracons, Mayte Rodriguez, Joan Martínez, Noelia Rey, Nela Fraga and José Parrón. Thanks and thanks and thanks to all for making me smile and give me love when I had to visit the hospital more often than wanted this last year...and above all, thanks for turning this beautiful city into a warm beautiful city. Thanks to the magic animals that live in the forest of the senses in Montjuic too, for providing with experiences of the essential that make me see that I am a big question whose answer I don't know, or better, I think I don't know...

I love you all my friends, thanks for all the distractions that contributed to my taking longer to finish this PhD thesis, it wouldn't have been worth without them! Thanks for making me realize the world is very big, and this thesis very small.

This work is dedicated with all my love to my parents, Paz Gatell and Juan Carlos del Campo, and my three grandmothers, Consuelo López, Domitila Méndez and Ángeles Gatell. I owe them everything. Thanks for their patience, their love and their generous support of this crazy creature.

Journal Publications and Conferences

V. del Campo, D. Ragni, D. Micallef, B. Akay, J. Diez, C. Simao Ferreira. *3D Load Calculation on a Horizontal Axis Wind Turbine using PIV.* Wind Energy. Under review.

V. del Campo, D. Ragni, D. Micallef, B. Akay, J. Diez, C. Simao Ferreira. *Non-intrusive 3D load calculation during yaw conditions.* EWEA Wind Energy Event. Accepted for presentation in Vienna 2013.

V. del Campo, D. Ragni, D. Micallef, B. Akay, J. Diez, C. Simao Ferreira. *3D Aerodynamic Load Calculation on a Horizontal Axis Wind Turbine using PIV.* Euromech Colloquium 528, Wind Energy and the impact of turbulence on the conversion process. Presented in Oldenburg 2012.

T. Albrecht, V. del Campo, T. Weier and G. Gerbeth. *Comparison of PIV-based methods for airfoil loads evaluation.*16th International Symposion on Applications of Laser Techniques to Fluid Mechanics. Presented in Lisbon 2012.

V. del Campo, A. Villegas, Y. Cheng, F. J. Diez. *Characterization of Low Reynolds Number Wind Turbine Aerodynamics by BEM Theory and PIV Measurements.* ASME: 3rd Joint US-European Fluids Engineering Summer Meeting. Presented in Montreal 2010.

Abstract

One of the challenges of the wind energy community today is to improve the existing background on the aerodynamic phenomena of a Horizontal Axis Wind Turbine (HAWT), the prediction of the wind speed distribution on the rotor plane, and the estimation of the design loads. This dissertation aims at contributing to the fulfillment of these objectives.

In this way, this study assessed the feasibility of measuring the loads exerted on a HAWT blade by means of Stereoscopic Particle Image Velocimetry (SPIV), which is a non intrusive technique that provides with the whole 3D velocity field in a plane. Thus, with this PIV-Loads method, the velocity and pressure fields, as well as the resultant aerodynamic forces around a section of the blade, would be available simultaneously, without the need of modifying the model or disturbing the flow.

In order to achieve this goal progressively, the PIV-Loads method, based in a Momentum Equation contour-based approach, was firstly validated using DNS data, both for a laminar unsteady flow case, as for a velocity averaged turbulent flow. Secondly, the method was tested in the wind tunnel with a bidimensional problem, measuring forces in a stationary flat plate, for different angles of attack (that provided laminar and turbulent flow conditions). Finally, the PIV-Loads method was applied to a HAWT model working both in axial and yaw flow conditions, measuring forces on a rotating blade for steady and unsteady cases. Bringing the project to completion, the near vortex wake of a HAWT was characterized by means of Time Resolved PIV.

Regarding the PIV-Loads methodology, load predictions are more reliable if the integration path does not cross a shear layer or a boundary layer. In addition, it is neither recommended to neglect the third velocity component when measuring forces on a rotating HAWT blade, nor to eliminate the velocity fluctuation terms when dealing with turbulent flows.

All implemented codes and experimental results were validated or compared with numerical or experimental alternative data. The conclusion is that the PIV-Loads method provides with precise results if the available velocity data is sufficiently accurate. Furthermore, the force results obtained with standard PIV equipments showed good agreement and consistency with the results provided by a balance and a panel method code, among others. However, any PIV errors such as lack of resolution, velocity gradients inside the interrogation window or laser reflections, may lead to uncertainties in the load measurements. Any future improvement in this sense will certainly lead to better results.

Contents

List of Figures

List of Tables

Nomenclature

Roman Symbols

f	Frequency
M	Mach number
$\mathrm{Re_x}$	Local Reynolds number
Re	Reynolds number
St	Strouhal number
$\vec{a}$	Flow acceleration
$\vec{n}$	Normal unit vector
a	Axial induction factor
a'	Tangential induction factor
A_d	Rotor disk area
B	Number of blades
b	Span length
c	Chord
C_d	Drag coefficient
C_l	Lift coefficient
C_n	Normal force coefficient
C_P	Power coefficient
C_T	Thrust coefficient
C_t	Tangential force coefficient
CC	Cross-correlation value
d	Drag
d_τ	Partilce image diameter
D_p	Particle diameter

e	Thickness
F	Force
f	Prandtl's correction factor
$f^\sharp$	Diaphragm aperture
F_n	Normal force
F_t	Tangential force
f_h	Prandtl's hub correction factor
f_l	Focal length
f_m	Mass force
f_t	Prandtl's tip correction factor
I	Turbulence intensity
I_g	Grey intensity value
l	Lift
M	Torque
N	Number of samples
P	Power
p	Pressure
p_∞	Free stream pressure
p_d^+	Pressure at the rotor disk (upstream)
p_d^-	Pressure at the rotor disk (downstream)
p_t	Total pressure
q	Mie's normalized diameter
R	Rotor radius
r	Distance to the rotation axis (radius)
R_h	Hub radius
s	Surface
T	Thrust
t	Time
u', v', w'	Velocity fluctuations in x,y,z axis, respectively
u, v, w	Velocities in x,y,z axis, respectively

V	Flow velocity
V_∞	Free stream velocity
V_d	Axial velocity at the rotor disk
V_{lag}	Particle velocity lag
V_p	Particle velocity
V_{rmse}	Velocity turbulence strength
V_r	Relative Velocity
V_w	Axial velocity at the wake
x, y, z	Spatial coordinates

Greek Symbols

α	Angle of attack
β	Angle between the chord of the blade and the rotor plane
ϵ	Displacement error
λ	Light wavelength
λ_{sr90}	Minimum resolved structure
μ	Dinamic viscosity coefficient
Ω	Angular velocity
$\overline{\overline{\tau'}}$	Viscous stress tensor
ϕ	Angle between the local velocity and the rotor plane
ρ	Density
ρ_p	Particle density
σ	Standard deviation
σ_r	Solidity factor
θ	Azimuth angle in the rotation plane
υ	Volume
ε_{cc}	Cross-correlation displacement error
ε_{pl}	Peak-locking displacement error

Abbreviations

μPIV	Micro Particle Image Velocimetry
BEM	Blade Element and Momentum

CCD Charge-Coupled Device.

CFD Computational Fluid Dynamics

CMOS Complementary Metal Oxide Semiconductor

DMT Derivative Moment Transformation

DNS Direct Numerical Simulation

EWEA European Wind Energy Association

FOV Field Of View

HAWT Horizontal Axis Wind Turbine

HWA Hot Wire Anemometry

IA Interrogation Area

LDV Laser Doppler Velocimetry

LES Large Eddy Simulation

LIDAR LIght Detection And Ranging

ME Momentum Equation

NREL National Renewable Energy Laboratory

OJF Open Jet Facility

PDF Probability Density Function

PIV Particle Image Velocimetry

RANS Reynolds Averaged Navier-Stokes equations

SPIV Stereoscopic Particle Image Velocimetry

SWT Small Wind Turbine

TR-TOMO PIV Time Resolved Tomographic Particle Image Velocimetry

TRPIV Time Resolved Particle Image Velocimetry

TSR Tip Speed Ratio

VAWT Vertical Axis Wind Turbine

Chapter 1

Introduction

1.1 Wind Energy Technology Trends

During the past 75 years, the wind energy technology has gone through a big evolution, with the aim of designing more efficient turbines, to turn wind energy into electricity. Making a wind turbine is a big challenge that entails meeting the specifications for standard electricity generation, coping with the variability of the wind, and competing economically with other energy sources.

Although nowadays most of the largest wind turbines employ active pitch control, the use of aerodynamic stall to limit power has been a characteristic feature in the history of wind turbine technology. While most aerodynamic devices avoid stall, wind turbines can make purposeful use of stall, as means of limiting power an loads, in case of having high wind speeds. Thus, in an aircraft wing, a large margin between the stall angle of attack and the optimum cruising angle is very desirable, whereas for a wind turbine, this may be undesirable and lead to higher extreme loads.

The components of a wind turbine are subject to highly irregular loading input coming from turbulent wind conditions, and the number of fatigue cycles experienced by the major structural components can be orders of magnitude greater than for other rotating machines. In addition, a wind turbine should operate unattended during a 20 years lifetime.

Thus, wind technology differs from other existing technologies, and has unique research demands, in the use (rather than avoidance) of stall, and in the severity of the fatigue to which the machines are subjected.

In the last decades, significant consolidation of the wind turbines design has taken place, although further diversification has also been introduced. A brief summary of main tendencies is presented herein. Further details can be found in EWEA (2009).

In the beginning, big advantages were expected in the use of vertical axis wind turbines (VAWT), due to their omnidirectionality. However, some serious technical problems, such as metal fatigue-related failures of the curved rotor blades, among others, caused the VAWT design to disappear from the large commercial market. Nevertheless, there has been a remarkable resurgence of innovative VAWT designs recently, in the category of small systems for diverse applications, like rooftops of buildings, offshore applications, etc... As an example, Figure 1.2 shows a photograph of a small VAWT, the QR5, with

Figure 1.1: Lillgrund offshore wind farm (*from www.siemens.com*).

diameter $D = 3$m, and $P = 7$kW.

Small wind turbines (SWT) are used in two main areas: autonomous electrical systems (off-grid), and distributed generation (on-grid). Despite the maturity reached in the development of the large wind turbines, the state of the art for small wind turbines is far from technological maturity; average costs for a small wind turbine vary from 2700 €/kW to 8000 €/kW, while the costs of large wind turbines are in the region of 1500 €/kW (see EWEA (2009)). However, the markets for SWTs can be attractive in places where the prices of conventional electricity and fossil fuels are high, or in areas without access to electricity. The technology of the SWTs is clearly different from that used in large wind turbines, mainly regarding the control and electrical systems, but also the design of the rotor.

During the last years, there has been an exponential growth of horizontal axis wind turbine (HAWT) size, since large wind turbines are more cost-effective and remain more economical for kW installed. Partly because, for small wind turbines, towers need to be higher in proportion to diameter; to clear obstacles to wind flow, and escape the worst conditions of turbulence and wind shear near the surface. In addition, controls, electrical connection to grid and maintenance are much lower, in proportion, for large turbines. Land-based supply is now dominated by turbines in the 2MW range, and some new models reach even more than 7MW power capacity, like the E126, from Enercon (shown in Figure 1.3), with a diameter of $D = 127$m, and a power output of $P = 7500$kW.

The key factor in maintaining design development into the megawatt range has been the appearance of the offshore market. For offshore applications, optimum economics requires larger turbines to limit the proportionally higher costs of infrastructure (foundations, electricity collection, subsea transmission, maintenance, etc...). Figure 1.1 shows an example of an offshore wind farm, placed in Denmark.

Regarding the aerodynamics of wind turbines, the engineering community has still some goals to achieve, in order to design highly cost-efficient turbines that can compete with other energy sources in the near future. Firstly, with the increasing size and complexity of wind turbines, a full understanding of the aerodynamic phenomena is required, including external conditions, such as the wind speed distribution on the rotor plane, for different wind turbine configurations and sites. Besides, the structural integrity of the wind turbine should be improved, through a better estimation of the design loads. Finally, it would be desirable to optimize the balance between performance, loading and lifetime. This could be achieved with advanced control systems.

Figure 1.2: Small VAWT QR5 (*from www.quietrevolution.com*).

Figure 1.3: Large HAWT E126 (*from www.enercon.de*).

1.2 The Research Question

Understanding aerodynamic phenomena and estimating loads reliably is one of the main interests by the wind energy community, as has just been discussed. Pursuing these objectives, the research work presented herein aims at providing a method for measuring the loads impinged on a HAWT blade by means of stereoscopic particle image velocimetry (SPIV), which is a non-intrusive technique. Moreover, with this approach, pressure and velocity fields around the blade would be obtained simultaneously, giving a better insight of the HAWT aerodynamics. The study uses a Momentum Equation (ME) contour-based approach, and a pressure Poisson solver.

Conventionally, wind turbine blade loads have been measured with pressure taps and Pitot-tube wake rakes. However, these techniques provide only pointwise information. Besides, wake rakes introduce flow perturbations and pressure taps require the modification of the model. Another way of measuring forces is the use of multi-component balances, although, they provide only with global torque and thrust on the turbine, without providing with local information on the blade itself.

In the last years, there have been several projects that studied the feasibility of calculating aerodynamic loads using only velocity fields and their derivatives. In this way, different approaches have been undertaken all using a momentum-based control-volume formulation. The first considerations of this methodology used a vorticity based formulation.

On the one hand, Lin & Rockwell (1996), used a vorticity based method to measure

instantaneous lift on a cylinder. The method followed the concept previously described by Lighthill (1986). On the other hand, Noca *et al.* (1999) , extended this approach presenting a comparison of three different methods (one of which cleverly eliminates the need of explicitly evaluating the pressure term) for calculating time dependent lift and drag on a bluff body; in this case, it was a cylinder immersed in water and moved unidimensionally by a towing tank. They concluded that their formulations were effective for flow fields that were either highly resolved or well accentuated (with large force coefficients).

The advantage of these vorticity-based approaches is that the relationship between the evolution of the vorticity field and the loading is direct. Effective application requires, however, accurate evaluation of vorticity throughout the domain of interest. With the objective of developing alternative techniques that minimized evaluation of spatial derivatives, other research studies have been undertaken ever since. All of them follow a momentum-based approach and a control-volume methodology, but abandon the vorticity-based formulation. The main differences encountered are the PIV method chosen, the way of calculating the pressure term and the fluid mechanical conditions of the problem under study. A brief chronological review is presented herein.

Firstly, Unal *et al.* (1997) calculated lift in a cylinder submerged in quiescent water and subjected to sinusoidal oscillations. Conventional PIV data were used for the purpose.

Wu *et al.* (2005) used new formulation that allowed to measure the total force acting on a solid body that is moving, solely in terms of control-surface integrals, provided the flow is incompressible. Numerical 2D data were used in order to prove the formulation.

In the microPIV (μPIV) field, Fujisawa *et al.* (2005) evaluated pressure fields in a microchannel flow, in conjunction with the 3D pressure Poisson equation. Pressure errors were ascribed to the limited number of measurement planes by μPIV , the computational grids for solving the pressure Poisson equation and the random error in μPIV. In general, there was a good agreement between the experimental results and the numerical simulations.

Van Oudheusden *et al.* (2006) proved the feasibility of using PIV velocity data for aerodynamic force characterization of an airfoil. In this case, because of the low value of the drag, application of the contour procedure yielded unacceptably large relative errors. Thus, drag determination was improved by introducing a classical wake approach as in Jones (1936). The same research group (see Van Oudheusden *et al.* (2007 and 2008)) extended the method to steady compressible flows with shocks and measured forces in an airfoil, submerged in a supersonic flow. As in this flow regime the density appears as an extra unknown in the Momentum Equation, additional flow equations were invoked (gas law, adiabatic flow condition). In order to avoid computing the pressure field iteratively, a spatial-marching gradient-integration was employed.

Following the same directions, Ragni *et al.* (2009) conducted PIV experiments on an airfoil model in the transonic flow regime, inferring surface pressure distribution and aerodynamic loads. The surface pressure showed excellent agreement with the pressure orifices in the absence of shocks, while in the presence of shocks, the use of the isentropic relation introduced an error on the pressure values, which remained moderate for mild shock strengths. In order to obtain accurate results for the drag coefficient, the wake-based formulation was again used.

Kurtulus *et al.* (2006) performed Time Resolved Particle Image Velocimetry (TRPIV) measurements to obtain unsteady forces on a square section cylinder in a 2D airflow at

Re = 4890. The unsteady pressure gradient field was obtained invoking the Navier-Stokes equations an the pressure was evaluated based on the Bernoulli equation (in the inviscid region) and the line integration of the pressure gradient from the complete Navier-Stokes equations inside the turbulent wake.

Moreover, Jardin *et al.* (2009) used TRPIV as a basis to evaluate both unsteady forces and vortical structures generated by an airfoil undergoing complex motion (i.e. asymmetric flapping flight) through the Momentum Equation approach and a multidimensional wavelet-like vortex parametrization method, respectively. The use of both methods allowed an accurate temporal correlation and further insight into the lift generating mechanisms. The drag prediction was subjected to specific difficulties linked to the pressure contribution evaluation.

Using Time Resolved Tomographic PIV (TR-TOMO PIV), Violato *et al.* (2011) investigated the rod-airfoil flow air flow. By comparing Lagrangian and Eulaerian approaches, the latter was found not applicable to evaluate the pressure gradient field if a relative precision error lower than 10% was required.

Albrecht *et al.* (2011) presented a method to derive a planar, instantaneous body force distribution from a give two-dimensional velocity field without knowledge of the pressure field, under the restriction that the body force is dominated by one component only. PIV and DNS simulations of a wall jet induced by a known body force were conducted to validate the method, demonstrating a good agreement of the original and reconstructed force fields. It was concluded that a moderate spatial resolution from an average PIV setup was sufficient for correct force reconstruction. However, highly accurate velocity measurements were crucial due to the third order spatial derivatives involved.

Finally, Ragni *et al.* (2011) studied the flow field around the tip region of a rotating aircraft propeller blade, running at transonic speed, by means of Stereoscopic PIV. A moving frame of reference was used, allowing for steady formulation. The pressure field was inferred from the 3D velocity data using the pressure Poisson equation. On the one hand, the sectional PIV computed thrust was found the most in agreement with the one provided by the CFD simulation data. On the other hand, the experimental sectional torque force compared favorably to the numerical data mainly at the inboard part of the measurement domain, while a consistent deviation between experiment and simulation was observed at the immediate tip region.

This last study has many similarities with the final goals pursued in the research work presented herein, apart from the fact that flow can be considered incompressible around a HAWT. Moreover, the present project will aim at going one step further, calculating not only the loads with axial flow (steady case), but also with yawed flow (unsteady case). However, before attempting to measure forces on a rotating blade, the methodology will be validated using Direct Numerical Simulation (DNS) data, and a first experimental campaign will focus on measuring forces around an inclined flat plate.

Finally, the near wake of a HAWT model is studied by means of TRPIV, with the purpose of determining the vorticity fields shed and setting the basis to evaluate unsteady forces through the Momentum Equation. In this way, tip blade vorticity and vorticity shed by the airfoil at a midspan position of the blade will be studied.

A brief chronological review of the previous work done on the experimental study of the near wake of a wind turbine is presented below. Most of the projects were carried out using PIV. It can be observed that, for more than a decade, continuous efforts have been made

to correctly visualize the near vortex wake, with the aim of creating a reliable data base, that would serve as means of validation for numerical simulations under development.

Firstly, Grant *et al.* (2000) used PIV to measure the velocity field of the trailing vortices from the blades of a HAWT in yaw. The creation of the trailing vortex circulation was shown to vary as a function of the azimuth phase angle of the rotor, and the angle of yaw between the wind and the turbine.

Whale *et al.* (2000) carried out an investigation into the properties of the vortex wake behind a wind turbine rotor model, using PIV. The two-bladed model was operated at tip speed ratio TSR = 3-8 and chord Reynolds numbers Re = 6,400-16,000. It appeared that the fundamental behavior of the helical vortex wake was relatively insensitive to blade chord Re, so long as similarity of TSR was observed.

The physics of power extraction by wind turbines were studied by Vermeer *et al.* (2003), reviewing both the near and the far wake region. The emphasis was put on measurements in controlled conditions.

Moreover, Massouh *et al.* (2007) presented a wind tunnel study of flow downstream a small HAWT using PIV. Explorations were carried out in azimuth planes with different angles using the phase-locked technique.

The first results obtained by the MEXICO (Model Experiments in Controlled Conditions) project, financed by the European Commission, were presented by Snel *et al.* (2007). The main objective was to create a database of detailed aerodynamic and load measurements on a wind turbine model, in a large and high quality wind tunnel, to be used for model validation and improvement. A 4.5 m diameter HAWT model stood for both the extended BEM modeling (used in state of the art design and certification software), and CFD modeling of the rotor and near wake flow.

In the field of micro-wind energy, Hirahara *et al.* (2007) developed a very small wind turbine of 0.5m diameter. The flow around the wind turbine and the influence of the turbulence were investigated with PIV. The approaching flow velocity and the accelerated flow field passing the blade tip was obtained. Tip vortex shed from the blade tip was also visualized clearly.

Regarding vertical axis wind turbines (VAWT), Ferreira *et al.* (2008) analyzed the behavior of a VAWT by means of PIV, focusing on the development of dynamic stall at different tip speed ratios.

Haans *et al.* (2008) focused on the near wake of a model HAWT in both axial and yawed flow conditions. Three different downstream planes, parallel to the rotor plane, were captured by single sensor hot film traverses. The main goals was to obtain a detailed understanding of the near wake development and to arrive at a base for model construction and validation.

Again with the MEXICO data, Micallef *et al.* (2010) validated an inverse free wake lifting line model, a direct free wake model and a BEM model. In this project, pressure measurements were acquired by means of Kulite pressure sensors, and velocity fields were obtained using PIV, with the aim of tracking the tip vortex trajectory.

Finally, Xiao *et al.* (2011) conducted large view flow field measurements using PIV on a rotating 1/8 scale blade model of the NREL UAE phase VI wind turbine. The motivation was to establish the database of the initiation and development of the tip vortex to study

the flow structure and mechanism of the wind turbine. The results showed that the tip vortex first moved inward for a very short period and then moved outward with the wake expansion, while its vorticity decreased with time.

1.3 Structure of the Dissertation

After having discussed what is the purpose of the thesis, why is it relevant for the wind energy community and what is the state of the art in the fields that want to be approached, the main objectives of the research work will be addressed progressively.

Firstly, a brief overview of the aerodynamics of a HAWT will be exposed by means of the Blade Element and Momentum (BEM) theory, in Chapter 2. This method allows to better understand the physics of the problem, and will be used to design the two scaled-down turbines constructed for the experimental campaigns.

Afterwards, a thorough analysis of the Momentum Equation (ME) contour-based methodology, used to measure forces out of PIV velocities, will be made in Chapter 3. A brief description of the basic concepts of PIV will be introduced in the beginning of this chapter. In addition, the implemented code to measure loads from PIV velocities will be validated by means of DNS data, both for a circular cylinder (Re = 200) and an inclined flat plate (Re = 10,000), and the results will be discussed.

The first attempt to use the proposed methodology was undertaken using the same flat plate geometry, with the aim of measuring forces out of 2D-PIV data, and comparing them with those provided, simultaneously, by a high sensitive balance. The experiments were done in a small wind tunnel at the UPC's Aerospace Department, in Terrassa, with Re = 30,000-120,000 conditions. Chapter 4 will describe the experimental set up, the methodology and the results obtained.

Once the methodology has been analyzed and validated for a 2D stationary and steady case, it will be used to measure forces with 3D-SPIV data along the span of a rotating HAWT blade, operating both in axial flow (steady case) and in yawed flow (unsteady case). These tests took place in a big subsonic wind tunnel, at TU-Delft's Aerodynamics Department (The Netherlands), for tip chord Re = 275,000. Chapter 5 will describe the experimental set up, the methodology, the uncertainties of the procedure, the pressure and velocity fields obtained, and the calculated loads. These final results will be compared with those obtained through a panel method code. This chapter constitutes the main goal of the thesis, since all previous chapters make up the way to finally assess the possibility of estimating aerodynamic loads in a rotating HAWT blade out of SPIV.

Finally, the near vortex wake of a HAWT working in low Re conditions (Re = 16,000 at the tip), will be visualized in Chapter 6, with the aim of investigating the relation between the shed vorticity and the originated unsteady forces. This experimental campaign constituted the initial investigation done for this PHD thesis dissertation. It was undertaken in a medium size water tunnel at the Mechanical & Aerospace Department of Rutgers University (USA). Although it might seem further from the main purpose of the thesis, it was indeed an important step in the achievement of this research project, since it was decisive for focusing in what later became the main purpose of this investigation.

The main achievements and the conclusions extracted from the present research work will be exposed in Chapter 7, with the aim of providing with a small contribution to the wind

energy and fluid dynamics community. A brief discussion on future work will be presented in addition.

Chapter 2

HAWT Aerodynamics Overview

2.1 Introduction

A Horizontal Axis Wind Turbine (HAWT) extracts kinetic energy from the wind and, as a result, the mass of air going through the rotor decelerates (in fact, the presence of the turbine causes the approaching air gradually to slow down, and when the air arrives at the rotor disc its speed is already lower than the free stream wind speed). As the air goes through the rotor disc, there is a drop in static pressure; the air that proceeds downstream with reduced velocity and reduced static pressure forms the wake. Since the air slows down but does not become compressed, the cross-sectional area of the near wake expands to accommodate the slower motion. Far downstream, the air progressively recovers the atmospheric pressure at the expense of kinetic energy, which causes further deceleration of the wind.

Thus, between the far upstream region and the far downstream region of the HAWT, there is no change in static pressure but a reduction in kinetic energy. Part of this extracted energy is transformed in useful work by the turbine, but some of it is spilled back into the wind as turbulence and eventually dissipated as heat. Several ways of computationally modeling the physics of these phenomena have been developed so far:

Blade Element and Momentum Theory (BEM) is one of the most popular tools in HAWT engineering, due to its low computational costs and fast results. The method combines the conservation of Momentum across the rotor (which is considered as an actuator disk) and the integration of aerodynamic forces over all blade elements. To achieve closure, the thrust calculated from the Momentum Equation is equated with that calculated with the blade element equations; in this way, the induced velocities across the rotor can be assessed.

The kinematics that define the turbine motion together with the induced velocity across the rotor determine the inflow conditions for each blade element. Finally, once the Reynolds number and the angle of attack are assessed for a given blade section, the aerodynamic forces are calculated using lift and drag coefficients from existing experimental airfoil data.

Although BEM models are a practical approach to HAWT aerodynamics, they have some limitations due to simplifying assumptions. For instance, they are not able to model swirl flow, wake expansion, tip effects...etc. Thus, in order to improve their performance some corrections are usually adopted.

Vortex models use the vorticity transport equation and the Biot-Savart equation to model the shed wake and its influence on the blades. The wake is thus defined by a lattice composed of overlapping vortex rings.

Once more, the angle of attack can be determined in every section of the blade combining the motion of the blade with the wake induced flow; and then, lift and drag can be assessed with the aerodynamic coefficients obtained from experimental airfoil data (for a given section and Reynolds number). In this way, vortex methods are similar to BEM methods.

The closure of the model is achieved by the Kutta-Jukovsky theorem, which links circulation to lift. Finally, the strength of the shed vortex (and its influence on the blades) can be determined taking in account the conservation of the total circulation.

Panel methods can be considered as an extension to the vortex methods because they model the wake in the same way. However, they do not require external airfoil data, which is an important advantage. In order to model the geometry, they use the Prandtl-Glauert equation for inviscid flows. Panel methods are thus suitable for investigating new, not known sections.

Nevertheless, if unaltered, the governing equations for panel methods do not cover viscous phenomena. Therefore, while the vortex methods above include drag effects on the blade (because they use experimentally determined section data), a panel method is usually coupled with a boundary layer code in order to capture the effect of friction. Besides, viscosity also plays a role in the wake behavior, and in the vorticity diffusion and dissipation.

Computational fluid dynamics (CFD) models that solve the Navier-Stokes equations offer the opportunity to capture nearly all phenomena that play a major role in HAWT aerodynamics. However, their computational cost makes a full reliable solution impractical for use as a design code. Nevertheless, CFD models using (RANS) or Large Eddy Simulations (LES) or even Direct Numerical Simulations (DNS) are nowadays used to investigate HAWT aerodynamics in different ways.

The next sections of this chapter will focus on the fundamentals of BEM. This method was used to design the scaled down HAWT models presented in this research work. Furthermore, understanding the theory (and its limitations), represents a clarifying approach to the aerodynamics of horizontal axis wind turbines. A thorough explanation of the BEM method can be found in Burton *et al.* (2001) and Hansen (2008).

2.2 Blade Element and Momentum Theory

2.2.1 Momentum Theory

The Momentum Theory applied to a 1-D model assumes the following hypothesis:

- Stationary, frictionless and incompressible flow.
- No external force acts on the fluid up or downstream of the rotor.
- The air that passes through the disc is confined in a stream tube of circular cross section.
- There is no wake rotation.

- The rotor is a permeable disc.

The actuator disc extracts kinetic energy from the air and, as a result, it slows down. At the disc, the net streamwise velocity is

$$V_d = V_\infty(1-a) \tag{2.1}$$

where a is called the *axial flow induction factor.*

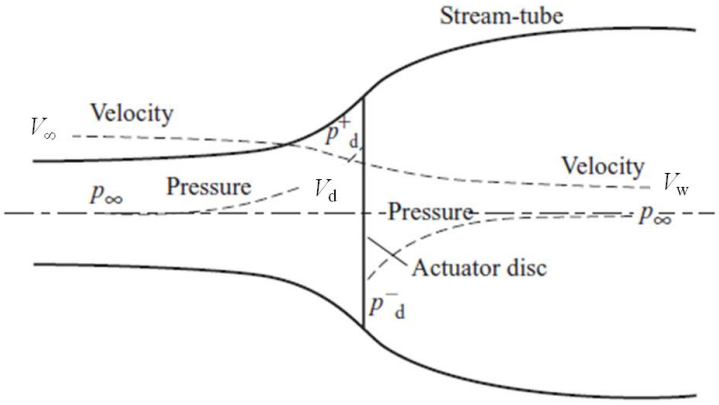

Figure 2.1: Stream tube around the actuator disc: axial velocity and pressure. *Adapted from Burton et al. (2001).*

Since the mass flow rate is kept constant, and the velocity is decreased, there is a change in Momentum equal to the overall change of velocity times the mass flow rate. The force causing this change of Momentum comes entirely from the pressure difference across the actuator disc, since the pressure distribution along the curved streamlines enclosing the wake does not exert any axial force.

$$T = (p_d^+ - p_d^-)A_d = (V_\infty - V_w)\rho A_d V_\infty(1-a) \tag{2.2}$$

The resulting velocity downstream of the rotor disc is obtained applying Bernoulli equation in the streamtube, and thus, it is concluded that half of the axial speed loss in the stream tube takes place upstream of the actuator disc, and the other half downstream. Therefore:

$$V_w = V_\infty(1-2a) \tag{2.3}$$

Hence, the force impinged on the air results in:

$$T = (p_d^+ - p_d^-)A_d = 2\rho A_d V_\infty^2 a(1-a) \tag{2.4}$$

And since this force is concentrated in the actuator disc, the power extracted from the air is given by:

$$P = TV_d = 2\rho A_d V_\infty^3 a(1-a) \tag{2.5}$$

The power is often non-dimensionalized with respect to the available power in a cross-section equal to the swept area A_d, as a power coefficient:

$$C_P = \frac{P}{\frac{1}{2}\rho V_\infty^3 A_d} \tag{2.6}$$

Similarly, a thrust coefficient is defined as:

$$C_T = \frac{T}{\frac{1}{2}\rho V_\infty^2 A_d} \tag{2.7}$$

Using Equation 2.4 and Equation 2.5, the power and thrust coefficients can be expressed as:

$$C_P = 4a(1-a)^2 \tag{2.8}$$

and

$$C_T = 4a(1-a) \tag{2.9}$$

Experiments have shown that the assumptions made by the Momentum theory are no longer valid for values of $a \geq \frac{1}{2}$. In these conditions, empirical modifications have to be made.

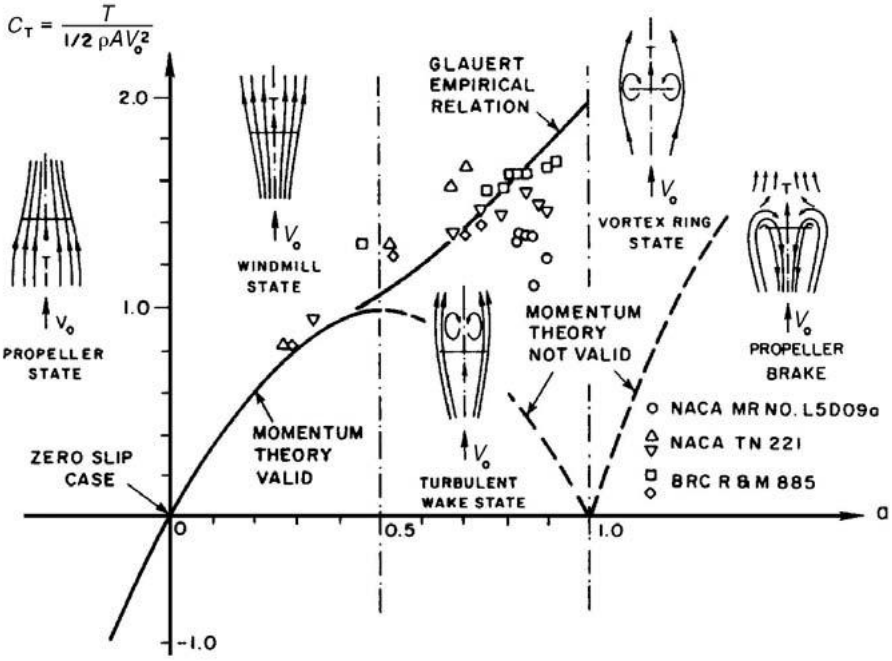

Figure 2.2: Theoretical and measured values of the thrust coefficient as a function of the axial induction factor and the corresponding rotor states. *Adapted from Hansen (2008).*

For a wind turbine, a high thrust coefficient C_T and thus a high axial induction factor a is present at low wind speeds. In these conditions the free shear layer at the edge of the wake becomes unstable, since the velocity jump $V_d = V_\infty(1-a)$ becomes too high and eddies are formed which transport Momentum from the outer flow into the wake. This situation is called *the turbulent wake state.*

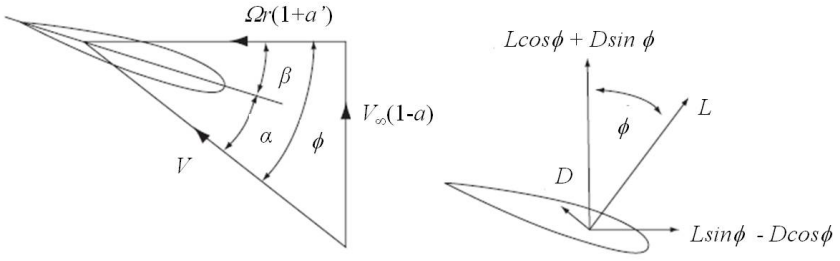

Figure 2.3: Blade element velocities and forces. *Adapted from Burton et al. (2001).*

2.2.1.1 Effects of Rotation

In the one dimensional Momentum theory for an ideal rotor, there is no rotation of the wake. The inclusion of the wake rotation in the Momentum theory provides with a more accurate method. In this new approach, the stream tube is discretized into N annular elements of height $\mathrm{d}r$, between which there is no radial dependency.

The exertion of a torque on the rotor disc by the air passing through it requires an equal and opposite torque to be imposed upon the air. This reaction torque causes the air to rotate in opposite direction to that of the rotor. Therefore, in the wake of the rotor disc, the air particles have a velocity component in a direction which is tangential to the rotation, as well as an axial component.

The tangential velocity at the rotor disc is expressed as $\Omega r(1+a')$, where r is the distance of the annular element to the rotation axis and $a'$is called the tangential induction factor.

The thrust from the disc on this annular control volume can thus be found as:

$$\mathrm{d}T = 4\Pi r\rho V_\infty^2 a(1-a)\mathrm{d}r \tag{2.10}$$

And the torque $\mathrm{d}M$ on the annular element is found using the integral moment of the Momentum Equation on the control volume ($\overrightarrow{M} = \iint_s \overrightarrow{r} \times \rho\overrightarrow{V}(\overrightarrow{V}\cdot\overrightarrow{\mathrm{d}s})$) and setting the rotation velocity to zero upstream of the rotor:

$$\mathrm{d}M = 4\Pi r^3\rho V_\infty \Omega(1-a)a'\mathrm{d}r \tag{2.11}$$

2.2.2 Blade Element Theory

The forces on a blade element can be calculated by means of two dimensional airfoil characteristics using an angle of attack determined from the incident resultant velocity in the cross-sectional plane of the element.

The following assumptions are made:

- There is no velocity component in the spanwise direction of the blade.
- Three dimensional effects on the blade are not taken into account.

The resulting velocity field around the blade element can be seen in the following figure:

The angle of attack is expressed as:

$$\alpha = \phi - \beta \tag{2.12}$$

where ϕ is the angle formed by the resultant local velocity and the rotor plane and β is the angle formed by the chord of the blade and the rotor plane (result of both the pitch and the local twist):

$$tan\phi = \frac{V_\infty(1-a)}{\Omega r(1+a')} \tag{2.13}$$

The modulus of the resultant velocity V is:

$$V = \sqrt{(V_\infty(1-a))^2 + (\Omega r(1+a'))^2} \tag{2.14}$$

Furthermore, if the lift and drag coefficients are known, the lift l and drag d per unit length are:

$$l = \frac{1}{2}\rho V^2 c C_l \tag{2.15}$$

$$d = \frac{1}{2}\rho V^2 c C_d \tag{2.16}$$

Since the interest relies on the normal and tangential forces to the rotor plane, the lift and drag are projected on these directions:

$$F_n = lcos\phi + dsin\phi \tag{2.17}$$

$$F_t = lsin\phi - dcos\phi \tag{2.18}$$

Normalizing the preceding equations results in:

$$C_n = C_l cos\phi + C_d sin\phi \tag{2.19}$$

$$C_t = C_l sin\phi - C_d cos\phi \tag{2.20}$$

A solidity factor is defined as the fraction of the annular area in the control volume which is covered by blades:

$$\sigma_r = \frac{cB}{2\Pi r} \tag{2.21}$$

where B is the number of blades and c is the chord at the radial position r.

The normal force and torque on the control volume of thickness dr are:

$$\mathrm{d}T = Bp_n \mathrm{d}r \tag{2.22}$$

$$\mathrm{d}M = Bp_t r \mathrm{d}r \tag{2.23}$$

Which can also be expressed as:

$$\mathrm{d}T = \frac{1}{2}\rho \frac{V_\infty^2(1-a)^2}{sin^2\phi} BcC_n \mathrm{d}r \tag{2.24}$$

$$\mathrm{d}M = \frac{1}{2}\rho \frac{V_\infty(1-a)\Omega r(1+a')}{sin\phi cos\phi} BcC_t r \mathrm{d}r \tag{2.25}$$

2.2.3 Combination of Blade Element and Momentum Theory

The Blade Element and Momentum Theory (BEM) combines the Momentum Theory and the Blade Element Theory, and same assumptions are considered. If Equation 2.10 and Equation 2.11, describing $\mathrm{d}T$ and $\mathrm{d}M$, obtained via the Momentum Theory, are equated with those obtained via the Blade Element Theory (i.e Equation 2.24 and Equation 2.25), two expressions for the axial induction factor a, and the tangential induction factor a', are obtained:

$$a = \frac{1}{\frac{4sin^2\phi}{\sigma_r C_n} + 1} \tag{2.26}$$

$$a' = \frac{1}{\frac{4sin\phi cos\phi}{\sigma_r C_t} - 1} \tag{2.27}$$

This way, the method achieves its closure: the induced velocities across the rotor can be assessed, and the inflow conditions for each blade element can be determined. Once the Re and the angle of attack are computed for each blade section, the aerodynamic forces can be calculated using aerodynamic force coefficients (available from experimental data).

It must be noted that the whole methodology relies on an iterative calculation, computed as follows:

1. Initialize a and a' (usually equated to zero).
2. Assess the flow angle ϕ with Equation 2.13 and the local angle of attack α with Equation 2.12.
3. Compute normal and tangential force coefficients C_n and C_t with Equation 2.19 and Equation 2.20, reading aerodynamic coefficients available from database.
4. Estimate normal and tangential induction factors a and a', using Equation 2.26 and Equation 2.27, and check if the values have changed more than a certain tolerance. If this is the case, the whole iteration is started from step 2. Otherwise, the calculation finishes with next step, since inflow conditions have been successfully determined.
5. Calculate the local loads on the segments of the blade considered.

2.2.3.1 Prandtl's Tip and Root Correction Factor

If the axial flow induction factor a is large at the blade position, then the inflow angle ϕ will be small and the component of the lift force in the tangential direction will be small as well, resulting in a smaller contribution to the torque. A reduced torque means reduced power and this reaction is know as tip/root loss, because the effect occurs at the innermost and outermost parts of the blades, where the vortex shedding is most important.

Prandtl (reported by Betz (1919)) developed an ingenious approximate solution which yields a relatively simple analytical formula for the tip/root loss function. The theory applies only to the fully developed wake. Prandtl replaced the helicoidal vortex sheets with a succession of discs moving with the uniform central wake velocity. This way, Prandtl derived a correction factor f that, applied to Equation 2.10 and Equation 2.11, results into:

$$\mathrm{d}T = 4\Pi r \rho V_\infty^2 a(1-a) f \mathrm{d}r \tag{2.28}$$

$$\mathrm{d}M = 4\Pi r^3 \rho V_\infty \Omega (1-a) a' f \mathrm{d}r \tag{2.29}$$

where the correction factor f is computed as:

$$f_t = \frac{2}{\Pi} arccos(e^{-\frac{B}{2}\frac{R-r}{rsin\phi}}) \tag{2.30}$$

$$f_r = \frac{2}{\Pi} arccos(e^{-\frac{B}{2}\frac{r-R_h}{rsin\phi}}) \tag{2.31}$$

$$f = f_t f_r \tag{2.32}$$

where R is the total radius of the rotor, $R_h$is the hub radius (radius of the blade root) and r is the local radius. The derived equations for a and $a'$are:

$$a = \frac{1}{\frac{4fsin^2\phi}{\sigma_r C_n} + 1} \tag{2.33}$$

$$a' = \frac{1}{\frac{4fsin\phi cos\phi}{\sigma_r C_t} - 1} \tag{2.34}$$

2.3 Conclusions

The basic concepts that define the Blade Element and Momentum (BEM) theory have been exposed in this chapter. The theory assumes that the flow, at a given annulus, does not affect the flow at adjacent annuli, which allows the rotor blade to be analyzed in sections. The resulting forces can be summed over to get the overall forces of the rotor. Axial an angular Momentum balances are used to determine the flow around the blade. Further information can be found in Burton *et al.* (2001) and Hansen (2008).

BEM is widely used both in the industry and in the research community, due to its simplicity and overall accuracy. However, its simplifying assumptions limit its use when non axisymmetric effects influence the flow. Computational fluid dynamics (CFD) solvers, based on Reynolds Averaged Navier Stokes (RANS) or Large Eddy Simulations (LES), are also used to study different HAWT aerodynamic problems, although their computational cost is much higher. Panel methods and Free Vortex models represent alternative options to simulate and predict the aerodynamics of a wind turbine.

The presented BEM method was used in the design of the two scaled down wind turbine models constructed for this research project. More details of these two models can be found in chapters 5 and 6, respectively. In addition, the explanation of the theory and its limitations represent a good way of studying the aerodynamics of a HAWT, and has served as means of checking the consistency of the results in the experimental campaigns.

Chapter 3

Aerodynamic Loads from PIV

3.1 Introduction

Particle Image Velocimetry (PIV) is a non intrusive laser technique that allows for obtaining instantaneous velocity fields of a flow in a determined region. The fluid is seeded with tracer particles that are assumed to faithfully follow the flow, while a laser illuminates the region and makes these particles visible (differentiating them from the background). Finally, the motion of the seeding particles is used to calculate speed and direction of the studied flow.

Other techniques used to measure flows are Laser Doppler Velocimetry (LDV) and Hot Wire Anemometry (HWA). However, the main difference between PIV and those techniques is that PIV captures the instantaneous 2D-2C (two dimensions, two velocity components) flow field, whereas LDV and HWA only give information of the velocity in a single point. Furthermore, some variants of PIV, which use a multiple camera arrangement, can analyze 2D-3C (Stereoscopic PIV) or even 3D-3C (Tomographic PIV) velocity fields. With cameras capable of taking picture frames in continuous mode with a high repetition rate, unsteady velocity fields can also be characterized in time (Time Resolved PIV).

Since PIV is a non intrusive technique, it would be very convenient to enlarge its capacities, and make it possible to measure forces, out of the velocity fields obtained with it. Different research studies have been undertaken with this goal so far, and their different approaches are summarized in Section 1.2.

In this chapter, a thorough description of the methodology used in this study, to measure forces out of PIV, will be exposed. This methodology was validated using Direct Numerical Simulation data, for two different cases; a circular cylinder and an inclined flat plate immersed in a flow, at Re =200 and Re =10,000, respectively. The results of this validation will be analyzed and discussed.

Furthermore, a brief explanation of the basic concepts of PIV will be explained in the next Section; defining the tracer particles, the light source, the imaging procedure, and its subsequent processing.

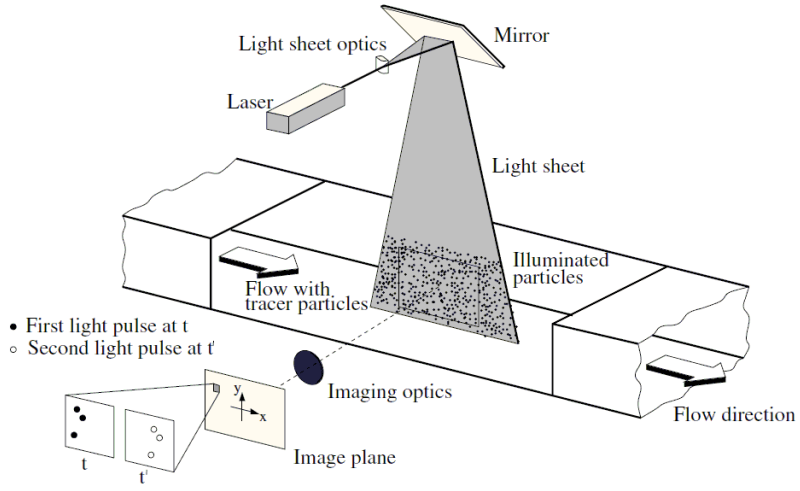

Figure 3.1: Typical experimental PIV arrangement. *Adapted from Raffel et al. (1998)*

3.2 Particle Image Velocimetry

Typical PIV apparatus consists of a camera , a laser with an optical arrangement to limit the physical region illuminated, a synchronizer to act as an external trigger for control of the camera and the laser, the seeding particles and the fluid under investigation. A typical PIV arrangement in a wind tunnel is depicted in Figure 3.1. In addition, some PIV software is needed to post-process the optical images and obtain the velocity fields. The PIV technique has been developed over the last twenty five years and there are still important challenges to achieve that would improve the accuracy and scope of this powerful technique. A thorough historical review of the method can be found in Adrian (2005).

PIV is very broad and there are many different ways of implementing it. In the next subsections the main working principles of the technique will be described, focusing on the methodology chosen for the current research project. Further information on the method and its multiple applications is available in Westerweel *et al.* (1993) and Raffel *et al.* (1998). .

3.2.1 Tracer Particles

Proper tracer particles must be small enough to follow the fluid motion and should not alter fluid or flow properties. The tracing ability and the dispersion characteristics depends on the size and shape of the particles and the densities of particles and fluid flow. The particle density should be as close as possible to the one of the flow, in order to minimize the effect of buoyancy forces over them.

If we assume spherical particles in a viscous fluid at very low Reynolds numbers (see Raffel *et al.* [40]) , the velocity lag of the particle within a flow with uniform acceleration $\vec{a}$ is given by Equation 3.1:

$$\vec{V}_{lag} = \vec{V}_p - \vec{V} = D_p^2 \frac{\rho - \rho_p}{18\mu} \vec{a} \tag{3.1}$$

where $\vec{V}_p$ is the particle velocity, D_p is the particle diameter,ρ_p is the particle density, μ is the dynamic viscosity of the fluid, ρ is the density of the fluid and $\vec{V}$ the velocity of the flow.

Therefore, the tendency of particles to attain velocity equilibrium with the fluid linearly decreases with the difference of densities and with the square of the particle diameter. If the fluid acceleration is not constant or Stokes drag does not apply, the equations of the particle motion become more difficult to solve. Nevertheless, this results give a good qualitative idea of the influence of particle size and densities in the ability of particles to track the fluid velocity.

At the same time, particles must be large enough to be visible by the camera. As laser sheet leads to a low energy density, particle scattering efficiency is important. It is often more effective and economical to increase the image intensity by properly choosing the scattering particles than by increasing the laser power.

The scattering cross section increases with the ratio of the refractive index of the particles to that of the surrounding medium and with the ratio of the particle size to the laser wavelength. It also depends on the particle shape and orientation, and also on polarization and observation angle.

For spherical particles with diameters larger than the wavelength of the incident light λ, Mie's scattering theory can be applied. A detailed description is given in Van de Hulst (1981). The Mie scattering can be characterized by the normalized diameter, q, defined by Equation 3.2, where D_p is the particle diameter:

$$q = \frac{\pi D_p}{\lambda} \tag{3.2}$$

The light scattering quickly increases with particle size (the average intensity roughly increases with q^2), and that forward scatter (in the 180° direction) is maximum.

In conclusion, for a given refractive index and laser wavelength, larger particles are able to scatter more light. Therefore an optimum particle size should represent a compromise between the tracing and the scattering characteristics of the particles.

In addition, a uniform particle size is desirable in order to avoid excessive intensity from larger particles and background noise from the smaller ones. Particles that naturally exist in the flow seldom meet the above requirements. Hence, in PIV applications, it is often necessary to seed the flow with a chosen tracer particle. Moreover, getting an optimum particle concentration uniformly distributed along the flow domain is critical to the success of obtaining the velocity field. It is very important to make sure that all regions of the fluid domain get seeded with enough number of particles.

3.2.2 Light Source

Lasers are widely used in PIV, because of their ability to emit monochromatic light with high energy density, illuminating and recording the tracer particles without chromatic aberrations. Furthermore, laser light can be easily guided through mirrors or optical fiber through the test region, and then be converted, through a system of lenses, into thin light sheets.

Neodymium-YAG lasers (Nd:YAG lasers for $\lambda = 1064$nm and $\lambda = 532$nm) are the most common solid-state systems for conventional PIV applications where high pulse energies at moderate repetition rates are required. In these lasers, the beam is generated by Nd^{3+} ions within YAG (yttrium-aluminum-garnet, $Y_3Al_5O_{12}$) crystal bars. At standard operating

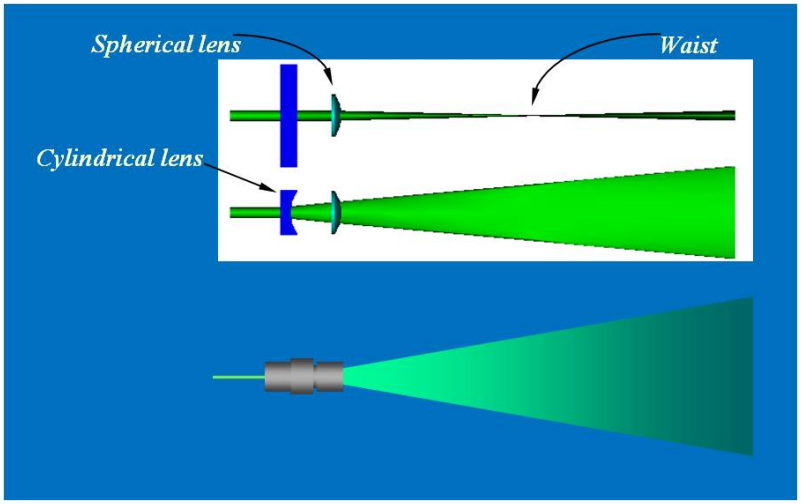

Figure 3.2: Typical PIV light sheet optics configuration.

temperatures, this laser only emits the strongest wavelength, 1064 nm (infrared). For safety reasons, the laser beam is filtered to isolate the 532 nm harmonics (this is green light, the only harmonic which can be seen by the naked eye). They are optically pumped using a flash-tube or laser diodes. Nd:YAG lasers have a high amplification and good mechanical and thermal properties.

A typical Nd:YAG laser for PIV concentrates from 20 to 400 mJ energy per pulse in 4 to 15 ns duration pulses. Typical repetition rate is around 10 Hz per double pulse, and it is the separation between the two pulses within a pair what is critical to get accurate velocity fields. To get this double pulse, two independent beams are generated in different oscillators, and are guided through an arrangement of mirrors through a single output beam aperture.

The essential element for generating a thin light sheet of high intensity from a circular beam is a cylindrical lens, which expands the laser beam into a plane. Nevertheless, additional elements are usually necessary in order to obtain a high quality light sheet. At least one additional spherical lens has to be used for focusing the light into an appropriate thickness. Figure 3.2 shows a typical light sheet optics configuration. The minimum thickness (waist) is on the order of the wavelength of the laser light and occurs at the focal point of the spherical lens. This is the ideal location to place the analysis area of the experiment.

3.2.3 Image Recording

To perform PIV analysis on the flow, two exposures of laser light are required upon the camera from the flow. Originally, with the inability of cameras to capture multiple frames at high speeds, both exposures were captured on the same frame and this single frame was used to determine the flow, through auto-correlation. Faster digital cameras using CCD (charge coupled device) or CMOS (complementary metal-oxide-semiconductor) sensors have been developed since then, bringing along double-triggered and high speed cameras, so that each exposure can be isolated on its own frame for a more accurate cross-correlation analysis. An in-depth comparison of each type of sensor can be found in Hain *et al.* (2007).

For conventional PIV processed with cross-correlation, a fast double shuttered CCD camera

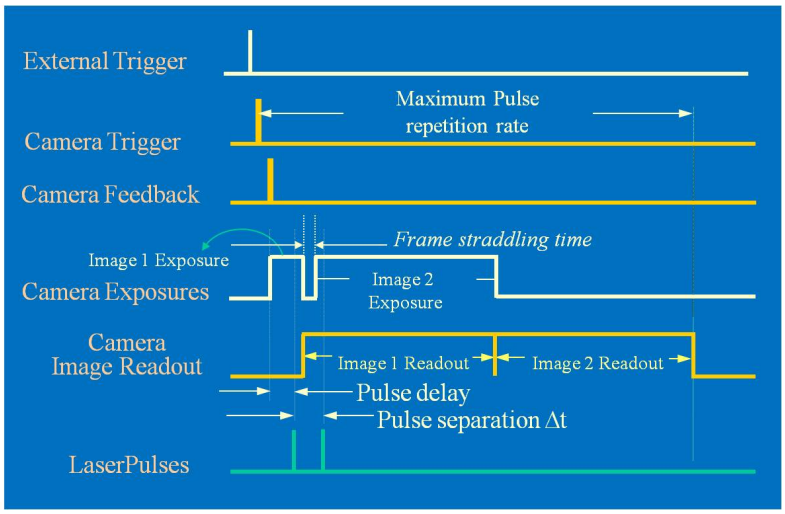

Figure 3.3: Example of a PIV set up synchronization.

is typically used to record images with "double frame". The minimum pulse delay is limited by the time necessary for the frame transfer of the camera. The time between the two laser pulses will determine the time separation between the two frames, as can be seen in Figure 3.3. The second image exposure is always longer than the first one and therefore, it has a bigger background intensity: this can be mitigated using a suitable filter in front of the camera lens.

A double-exposure camera is capable of recording two frames within a very short inter-frame period. After recording, both frames are transferred to the host system and the camera is prepared for the next image pair. Inter-frame times of below 500 ns are possible, but inter-pair times can be quite substantial, in the order of 0.1–0.5 s, depending on the image transfer system. Consequently, double-exposure cameras are well suited for repeatable flow events, or when only an instantaneous flow field is desired. This cameras use interline transfer CCD sensors, in which the information recorded on each pixel in the first frame of the pair is almost immediately transferred into adjoining storage sites, being later transferred both frames to the camera's internal memory.

For TRPIV, a high speed video system should be used, which can usually record up to 5000 frames per second (fps) at full sensor resolution and much higher rates at reduced image sizes. This is generally achieved through CMOS sensors.

3.2.4 PIV Processing

Statistical evaluation of the images is based in dividing the image in small areas called interrogation areas and cross-correlating each of them with its correspondent in the next image, as explained in Figure 3.4. This results in the most probable displacement vector for that particular particle pattern. Displacement can be estimated with sub-pixel accuracy. The process is repeated for all interrogation areas of the image pair resulting in a complete vector diagram of the flow studied. Finally, erroneous vectors should be identified and appropriately corrected.

Firstly, images are divided into square regions of size NxN pixels, the so called interrogation areas (IA). They should be selected containing a relatively small number of particles.

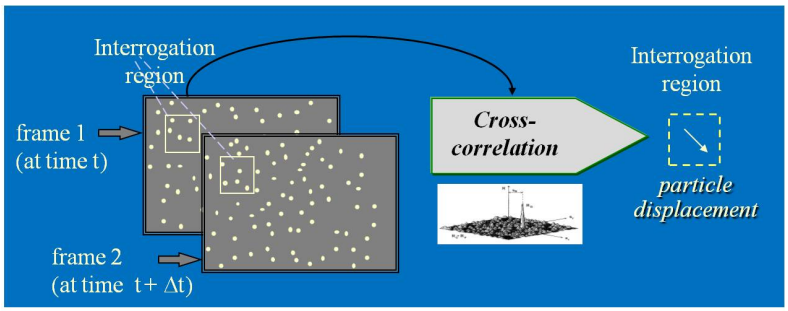

Figure 3.4: Scheme of the cross-correlation method.

In principle, an area containing only one single particle would be ideal, but it is hard to find that single same particle back in the second image, especially in a densely seeded flow as for PIV recordings. The probability for a good analysis result is highest when the interrogation area contains about 8-10 particle images (see Keane *et al.* (1992)).

The mean value of velocity in an IA at time t is calculated by cross-correlating the image intensities of that IA at time t and $t + \Delta t$. The cross-correlation function results:

$$CC\left(i,j\right) = \sum_{k=-M}^{M} \sum_{l=-M}^{M} I_g\left(k,\, l\right) I_g^{'}\left(i+k,\, j+l\right) \tag{3.3}$$

The functions I_g and $I^{'}{}_g$ represent the grey intensity values as extracted from the first and second image respectively, where I_g has the IA size, NxN and $I^{'}{}_g$ has a bigger size $(2M+N)\,\mathrm{x}\,(2M+N)$. Essentially the function I_g is linearly 'shifted' around in the sample $I^{'}{}_g$. For each choice of sample shift $(x,\, y)$, the sum of the products of all overlapping pixel intensities produces one cross-correlation value $CC\left(i,j\right)$. By applying this operation for a range of shifts, a correlation plane of size $(2M+1)\,\mathrm{x}\,(2M+1)$ is formed, together with the Probability Density Function (PDF). For shift values at which the sample particle images align with each other, the sum of the products of pixel intensities will be larger than elsewhere, resulting in a high cross-correlation value at this position. The highest value in the correlation plane can then be used as a direct estimate of the particle image displacement.

The alternative to calculating the cross-correlation directly using Equation 3.3 is to take advantage of the correlation theorem which states that the cross-correlation of two functions is equivalent to a complex conjugate multiplication of their Fourier transforms. Using the fast Fourier transform (FFT) reduces the number of operations required from $O\left[N^2\right]$ to $O\left[N \log_2 N\right]$. Then the product is transformed back to the real domain using an inverse FFT.

All $R\left(i,j\right)$ values apart from the one representing the displacement vector form the noise of the correlation function. This occurs because the displaced pattern in the second image is not identical to the pattern of the first one. The main reasons for this are:

- Background noise: which can be attenuated by filtering the images before performing the cross-correlation analysis.
- Out of plane displacements: a particle can escape from the laser sheet between the first and the second frame due to three-dimensional effects. Therefore, we must have

enough thickness of the laser sheet and assure that the flow is highly two-dimensional in the analyzed plane.

- In-plane displacements: If the interrogation window is not large enough, particles may shift to another IA between two consecutive frames. The highest measurable velocity is constrained by particles traveling further than the size of the interrogation area within the time Δt. As a rule of thumb, (this is generally achieved with CMOS sensors)the maximum displacement should be no larger than 1/4 of the IA side, so that no more that 25% of the particles are lost through in-plane displacements.

- It should be noted that the cross-correlation method inherently recovers linear shifts only. No rotations or deformations can be recovered by this first order method. IA should therefore be small enough to avoid big velocity gradients within them. As a rule of thumb, the maximum difference between the displacements of any pair of particles in an IA should be no larger that 5% of the IA side. For this reason, it is common to find spurious vectors in the vortex cores.

The high intensity peak in the result image has to be located to know the particle displacement. Because the peak is usually larger than one pixel, all pixel information of the peak can be used to calculate the peak position, and obtain sub-pixel accuracy. The process of selection of an interrogation area, cross-correlation, peak-finding, and calculation of the velocity vector, is repeated over the whole image, resulting in a complete vector representation of the flow field. To obtain more velocity information out of the images, adjacent interrogation areas are often overlapping.

The Probability Density Function (PDF) curve can be used to check whether the velocity field computation has a bias toward integer velocity values, which is called 'peak locking' effect. Peak locking can occur when the used seeding particles are too small and produce particle images on the CCD of less than one pixel in diameter.

When excessive noise is present, the maximum correlation value can occur at a position different from that representing the true displacement, yielding an spurious velocity vector. These vectors usually stand out clearly with respect to the surrounding vectors due to their very different orientation and magnitude. This enables relatively easy recognition to the observer as well as to any automated validation routine. Automated validation routines usually compare every vector with the surrounding ones and use statistical parameters (as the standard deviation or a histogram distribution function) to discriminate between correct and erroneous vectors. Once the spurious vectors are recognized, they should be replaced by new vectors, which should represent the local flow velocity as close as possible.

3.3 Load Calculation Methodology

3.3.1 Momentum Equation Approach

Aerodynamic forces exerted on a airfoil immersed in a flow are due to the surface pressure distribution and the viscous shear stresses. However, measuring these two terms with a non-intrusive experimental technique directly on the surface of the body is not possible. Thus, in order to calculate the aerodynamic loads, it is preferable to measure the change in Momentum of the flow inside a finite control volume (surrounding the airfoil) that has

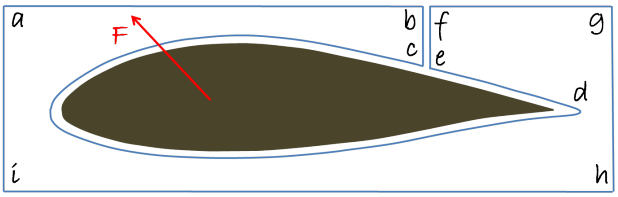

Figure 3.5: Scheme of the contour-approach used for load calculation.

no other external forces apart from those caused by the body itself (see Kurtulus *et al.* (2007)).

The finite control volume chosen may have any external shape, but in this case a rectangular shape ($aghi$), shown in Figure 3.5, is chosen for simplicity. It has two cuts ($bc - ef$) that connect with the internal shape of the control volume, which is wrapping the airfoil (edc). The force impinged by the airfoil on the flow causes a change in Momentum inside the control volume, and can therefore be assessed, as it is shown in Equation 3.4 and Equation 3.5.

Considering that the cuts are taken adjacent to each other, any shear stress or pressure distribution on one is equal and opposite to that on the other, i.e, the surface forces on them cancel each other (see Anderson (2001)). In addition, the convective acceleration is zero on the cuts because they are adjacent to each other and terms cancel themselves.

$$\iint_{s_{aghi}} \rho(\vec{V}\cdot\vec{n})\vec{V}\,\mathrm{d}s + \frac{\mathrm{d}}{\mathrm{d}t}\iiint_{v}\rho\vec{V}\,\mathrm{d}v = -\iint_{s_{aghi}} p\vec{n}\,\mathrm{d}s + \iint_{s_{aghi}} \overline{\overline{\tau'}}\vec{n}\,\mathrm{d}s + \iiint_{v}\vec{f_m}\mathrm{d}v + \vec{F}_{airfoil\Rightarrow flow} \tag{3.4}$$

$$\vec{F}_{flow\Longrightarrow airfoil} = -\iint_{s_{aghi}} p\vec{n}\,\mathrm{d}s + \iint_{s_{aghi}} \overline{\overline{\tau'}}\vec{n}\,\mathrm{d}s - \iint_{s_{aghi}} \rho(\vec{V}\cdot\vec{n})\vec{V}\,\mathrm{d}s - \frac{\mathrm{d}}{\mathrm{d}t}\iiint_{v}\rho\vec{V}\,\mathrm{d}v \tag{3.5}$$

The integral Momentum Equation expressed in Equation 3.5 (see White *et al.* (2004)) requires the velocity and the pressure fields in order to calculate the aerodynamic forces on the airfoil. Hence, it is necessary to reconstruct the pressure inside the control volume.The pressure gradient may be derived from the Momentum Equation in its differential form using the velocity field and its derivatives, as it shown in Equation 3.6 and Equation 3.7.

$$\rho\frac{\mathrm{D}\vec{V}}{\mathrm{D}t} = -\nabla p + \rho\vec{f_m} + \mathrm{div}\overline{\overline{\tau'}} \tag{3.6}$$

$$\nabla p = -\frac{\mathrm{d}}{\mathrm{d}t}\left(\rho\vec{V}\right) - \rho\vec{V}\cdot\nabla\vec{V} + \mu\triangle\vec{V} \tag{3.7}$$

Once the pressure gradient has been assessed in the control volume, there are different approaches to calculate the pressure in every point of the field. Historically, several authors have addressed this topic by implementing a space-marching algorithm that starts on the

boundary conditions, and marches towards the interior of the field, calculating pressures from the spatial derivatives. The main disadvantage of this method is that the error accumulates and propagates with the marching procedure (see De Kat (2008)). Different solutions have been implemented with the aim of minimizing this effect, some examples can be found in Kurtulus et al. (2007) and Liu *et al.* (2006).

In the present study, the pressure is obtained solving the Poisson pressure equation (see Equation 3.8) in all the flow field, using a forcing function $g(u, v)$ which is derived from the velocity field itself using the Momentum Equation, as shown in the Equation 3.9. The discretization of the Laplace operator is done using finite differences, which provides a matrix $\mathbf{D}$ containing information about the flow discratization.

$$\nabla^2 p \approx \mathbf{D}p = g(u,v) \Rightarrow p = \mathbf{D}^{-1} g(u,v) \tag{3.8}$$

$$\left\{ \begin{array}{ll} \left[\frac{p_{i+1,j}-2p_{i,j}+p_{i-1,j}}{\triangle x^2} + \frac{p_{i,j+1}-2p_{i,j}+p_{i,j-1}}{\triangle y^2}\right] & i = 1...n \\ & j = 1...m \\ \frac{\left[\frac{\partial p}{\partial x}\right]_{i+1,j} - \left[\frac{\partial p}{\partial x}\right]_{i-1,j}}{2\triangle x} + \frac{\left[\frac{\partial p}{\partial y}\right]_{i,j+1} - \left[\frac{\partial p}{\partial y}\right]_{i,j-1}}{2\triangle y} & = g(u,v)_{i,j} \end{array} = \mathbf{D}p \right\} \tag{3.9}$$

Finally, a Neumann condition was used on the airfoil surface, imposing $\frac{\partial p}{\partial n}$ (calculated with the Momentum Equation, as expressed in Equation 5.12), where $\overrightarrow{n}$ is the direction perpendicular to the airfoil surface. On the outer control, in the regions where the flow can be considered irrotational, a Dirichlet condition was used, calculating pressure with the Bernoulli theorem (see Equations 5.7 and 5.8). In the wake region a Neumann condition was imposed again, using the pressure gradient ($\frac{\partial p}{\partial x}$) resulting from the Momentum Equation.

$$p = p_t - \frac{1}{2}\rho(u^2 + v^2 + w^2) \tag{3.10}$$

3.3.2 Numerical Validation using DNS Data

In order to test the suitability of Momentum Equation (ME) approach to calculate aerodynamic forces, direct numerical simulation (DNS) data was used as a reference. DNS is a simulation in computational fluid dynamics in which the Navier-Stokes equations are numerically solved without any turbulence model. This means that the whole range of spatial and temporal scales of the turbulence must be resolved in the computational mesh, from the smallest dissipative scales (Kolmogorov microscales), up to the integral scale associated with the motions containing most of the kinetic energy. The number of operations required to complete the simulation is proportional to the number of mesh points and the number of time steps, and in conclusion, the number of operations grows as Re^3. Therefore, the computational cost of DNS is very high, even at low Reynolds numbers. DNS data was provided by the code developed by Albrecht *et al.* (2009), who used the SEMTEX spectral element Fourier code proposed by Blackburn *et al.* (2004).

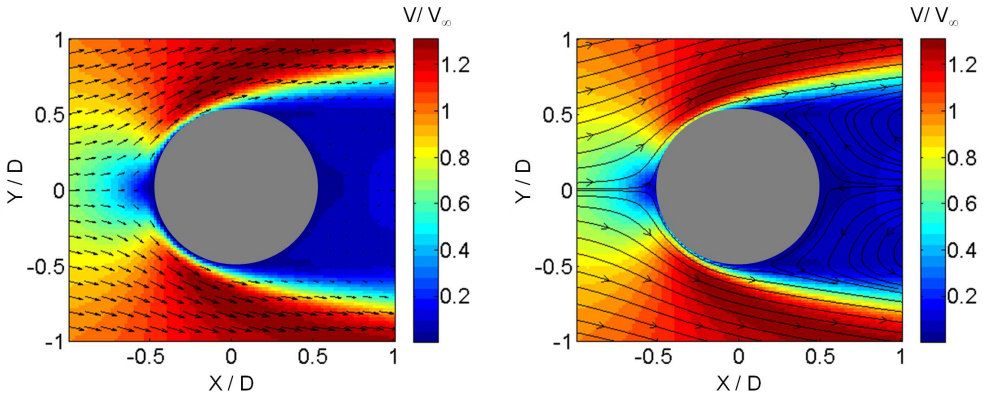

a) Absolute velocity. b) Streamlines.

Figure 3.6: Instantaneous DNS velocity field around a circular cylinder.

3.3.2.1 Circular Cylinder Flow, Re=200

The first test case used was unsteady, laminar flow, around a circular cylinder flow of diameter D at Re=200. Being computed by 2D-DNS, this velocity field, unlike those obtained via PIV, has neither missing out of plane vectors, nor under-resolved gradients. It will be thus very convenient in order to prove whether the proposed momentum-based method works, knowing that it is dealing with data free of uncertainties. DNS velocity data was re-sampled to a resolution of D/100, on a discrete grid of points, similar to what would be obtainable from a standard TR-PIV system.

The instantaneous velocity field describing the flow at time step t*=80 is shown in the left part of Figure 3.6. In this moment of the simulation, the Karman vortex shedding has not yet started, and two symmetrical big vortices form down-wash of the cylinder, as can be better seen in the right part of the figure, depicting the streamlines of the flow. As expected, an stagnation point forms when the fluid meets the cylinder at $\theta = 0^o$ (horizontal symmetry line, at x/D = -0.5).

In order to infer the aerodynamic forces impinged on the cylinder, the pressure gradient must be computed first. This is done using the ME in its differential form, using Equation 3.7. All data provided is non-dimensionalized and resolved in time (each field corresponds to a different time step). Three different velocity fields (corresponding to three consecutive time steps) are needed to infer the local acceleration of the flow (non steady terms).

Figure 3.7 and Figure 3.8 show a comparison between a) the pressure gradient calculated directly from DNS pressure data, and b) the pressure gradient calculated with the ME in its differential form. There is good agreement between these two, both for gradients in x direction and for gradients in y direction. In addition, the contributions of the different terms of Equation 3.7 to the total pressure gradients have been plotted in these figures in sections b.1), b.2) and b.3). The most important contribution comes from the convective acceleration, while the local acceleration (non steady terms) repercussion is very small. Finally, viscous terms gain importance in the boundary layer regions and in the wake.

Once the pressure gradient has been calculated satisfactory, allowing to validate both the methodology and its implementation, the entire pressure field around the cylinder must be computed. In fact, for the final load calculation, the pressure is only needed in the points

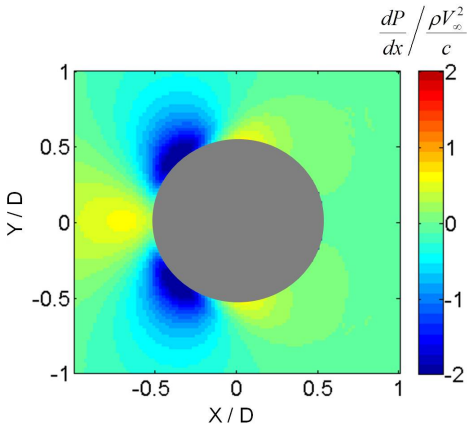

a) dp/dx derived from DNS data.

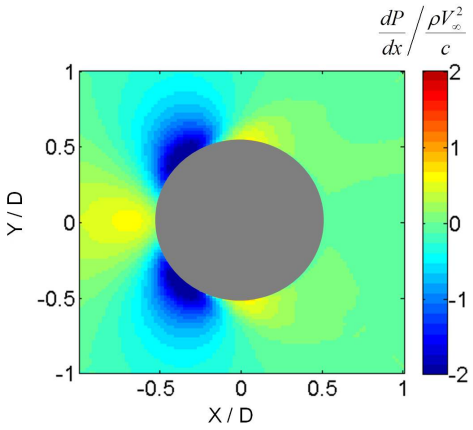

b) dp/dx calculated with ME

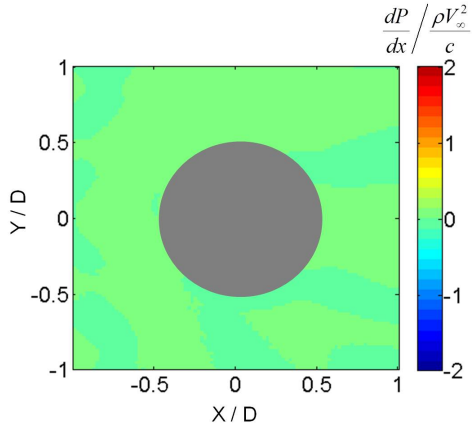

b.2) Non steady terms contribution.

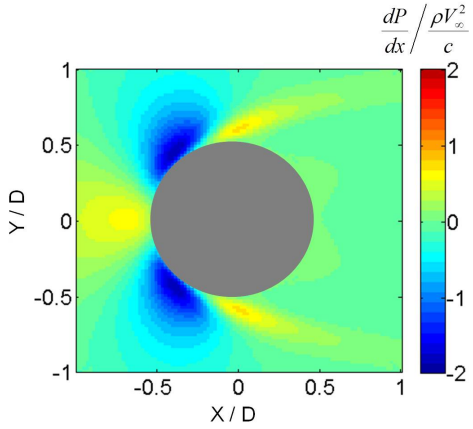

b.1) Convective terms contribution.

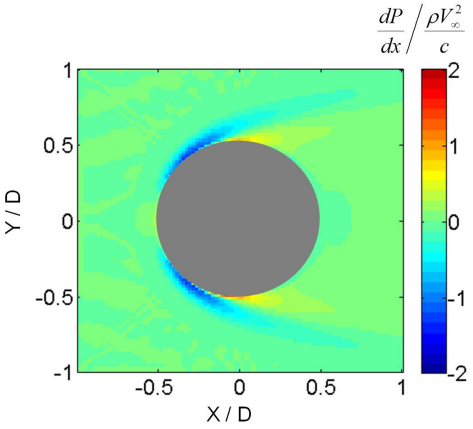

b.3) Viscous terms contribution.

Figure 3.7: Comparison of the pressure gradient dp/dx: a) derived from DNS pressure b) calculated with the ME methodology.

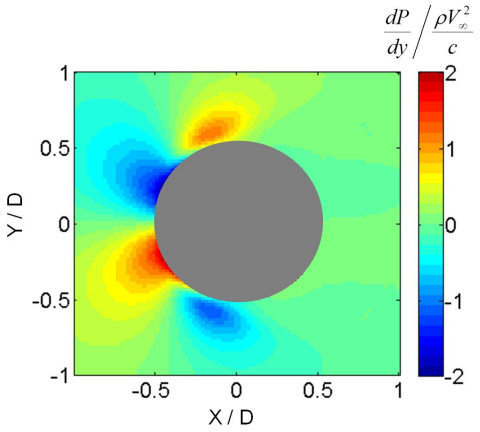

a) dp/dy derived from DNS data.

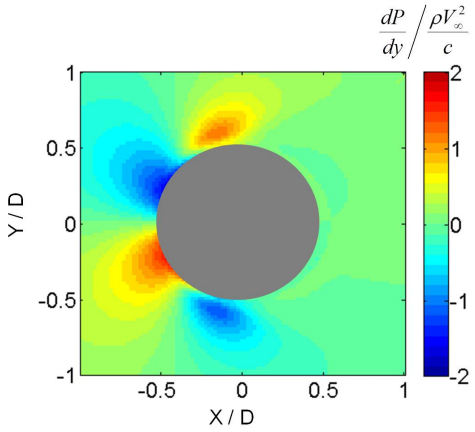

b) dp/dy calculated with ME.

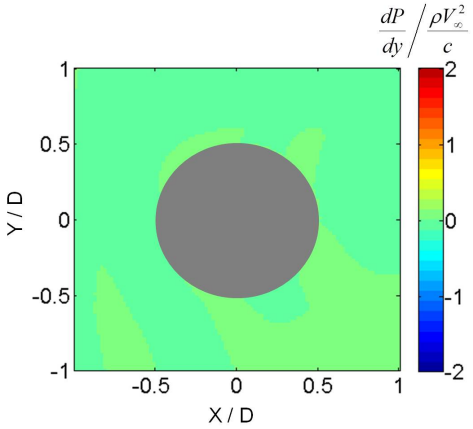

b.1) Non steady terms contribution.

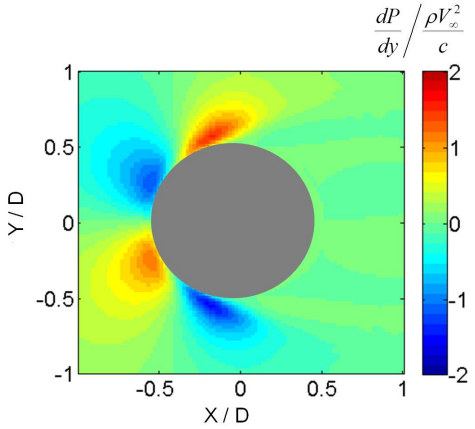

b.2) Convective terms contribution.

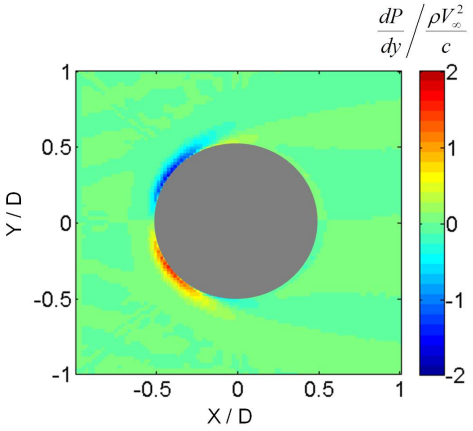

b.3) Viscous terms contribution.

Figure 3.8: Comparison of the pressure gradient dp/dy: a) derived from DNS pressure b) calculated with the ME methodology.

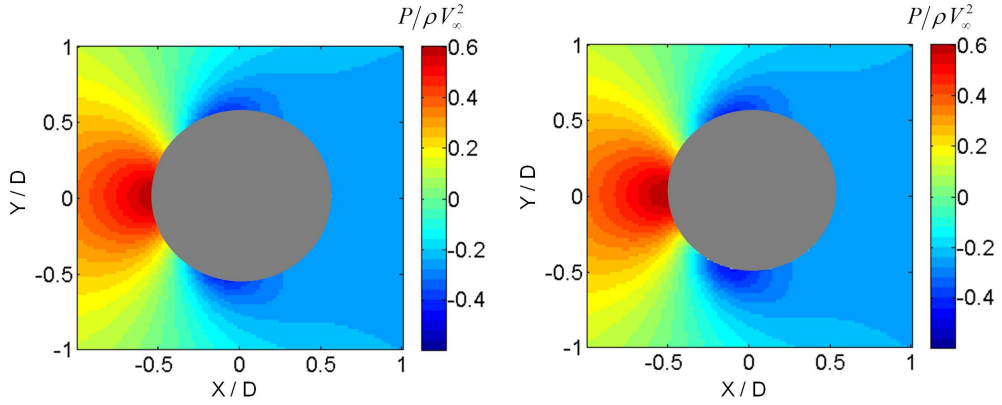

a) Provided by DNS. b) Calculated with the ME.

Figure 3.9: Comparison of the calculated pressure fields around the circular cylinder.

belonging to the integration path. However, calculating pressure only in these points through an integral marching scheme entails bigger accumulated error (see Section 3.3.1). It is for this reason that the pressure Poisson solver is used, as described in Equation 3.8 and Equation 3.9.

The comparison between the pressure obtained with the pressure Poisson solver and that provided by DNS is shown in Figure 3.9. Results show a very close agreement between these two, both qualitative and quantitative.

Finally, in order to calculate the lift and drag impinged, Equation 3.5 is applied using an integration path surrounding the cylinder. A rectangular path has been chosen for simplicity, but the shape of the path could be different, as long as it encloses the object. To see the influence of the integration path in the final results, 15 different rectangular control surfaces have been used, as it is depicted in Figure 3.10. The drag force calculation becomes more accurate when enlarging the integration path, when the magnitudes are calculated far from the cylinder surface and its boundary layer.

The mean values calculated with the ME approach and the standard deviation of the results obtained with 15 different integration paths are summarized in Table 3.1, with the parameters defined in Table 3.2. Mean values are very close to those provided by DNS; with absolute error of 0.003 for lift and 0.017 for drag. Furthermore, the standard deviation from the measurements, corresponding to the different integration paths, is also very small; 0.002 for lift and 0.001 for drag. These results conclude that, having accurate velocity data well resolved along all the field, the ME methodology brings a reliable way of measuring forces, independent of the integration path chosen.

However, the precision of the method has its limits, as can be seen in the relative error experienced in lift, up to 71.3%. The reason is that the lift coefficient has a very small value close to zero, $C_l = 0.004$. The precision of the method to calculate force coefficients reaches up to the tenth of unity.

Regarding the ME in its integral form (see Equation 3.5), it can be shown which terms are mainly responsible for the origin of the total forces. Figure 3.11 depicts how, in this case, pressure terms and convective terms have the biggest weight in the total computation of drag: indeed, pressure is pushing in the direction of the flow, increasing the drag, while the convective terms are holding, reducing the drag.

Force coefficients	Drag	Lift
DNS	1.069	0.004
ME (mean value)	1.086	0.001
ME (standard deviation)	0.001	0.002
Relative error	0.016	0.713
Absolute error	0.017	0.003

Table 3.1: Comparison of the circular cylinder force coefficients results.

Parameter	Description
Force coefficients	$c_f = \frac{f}{\frac{1}{2}\rho V^2 c}$
Mean value	$\mu = \frac{1}{N}\sum_{i=1}^{N} x_i$
Standard deviation	$\sigma = \sqrt{\frac{1}{N}\sum_{i=1}^{N}(x_i - \mu)^2}$
Absolute error	$\epsilon_{abs} = x - x_{ref}$
Relative error	$\epsilon_{rel} = \frac{x - x_{ref}}{x_{ref}}$

Table 3.2: Force coefficients comparison (standard deviation out of 15 different integration paths)

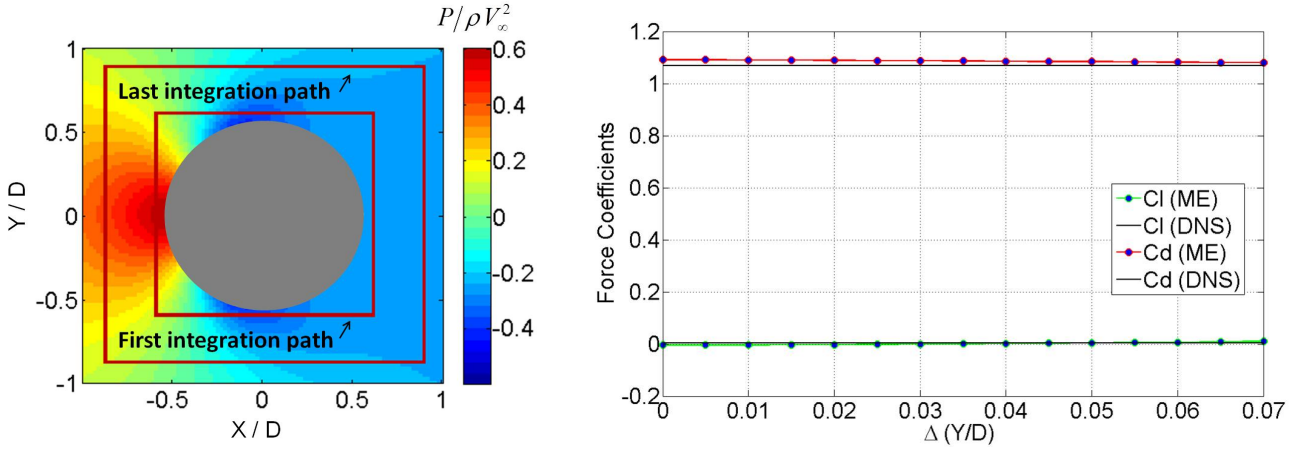

a) Integrations paths used to calculate loads.

b) Force coefficient results .

Figure 3.10: Influence of the integration path in the circular cylinder load calculation.

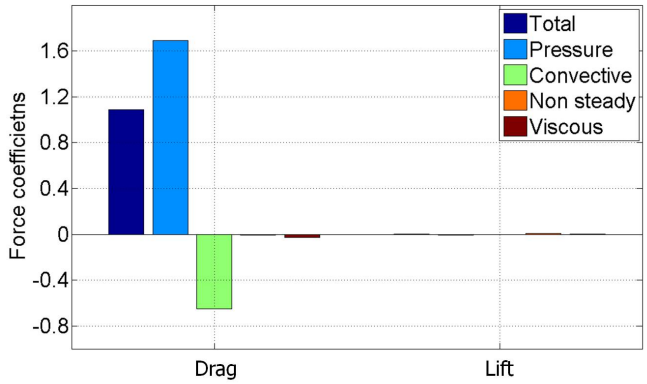

Figure 3.11: Contribution of the ME different terms to the circular cylinder load calculation.

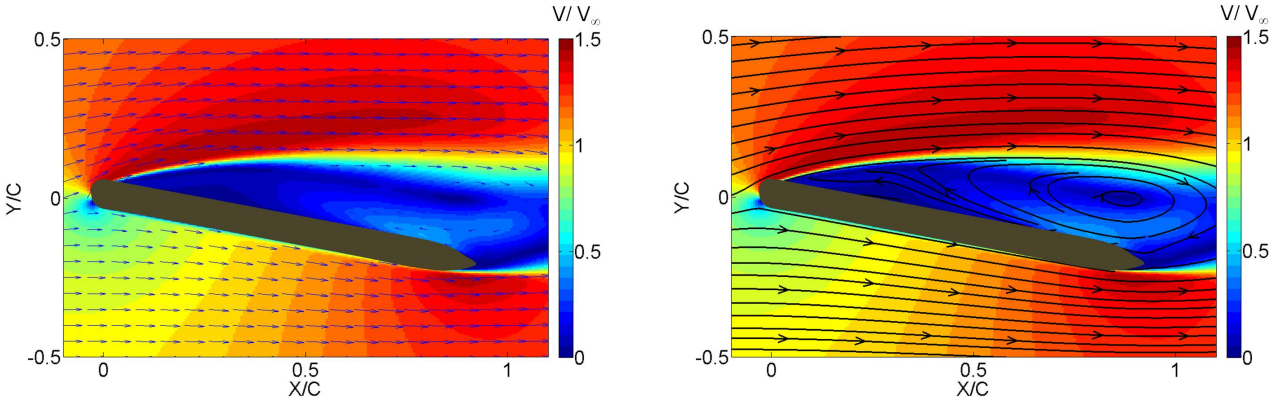

a) Absolute velocity. b) Streamlines.

Figure 3.12: Averaged DNS velocity field around the flat plate.

3.3.2.2 Inclined Flat Plate, Re = 10000

The second test case was chosen to estimate the accuracy achievable in flows with turbulent wakes. Thus, it was chosen to study the flow around a flat plate, inclined at an angle of attack $\alpha = 13^{\text{o}}$, at Reynolds number Re = 10000, computed by 3D-DNS. The flow separates near the leading edge, undergoes transition in the separated shear layer and intermittently reattaches, finally forming a turbulent wake. Figure 3.12 shows the velocity field around the flat plate, and its streamlines. DNS velocity data was re-sampled and averaged on a discrete grid of points, similar to what would be obtainable from a standard PIV system.

To account for turbulent fluctuations in the fluid Momentum, when averaging over the Navier-Stokes equations, the Reynolds Stress terms had to be considered in the formulation. Thus, Equation 3.11 is used to compute the pressure gradient, via the ME in its differential form. Velocities have been averaged and therefore no local acceleration is computed.

$$\begin{bmatrix} \frac{\partial p}{\partial x} \\ \frac{\partial p}{\partial y} \end{bmatrix} = -\rho \begin{bmatrix} u\frac{\partial u}{\partial x} + v\frac{\partial u}{\partial y} \\ u\frac{\partial v}{\partial x} + v\frac{\partial v}{\partial y} \end{bmatrix} - \rho \begin{bmatrix} \frac{\partial \overline{u'u'}}{\partial x} + \frac{\partial \overline{u'v'}}{\partial y} \\ \frac{\partial \overline{u'v'}}{\partial x} + \frac{\partial \overline{v'v'}}{\partial y} \end{bmatrix} + \mu \begin{bmatrix} \frac{\partial^2 u}{\partial x^2} + \frac{\partial^2 u}{\partial y^2} \\ \frac{\partial^2 v}{\partial x^2} + \frac{\partial^2 v}{\partial y^2} \end{bmatrix} \tag{3.11}$$

Force coefficients	Drag	Lift
DNS	0.314	1.021
ME (mean value)	0.315	1.035
ME (standard deviation)	0.000	0.006
Relative error	0.003	0.013
Absolute error	0.001	0.014

Table 3.3: Comparison of the flat plate force coefficients results

Figure 3.13and Figure 3.14 show the comparison between the pressure gradient derived directly from the DNS pressure data, and the pressure gradient calculated with the ME methodology. Both the pressure gradient with x direction and the pressure gradient with y direction coincide with those derived from DNS. Again, when analyzing the weight of each of the terms of the equation, the most relevant term is the convective acceleration, while the viscous stress terms are only noticeable in the separated shear layer. It is interesting to realize the important role of the Reynolds stress terms, without which the computed pressure gradient would not be correct at all.

Regarding pressure terms, a Poisson solver was used to reconstruct the whole field, as explained in Section 3.3.1, using the pressure gradients calculated before. Figure 3.15 presents the pressure field provided by DNS and that calculated with the ME, proving the good consistency of the two, and thus, validating again the suitability of the method and its implementation. The flat plate has a big suction region acting on the upper surface (even if the flow is disattached an has a recirculation region) and higher pressure acting on the lower surface, which altogether will originate a lift force. Regarding the direction parallel to the flow (that is, x direction), there is a higher pressure in the region near the leading edge, and a lower pressure region towards the trailing edge, which finally will represent an important drag source.

After having computed the pressure field, now all terms in the integral Momentum Equation are known, and aerodynamic loads can be calculated using Equation 3.12. Values in Table 3.3 show the force values provided by DNS as well as those computed by ME. In order to calculate the forces, 40 different rectangular integration paths have been used, and the Table collects the mean value of the resulting force coefficients, as well as their standard deviation. The first integration path has been drawn as close as possible to the flat plate, which means it crosses along its way the separated region of the flow. The rest of the considered paths grow bigger in the y-direction, outwards, as it is shown in Figure 3.16. The last integration paths are big enough to avoid the separated flow region, and therefore, they provide with better force coefficient results, specially regarding lift.

$$\begin{aligned}\begin{bmatrix} F_x \\ F_y \end{bmatrix} &= -\int_{aghi} \begin{bmatrix} p & 0 \\ 0 & p \end{bmatrix} \overrightarrow{n}\, ds + \int_{aghi} \mu \begin{bmatrix} 2\frac{\partial u}{\partial x} & \left(\frac{\partial u}{\partial y} + \frac{\partial v}{\partial x}\right) \\ \left(\frac{\partial u}{\partial y} + \frac{\partial v}{\partial x}\right) & 2\frac{\partial v}{\partial y} \end{bmatrix} \overrightarrow{n}\, \mathrm{d}s \\ &\quad - \int_{aghi} \rho \begin{bmatrix} uu & uv \\ uv & vv \end{bmatrix} \overrightarrow{n}\, \mathrm{d}s - \int_{aghi} \rho \begin{bmatrix} \overline{u'u'} & \overline{u'v'} \\ \overline{u'v'} & \overline{v'v'} \end{bmatrix} \overrightarrow{n}\, \mathrm{d}s \end{aligned} \tag{3.12}$$

On the whole, results are very promising, indicating the method is suitable to measure aerodynamic forces also in flows with turbulent wakes; regarding mean values of the force coefficients (from the 40 different control surfaces), the relative error is 0.3% for drag and

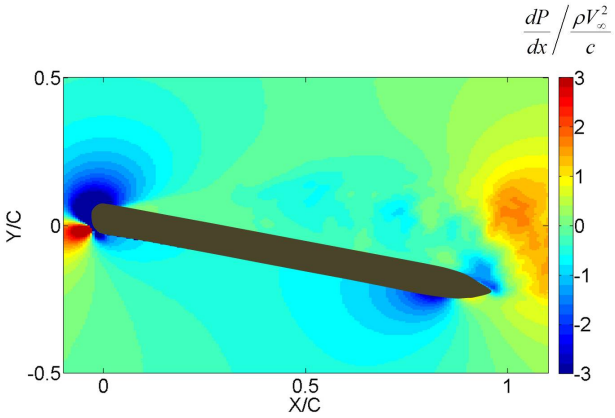

a) dp/dx derived from DNS data.

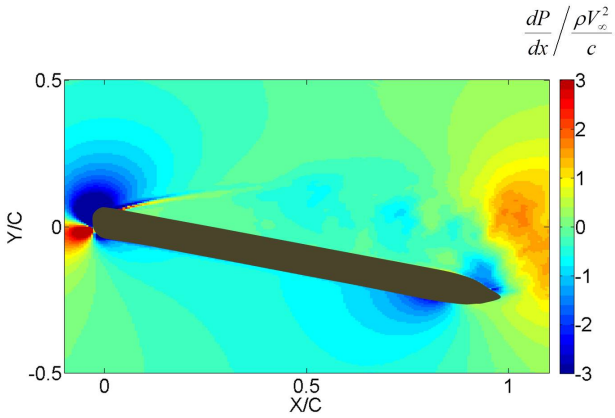

b) dp/dx calculated with ME.

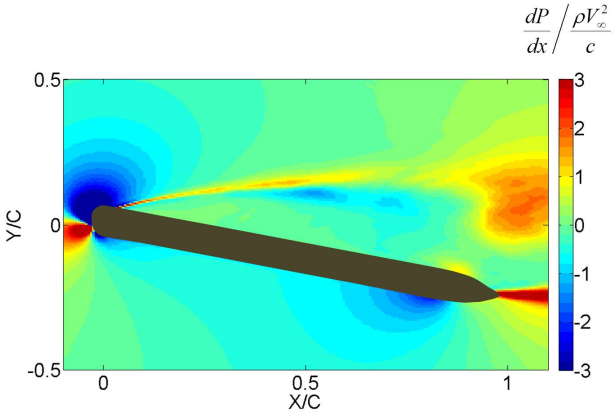

b.1) Convective terms contribution.

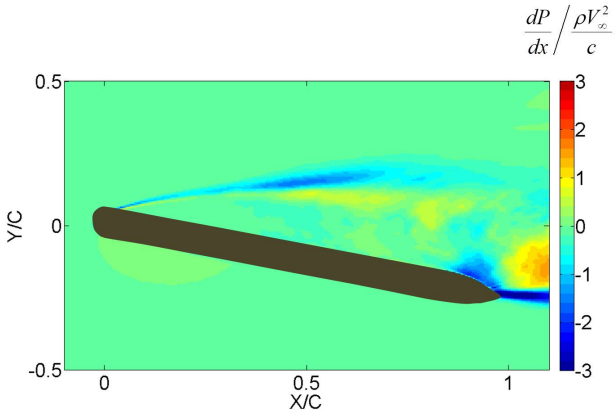

b.2) Reynolds stress terms contribution.

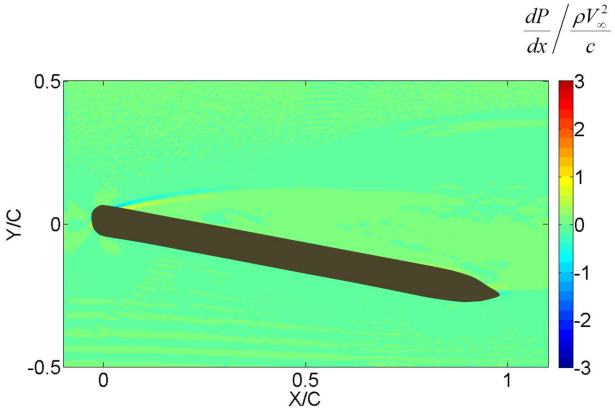

b.3) Viscous stress terms contribution.

Figure 3.13: Comparison of the pressure gradient dp/dx: a) derived from DNS pressure b) calculated with the ME methodology.

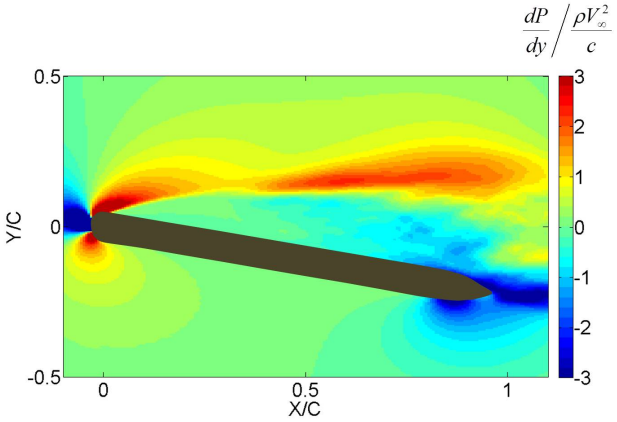

a) dp/dy derived from DNS data.

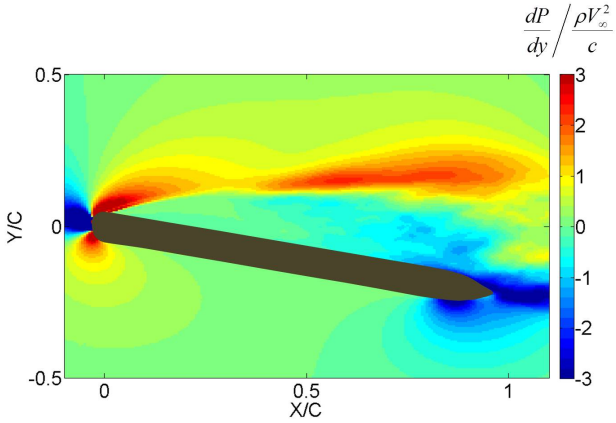

b) dp/dy calculated with ME.

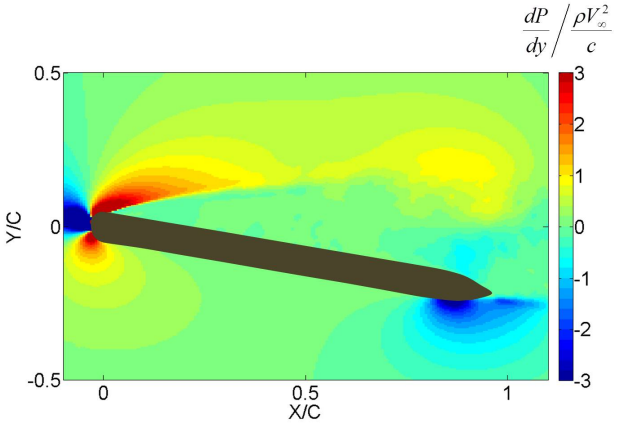

b.1) Convective terms contribution.

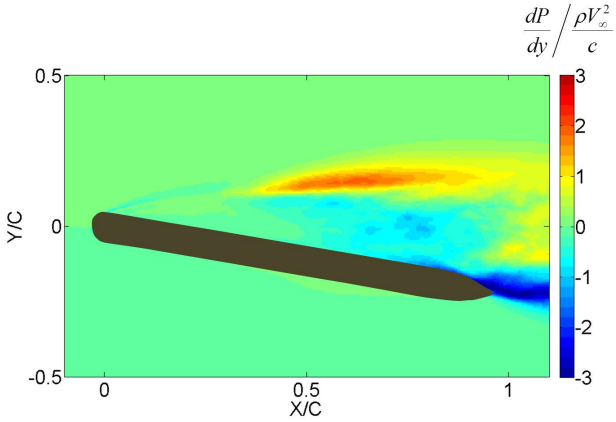

b.2) Reynolds stress terms contribution.

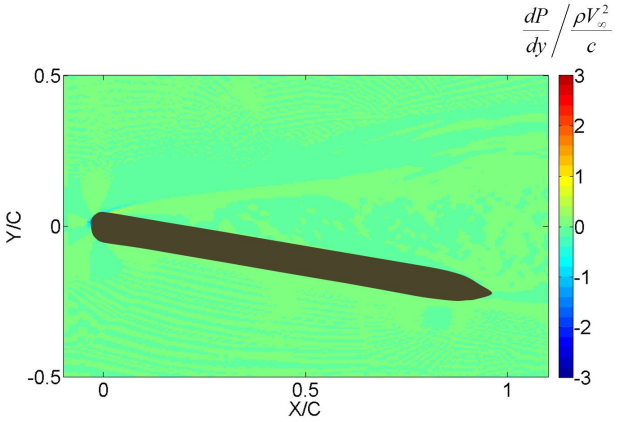

b.3) Viscous stress terms contribution.

Figure 3.14: Comparison of the pressure gradient dp/dy: a) derived from DNS pressure b) calculated with the ME methodology.

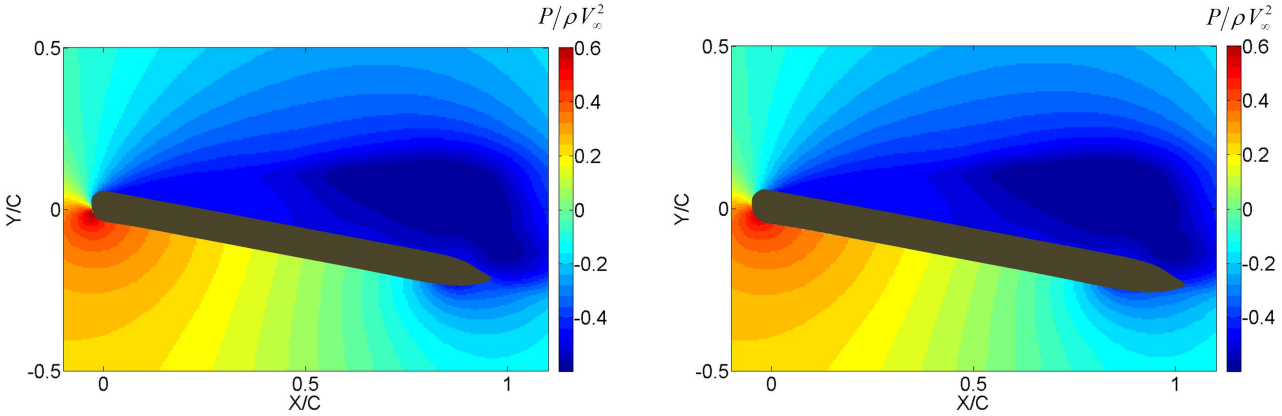

a) Provided by DNS. b) Calculated with the ME.

Figure 3.15: Comparison of the calculated pressure fields around the flat plate.

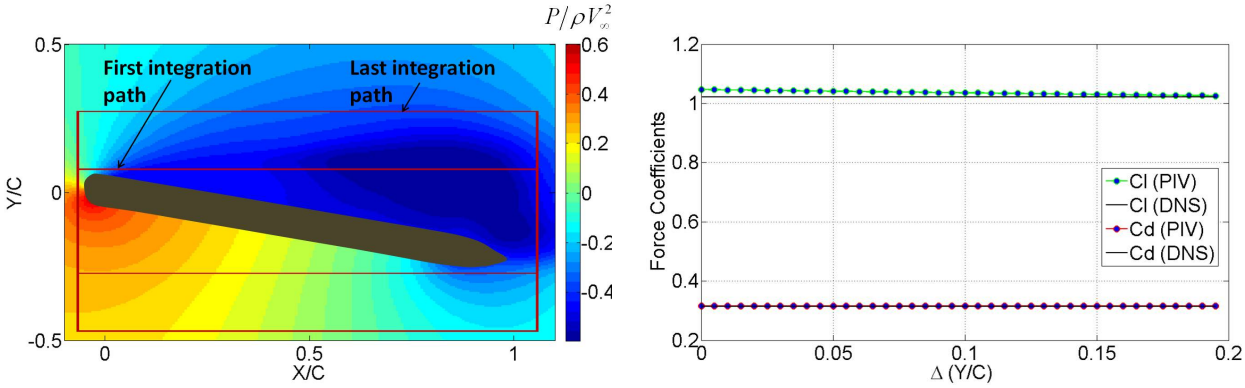

a) Integrations paths used to calculate loads. b) Force coefficients (comparison with DNS)

Figure 3.16: Influence of the integration path in the flat plate load calculation.

1.3% for lift, whereas absolute error is just 0.001 for drag and 0.014 for lift. Even though bigger integration paths result in more accurate coefficients, the difference between using one path or another is not big; the standard deviation from all measurements shrinks to 0.000 for the drag coefficient and 0.006 for the lift coefficient (parameter definitions are found in Table 3.2).

Finally, using optimized integration paths (that is, big enough to avoid the recirculation region), total forces as well as the different contributions from the ME in its integral form have been analyzed, as featured in Figure 3.17. Projecting the aerodynamic forces into the direction parallel and perpendicular to the undisturbed flow, it can be seen that pressure is the main source of drag, while the convective acceleration and its corresponding Reynolds Stress Terms are minimizing it. On the other hand, both pressure terms and convective acceleration terms contribute to create lift. Viscous terms in the ME are negligible in the global force computation. However, it is well known that an inviscid flow would create neither circulation nor disattachement of the flow and thus, if there was no viscosity, the resultant of all ME terms would be zero and there would be no aerodynamic forces impinged on the inclined flat plate (see Meseguer *et al.* (2005)).

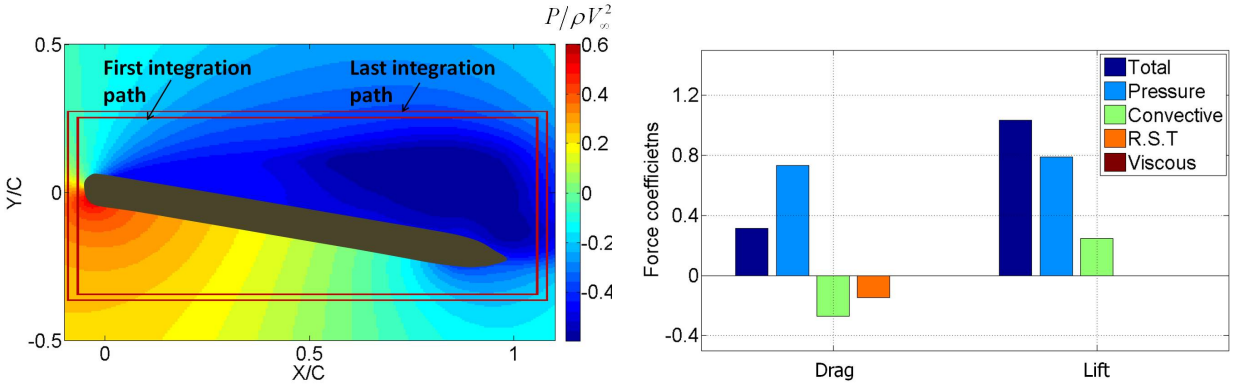

a) Optimized integrations paths used. b) Contribution of the ME terms.

Figure 3.17: Contribution of the ME different terms to the flat plate load coefficients.

3.4 Conclusions

The basic concepts of Particle Image Velocimetry have been explained in the beginning of this chapter, regarding seeding, illumination, image recording and processing. Besides, the methodology used to calculate forces out of velocities obtained with PIV, has been thoroughly described: the procedure is based in the Momentum Equation and uses a contour approach to estimate the loads impinged on a body by the fluid. In order to reconstruct the pressure field, it applies a Poisson solver, avoiding the error associated with a marching scheme.

The suitability of the method, together with its implementation, was validated using Direct Numerical Simulation data. The DNS data was re sampled to a resolution similar to what would be obtainable with a PIV system.

In the first place, the unsteady, laminar flow around a circular cylinder at Re=200 was considered. There was a very close agreement between the pressure provided with DNS and that calculated with the ME. The pressure gradient provided by the two sources was also compared showing good agreement. Actually, the contributions of the different terms of the ME, to the total pressure gradient, was analyzed: the result was that convective terms were the most important contributors, whereas viscous terms and unsteady terms had a very small influence.

To see the influence of the integration path in the final results, 15 different rectangular control surfaces were used. Mean values of the force coefficients were very close to those provided by DNS; with absolute error of 0.003 for lift and 0.017 for drag. The standard deviation from the measurements, corresponding to the different integration paths, was very small; 0.002 for lift and 0.001 for drag. The precision of the method to calculate force coefficients reached up to the tenth of unity, and the drag force calculation was sightly more accurate when enlarging the integration path, far from the cylinder surface and its boundary layer.

The second case was chosen to estimate the accuracy achievable in flows with turbulent wakes. Thus, the flow around an inclined flat plate ($\alpha = 13^{\text{o}}$) and Re =10,000 was studied. The flow separated near the leading edge, forming a turbulent wake. To account for turbulence, Reynolds stress terms were implemented in the steady formulation.

Both the comparison of the pressure gradient results, and the pressure reconstruction, showed good consistency with the data provided by DNS. Convective acceleration terms, and Reynolds stress terms, were the most important contribution to the pressure gradient. Regarding mean values of the force coefficients (calculated with the 40 different integration paths), absolute error is just 0.001 for drag and 0.014 for lift. Even though bigger integration paths result in more accurate coefficients (since they avoid part of the disattached flow, in the upper surface), the difference between using one path or another is small; the standard deviation is 0.000 for the drag coefficient and 0.006 for the lift coefficient

These results conclude that, having accurate velocity data, well resolved along all the field, the ME methodology brings a reliable way of measuring forces, independent of the integration path chosen.

Chapter 4

2D Load Calculation on a Flat Plate

4.1 Introduction

The main goal of this experimental campaign was to have simultaneous measurements of the forces impinged on an inclined flat plate both from a high sensitive balance and from 2D-PIV fields. This way, the loads calculated using PIV data could be compared with balance measurements obtained during the experiment itself.

Some studies have already tackled the problem of measuring forces in an airfoil (Van Oudheusden *et al.* (2006, 2007 and 2008) or Albrecht *et al.* (2011)), and in all cases the ways of validating the results were, either with numerical calculations or with pressure taps and wake rakes. However, using a force balance directly, allows to have simultaneous experimental results of the total forces impinged on the airfoil directly, avoiding uncertainties or lose of information because of indirect pointwise measurements and second calculations.

Actually, the flat plate chosen for the experiment had the same geometry as the one used in the Direct Numerical Simulation from Section 3.3.2.2 (rounded leading edge and wedge shaped trailing edge), and the first attempt was to simulate same experimental conditions as the ones imposed in the numerical simulation. However, given the geometry of the test chamber available, it was very difficult to achieve Re = 10,000 and still have precise balance measurements; the velocity inside the test chamber was too low (2m/s), the forces were too small, and the balance results were ambiguous.

Therefore, it was decided to run the wind tunnel at the lowest speed possible, that would still create forces that could be measured, reliably, by the balance; this velocity corresponded to Re = 30,000. In order to infer the influence of velocity and Re in the load calculation, the flat plate was also tested for Re = 70,000 and Re = 120,000. In all cases the measurements were carried out for different angles of attack ranging from $\alpha = 0°$ to $\alpha = 15°$. Thus, the airfoil loads could be calculated with fully attached flow, partially disattached and fully separated flow, and their corresponding turbulence levels.

In addition, the experiment provided with useful information about the stalling characteristics and the vortex shedding of a flat plate with a rounded leading edge. Historically, some studies had undertaken this theme: Fage & Johansen (1927), McCullough *et al.* (1951), and Chen *et al.* (1996), among others.

The project took place in the low speed wind tunnel of the Aerospace Laboratory at

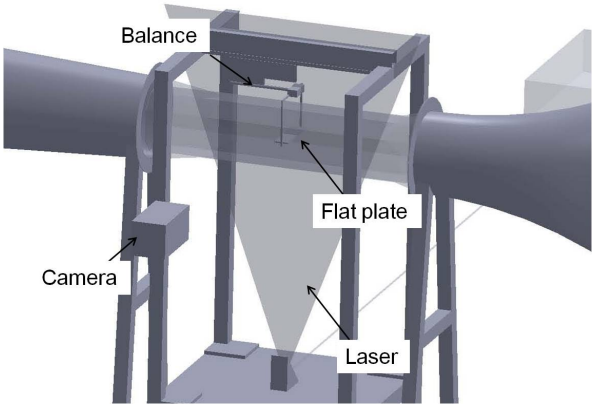

Figure 4.1: Scheme of the 2D PIV-Loads experimental set up.

the ETSEIAT, in Terrassa (Barcelona). Since the flat plate span coincided with the test chamber span, bidimensional conditions could be expected and a unique 2D-PIV plane in the middle of the flat plate was enough to calculate loads. It was a steady, yet turbulent, two-dimensional aerodynamic case.

4.2 Experimental Set Up and Conditions

The measurements were obtained in an open circuit wind tunnel with a closed test chamber that had a cross section size of $135\times160\text{mm}^2$. The flat plate model (chord $c = 44$mm, span $b = 135$mm and thickness $e = 3.3$mm) was built in methacrylate in order to ensure that the laser could go through it minimizing the shadowed areas. The leading edge of the flat plate was rounded and the trailing edge had a wedge form, so as to act as a thin airfoil with no camber. In order to maintain the flow undisturbed, the balance was placed outside of the wind tunnel and connected to the ends of the airfoil by means of an aluminum structure, as it is sketched in Figure 4.1. Figure 4.2 shows some photographs of the wind tunnel and the PIV experimental set up.

The flat plate was tested with four different angles of attack $\alpha = [0°, 5°, 10°, 15°]$, and three different free stream velocities $V_\infty(\text{m/s}) = [10, 25, 40]$ which corresponded to a Reynolds number based on chord equal to $\text{Re} = [0.3, 0.7, 1.2] \times 10^5$. Two hundred pairs of images were recorded, with a frequency of 7.5 Hz, for each operating condition. Simultaneously, the balance took measurements of both lift and drag forces. PIV velocity fields were averaged producing mean velocity fields, as well as their corresponding Reynolds stress terms. Balance results were also averaged and the standard deviation of each set of images was calculated. Table 4.1 summarizes the main experimental conditions.

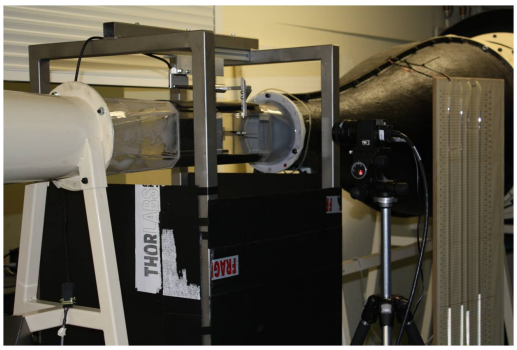

a) Wind tunnel and balance.

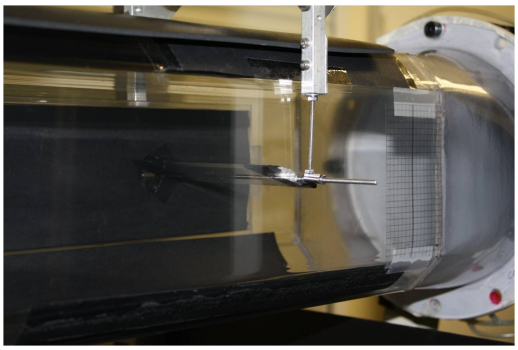

b) Test chamber and flat plate.

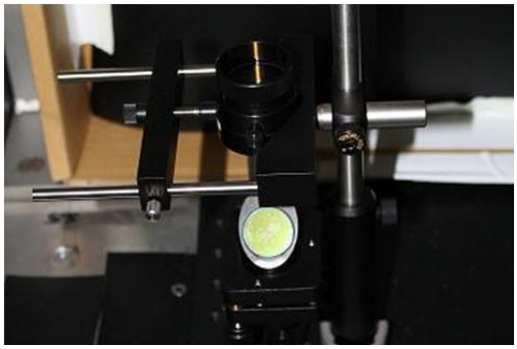

c) Mirror and optics.

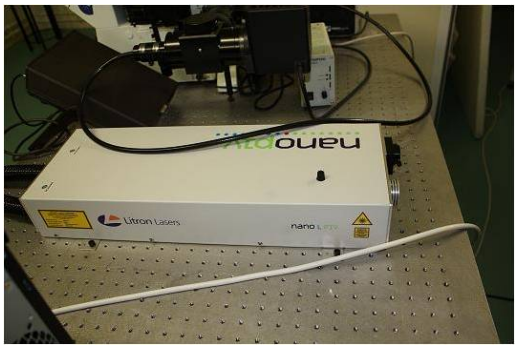

d) NdYag laser.

Figure 4.2: Details on the 2D PIV-Loads experimental set up.

Flat Plate Geometry	
Chord	44mm
Thickness	3.3mm
Relative thickness	0.075
Span	135mm
Angle of attack	$[0°, 5°, 10°, 15°]$
Material	Methacrylate

Experimental Conditions	
Free stream vel.	[10, 25, 40](m/s)
Reynolds number	$[0.3, 0.7, 1.2]\times10^5$
Temperature	21 ^{o}C
Test chamber	$135\times160\times400$mm^3
Bal. sensitivity	0.001N
Bal. acquisition	10Hz

Table 4.1: 2D PIV-Loads experimental conditions.

Illumination	
Laser type	Litron Nd:YAG
Energy per pulse	120 mJ
Wave length	$\lambda = 560$mm
Laser thickness	2mm
Frequency	7.5Hz (double pulse)

Seeding	
Fluid	Shell Ondina Oil15
Composition	Refined mineral oil
Particle density	≈ 1.20kg/m^3
Particle diameter	1.5 µm (median)
Fog generator	Teknova RG:100

Table 4.2: 2D PIV-Loads illumination and seeding characteristics.

A double cavity Litron Nd:YAG laser with a maximum power of 120mJ was used for illumination. The laser beam was directed through a cylindrical lens (r = 15mm) and a spherical lens (r = 500mm) in order to form a light sheet whose final thickness was 2 mm. The laser emitted in green with a wave length of 560mm and a frequency of 7.5Hz (per double pulse). The smoke particles used to seed the air had a median diameter of 1.5μm and were produced by a Teknova fog generator (RG:100) that used refined mineral oil. The smoke used produced throat irritations if inhaled during a prolonged period of time, therefore it was important to follow appropriate measures that enable the experimentalist not to breath it. Table 4.2 summarizes the main illumination and seeding conditions.

Images were obtained with a Powerview Plus PIV camera that was synchronized with the laser. It had a resolution of 2048 × 2048 px and was used together with a Nikon objective of 50mm focal length working with a diaphragm aperture of $f^\sharp = 11$. The images obtained were cropped in order to avoid the parts of the test chamber where the walls were not parallel to the laser light, thus resulting in a rectangular field of view of 110mm × 70mm size. For each case of study 200 couples of images were obtained with a laser pulse separation of 25μs, 10μs or 8μs, corresponding to the three different flow stream velocities tested. They were processed using the commercial software Insight 3G. The images had a resolution of 18px/mm and they were recursively cross-correlated using final interrogation windows of 16 × 16px with 25% overlap, which provided a spatial resolution of 0.89mm. Main imaging and acquisition parameters are presented in Table 4.3.

Imaging		**Acquisition and Processing**	
Camera	Powerview Plus	Int. window	48 × 48 ⇒ 16 × 16
Resolution	2048 × 2048 px	Overlap	25%
Focal length	50 mm	Image resolution	18px/mm
Diaph. aperture	11	Spatial resolution	0.89mm
Field of view	≈ 110mm × 70mm	Pulse separation	[25, 10, 8](μs)

Table 4.3: Imaging and acquisition parameters.

4.3 2D Load Calculation Procedure.

Aerodynamic loads exerted on the inclined flat plate were calculated following the ME approach already explained in Section 3.3.1. This time, the case of study is steady and two dimensional. Moreover, the flow can be considered incompressible and, since the flat plate is not moving, a stationary frame of reference whose origin is placed on the airfoil itself can be used. Thus, the ME expressed in Equation 3.5 can be simplified and converted into Equation 4.1, where F_x represents the drag force per unit length exerted on the airfoil and F_y represents the lift force per unit length

$$\begin{bmatrix} F_x \\ F_y \end{bmatrix} = -\int_{aghi} \begin{bmatrix} p & 0 \\ 0 & p \end{bmatrix} \vec{n}\, ds + \int_{aghi} \mu \begin{bmatrix} 2\frac{\partial u}{\partial x} & \left(\frac{\partial u}{\partial y} + \frac{\partial v}{\partial x}\right) \\ \left(\frac{\partial u}{\partial y} + \frac{\partial v}{\partial x}\right) & 2\frac{\partial v}{\partial y} \end{bmatrix} \vec{n}\, \mathrm{d}s$$
$$- \int_{aghi} \rho \begin{bmatrix} uu & uv \\ uv & vv \end{bmatrix} \vec{n}\, \mathrm{d}s - \int_{aghi} \rho \begin{bmatrix} \overline{u'u'} & \overline{u'v'} \\ \overline{u'v'} & \overline{v'v'} \end{bmatrix} \vec{n}\, \mathrm{d}s \tag{4.1}$$

Pressure terms are calculated using the Poisson solver, as described in Section 3.3.1. The ME used in its differential form to compute the pressure gradient transforms into Equation 4.2 when applied to the present case.

$$\begin{bmatrix} \frac{\partial p}{\partial x} \\ \frac{\partial p}{\partial y} \end{bmatrix} = -\rho \begin{bmatrix} u\frac{\partial u}{\partial x} + v\frac{\partial u}{\partial y} \\ u\frac{\partial v}{\partial x} + v\frac{\partial v}{\partial y} \end{bmatrix} - \rho \begin{bmatrix} \frac{\partial \overline{u'u'}}{\partial x} + \frac{\partial \overline{u'v'}}{\partial y} \\ \frac{\partial \overline{u'v'}}{\partial x} + \frac{\partial \overline{v'v'}}{\partial y} \end{bmatrix} + \mu \begin{bmatrix} \frac{\partial^2 u}{\partial x^2} + \frac{\partial^2 u}{\partial y^2} \\ \frac{\partial^2 v}{\partial x^2} + \frac{\partial^2 v}{\partial y^2} \end{bmatrix} \tag{4.2}$$

4.4 Experimental Results

During the tests performed in the wind tunnel, the airfoil was mounted upside down, i.e, the suction side was physically below the pressure side, as can be seen in the right part of Figure 4.2. This was done on purpose because, due to the bars that connected the airfoil to the balance, there was a thin region in which data had to be interpolated. Thus, it was easier to interpolate data in the pressure side where the flow was attached and laminar. Moreover, even if the airfoil was built in methacrylate, laser reflections could not be removed completely, having to draw a big mask around the flat plate before processing the images. In this masked area no velocity information could be obtained.

While the laser and the cameras were capturing PIV images, the balance was simultaneously recording lift and drag forces measured on the flat plate, with a 10Hz frequency. Table 4.4 shows the force coefficients provided by the balance as well as their standard deviation values.

Absolute velocity fields, non-dimensionalized with the free stream velocity, are shown in Figure 4.4 (*left:* $V_\infty = 10\,\mathrm{m/s}$ and *right:* $V_\infty = 40\,\mathrm{m/s}$ corresponding to Re = 30,000 and Re = 120,000 respectively). The figure shows the velocity fields obtained with 4 different angles of attack inspectioned. As it can be seen, the non dimensionalized velocity fields for the same angle of attack at different Re are consistent with each other, which means a similar aerodynamic problem is faced for the three Re considered in the experiment ($\mathrm{Re} = [0.3, 0.7, 1.2] \times 10^5$).

Regarding $\alpha = 0°$, the aerodynamic problem is symmetric and, theoretically, there should be no lift; there is a thin, horizontal viscous wake coming from the trailing edge. For $\alpha = 5°$, the boundary layer has disattached in the last half of the plate. For $\alpha = 10°$ flow is disattached in three quarters of the flat plate and finally, for $\alpha = 15°$, the flow is fully separated, starting from the leading edge. Thus, the separation starts in the trailing edge and the separated flow occupies more area of the flat plate if the angle of attack is increased. This is achieved gradually, until the flow is fully separated. Taking in account that the relative thickness of the flat plate is $\frac{t}{c} = 0.075$, it was observed that the way the flat plate stalls does not follow the description offered by McCullough & Goult (1951),

Re = 30,000	C_l	σ_{C_l}	C_d	σ_{C_d}
$\alpha = 0°$	0.096	0.084	0.012	0.043
$\alpha = 5°$	0.537	0.095	0.048	0.046
$\alpha = 10°$	0.649	0.108	0.082	0.064
$\alpha = 15°$	0.669	0.117	0.137	0.064

Re = 70,000	C_l	σ_{C_l}	C_d	σ_{C_d}
$\alpha = 0°$	0.060	0.015	0.064	0.008
$\alpha = 5°$	0.506	0.020	0.104	0.009
$\alpha = 10°$	0.773	0.023	0.183	0.011
$\alpha = 15°$	0.887	0.027	0.328	0.013

Re = 120,000	C_l	σ_{C_l}	C_d	σ_{C_d}
$\alpha = 0°$	0.066	0.006	0.063	0.005
$\alpha = 5°$	0.602	0.015	0.128	0.006
$\alpha = 10°$	0.713	0.019	0.190	0.007
$\alpha = 15°$	0.960	0.024	0.393	0.010

Table 4.4: 2D PIV-Loads balance results (mean and standard deviation values).

who presented three representative types of airfoil-section stall at low speed, based on their relative thickness. According to this reference, in a thin airfoil (as NACA 64A006), a recirculation bubble is created in the leading edge and it grows as the angle of attack is increased, until an angle in which the bubble explode, leaving the airfoil with fully separated flow all of a sudden. The reason for the flat plate not to follow this tendency could be that its shape is not so aerodynamic, there is no camber line, and no reduction of thickens towards the leading edge.

A better insight of the fluid dynamics of the experiment is observed in Figure 4.5 which shows; on the left, the vorticity contours of the flow, and on the right, the flow streamlines (for Re = 70,000 and whole range of angles of attack). It clearly depicts vortices of opposite signs being originated from the leading edge and the trailing edge of the flat plate, respectively, for the case of fully separated flow $\alpha = 15°$.

The vortex shedding created by an inclined flat plate has been widely considered in the literature. According to Chen *et al.* (1996) , the Reynolds number has no discernible effects on the relation between the Strouhal number ($\mathrm{St} = \frac{\mathrm{f \cdot c \cdot sin\alpha}}{\mathrm{V_\infty}}$) and the angles of attack, in the range of $\alpha = 10° - 90°$, with fully separated flow. Thus, an universal Strouhal number of $\mathrm{St} = 0.160 \pm 0.003$ was obtained for these cases. Similar results are found in Fage & Johanson (1927). This value of St provides with the frequency of the vortex shedding that is taking place in the leading edge, as can be seen in Table 4.5. However, neither the acquisition frequency of the PIV system nor that of the balance is high enough to characterize the frequency of the vortex shedding. Thus, this phenomenon will cause and oscillation in lift that the PIV-ME loads methodology will not be able to capture, unless TRPIV were used.

In order to have a better insight of the fluid dynamics of the problem, a Reynolds Average Numerical Simulation (RANS) was undertaken, imposing $\mathrm{Re} = 70,000$, V_∞= 25m/s and $\alpha = 15°$. Part of the results obtained are shown in Figure 4.3, where a oscillation of the lift coefficient is a direct consequence of a vortex shedding frequency $f = 350$Hz, consistent

V_∞[m/s]	10	25	40
f [Hz]	140	351	562

Table 4.5: Flat plate vortex shedding frequency ($\alpha = 15°$).

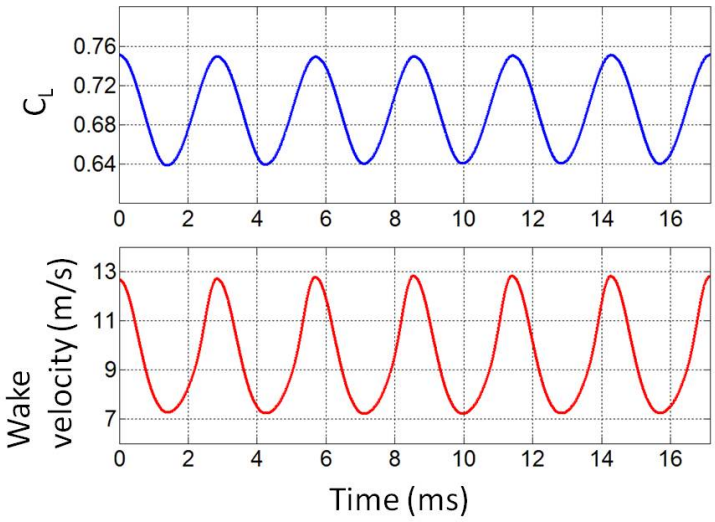

Figure 4.3: Flat plate time resolved lift coefficient (Re = 70,000 and $\alpha = 15°$).

with the aforementioned literature. The computation was done using Fluent software and a $k - \epsilon$ turbulence model. Further information on the procedure can be found in Lara *et al.* (2011).

Figure 4.6 depicts how as the angle of attack grows, there is an increase in the acceleration of the flow near the leading edge and a the deceleration of the flow in the lower surface of the plate, and how this tendency is interrupted in the suction side in the regions where the flow is separated. The figure shows velocities in x and y directions, non dimensionalized with the free stream velocity, for Re = 70,000.

Following the methodology explained in Section 4.3, the pressure field was calculated for each of the cases studied. Figure 4.7 depicts, on the right, the calculated pressure field around the flat plate, for Re =70,000. On the left, the figure shows pressure fields calculated with Bernoulli equation (see Equation 3.10), showing the large error generated in the wake region if pressure were calculated this way. In addition, this figure shows how pressure is contributing to create lift and drag; the higher the angle of attack, the bigger is the net contribution from pressure to both forces.

It must be noted that in order to calculate forces, a rectangular mask (where all velocities are set to zero) was drawn, adjusted to the PIV mask used to process velocities. Besides, derivatives of velocities were needed all over the field to calculate pressure; therefore the mask was enlarged by 0.02 times the chord in this step.

Once the pressure around the flat plate was known, the aerodynamic forces were calculated (per unit length). Figure 4.9, Figure 4.10 and Figure 4.11 show the result of drag and lift for the different control surfaces used. Since the physical problem that is being studied is two-dimensional, the control surface, that in this case would be a cube, reduces to a rectangular integration path. The first rectangular integration path chosen is the smallest

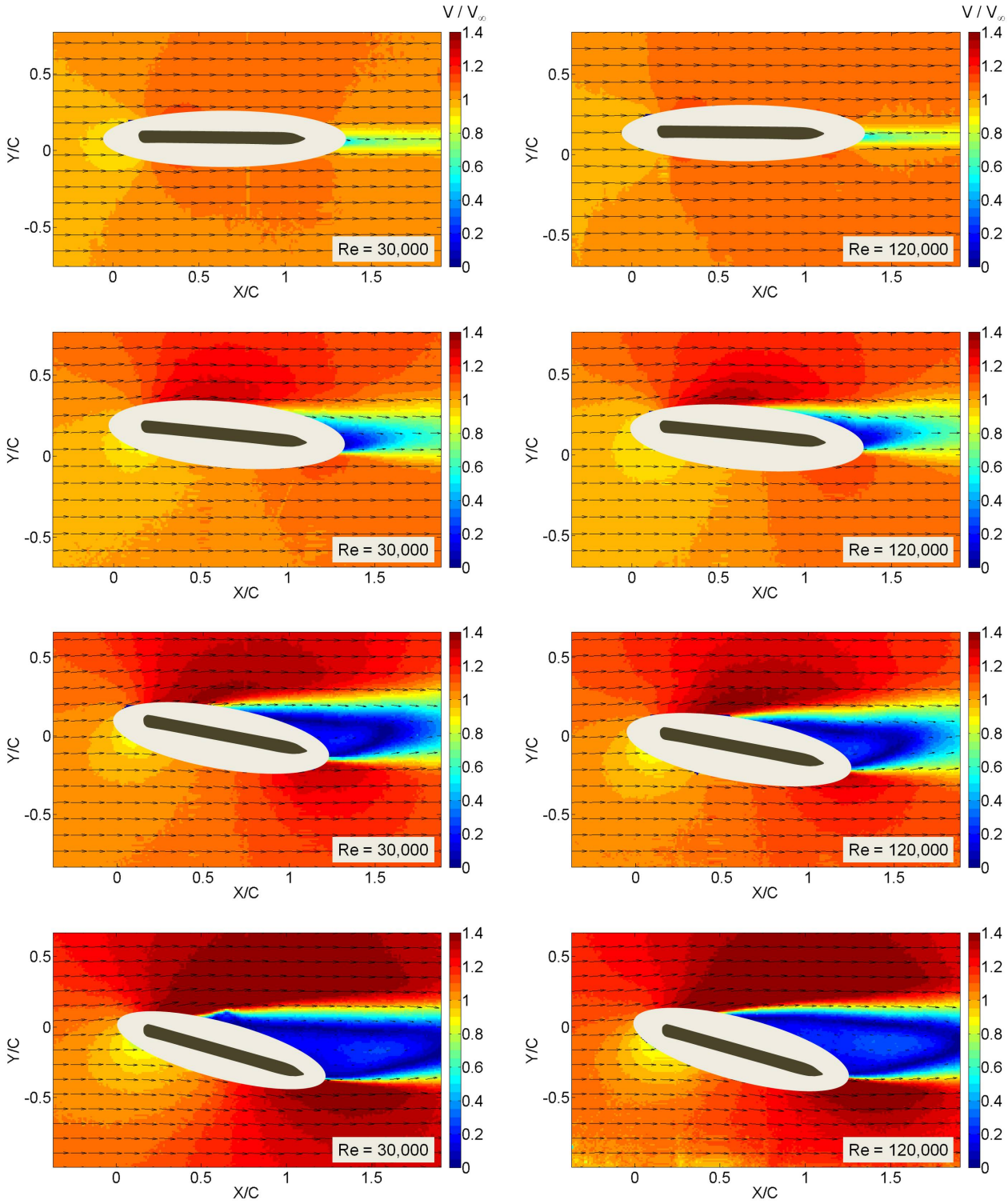

Figure 4.4: Flat plate absolute velocity fields obtained with PIV ($\alpha = 0°$, $5°$, $10°$, $15°$).

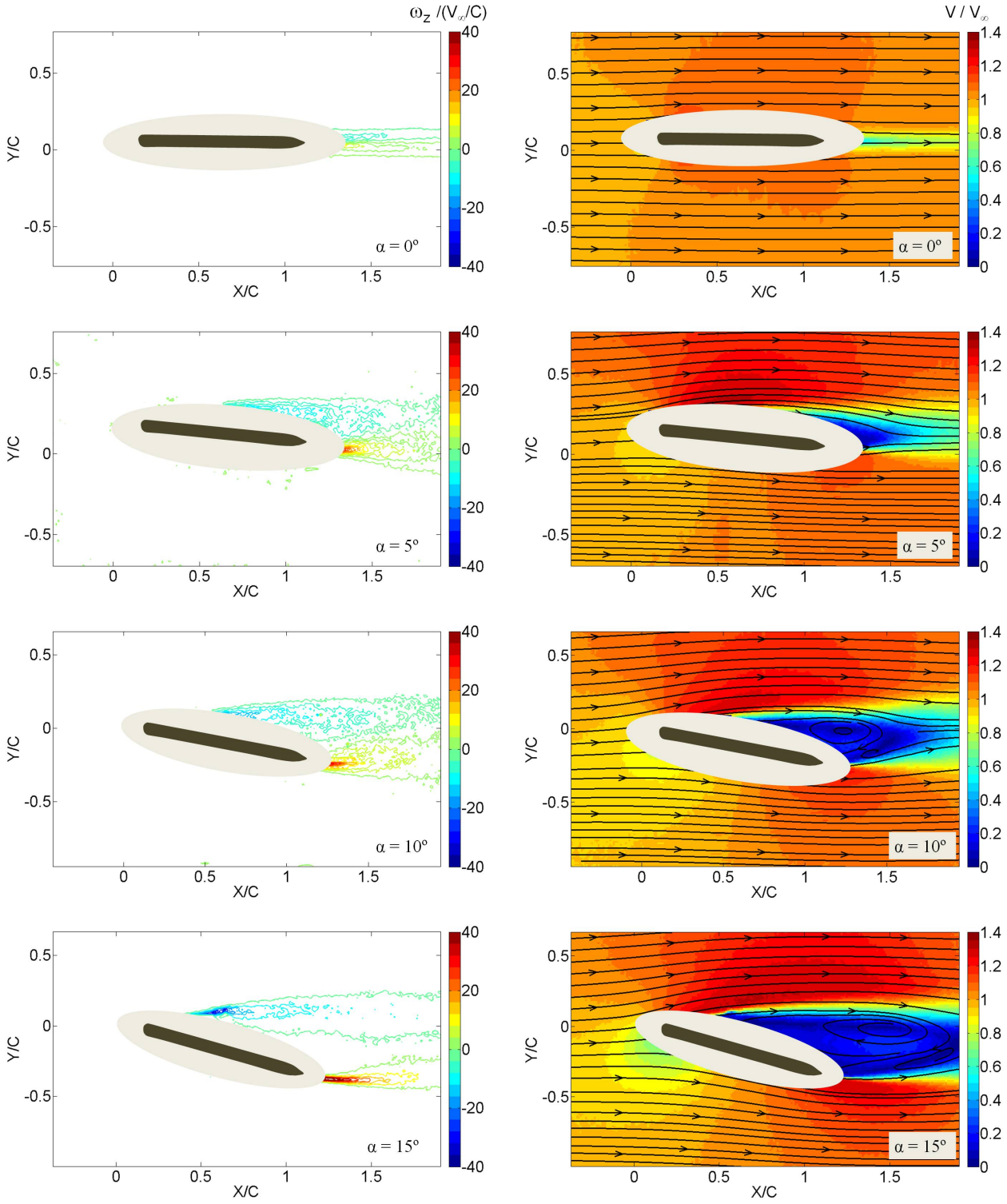

Figure 4.5: Flat plate vorticity contours *(left)* and streamlines *(right)* for Re = 70,000.

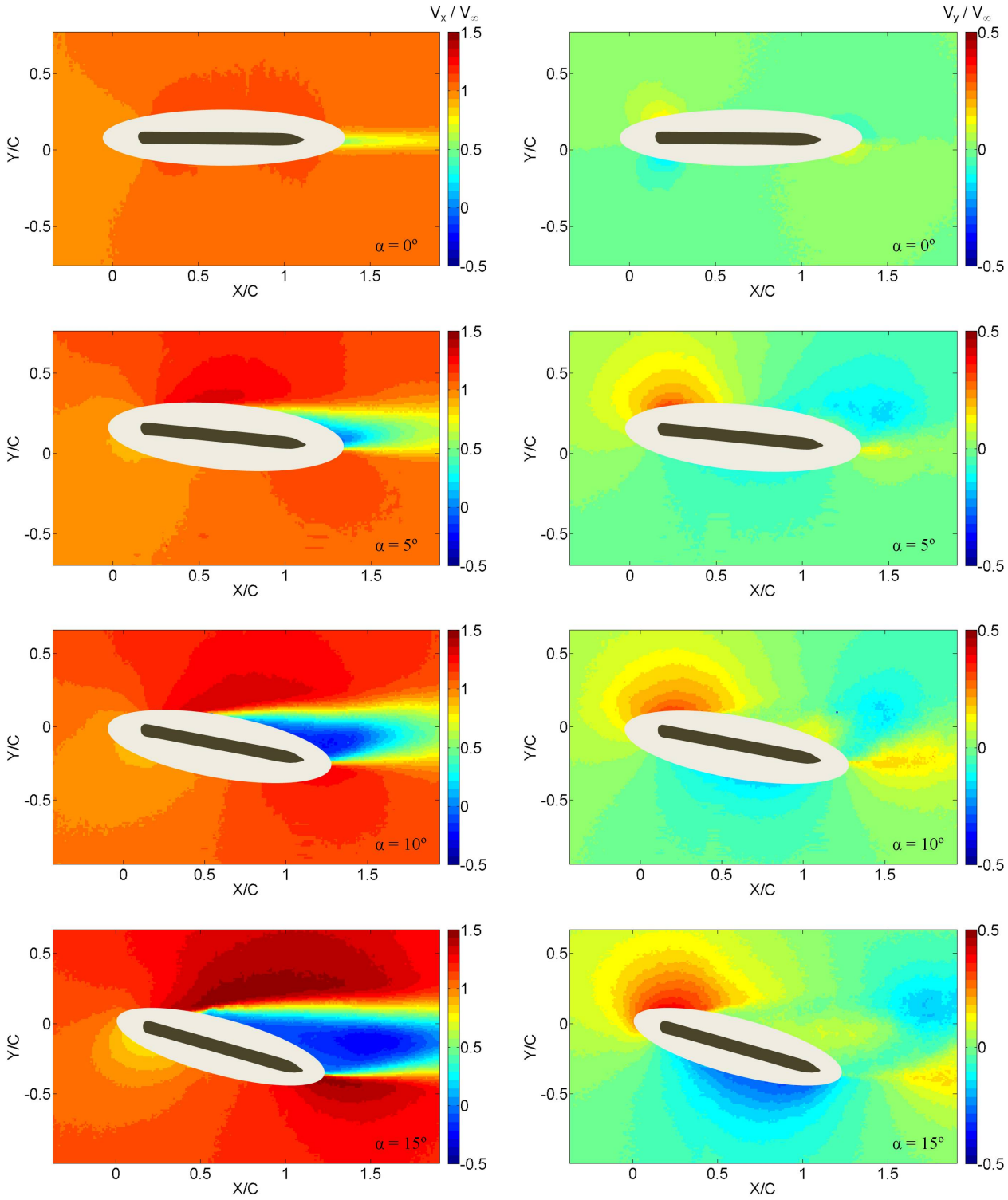

Figure 4.6: Flat plate velocity fields obtained with PIV for Re = 70,000.

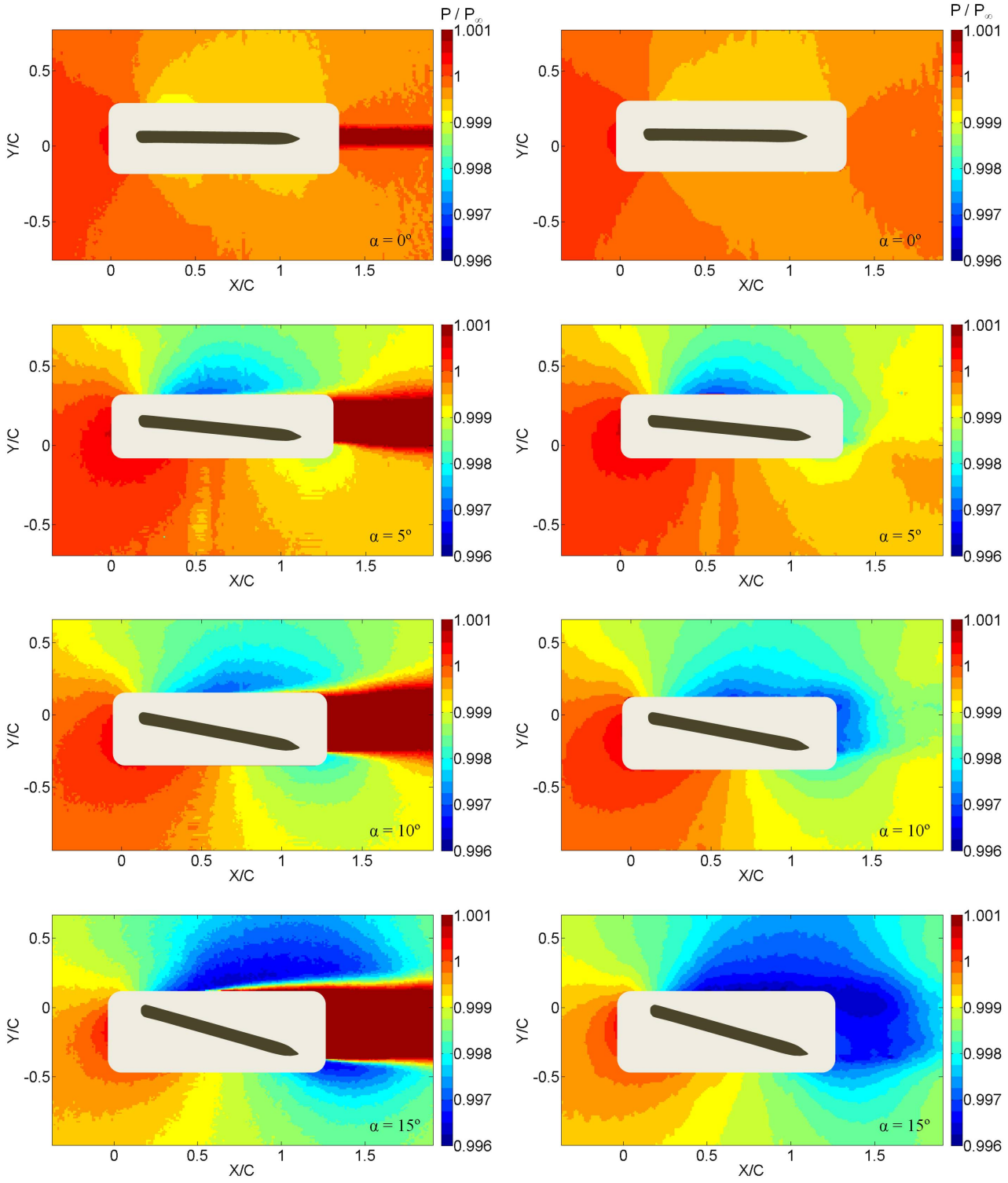

Figure 4.7: Flat plate calculated pressure fields for Re = 70,000 (*left:* Bernoulli, *right:* Poisson solver).

possible enclosing the PIV flat plate mask, and the next paths grow outwards, separating a distance Δ from each previous wall, as depicted in Figure 4.8, until the last path is reached, which is the biggest possible that can be included in the image.

Looking at these three figures, it is obvious that the first three points on the graphics are always erroneous. The reason for this is, either there was no pressure information in any of the path walls (first two points), or there was some wall of the path in which pressure had not been calculated (third point). Thus, these three first points can not be considered as a good calculation. Nevertheless, these points are shown in the dissertation in order to prove the relevance of the pressure term in the force calculation.

On the one hand, the consistency of drag results between the balance and the PIV-Loads method is better when using an integration path close to the mask (0.1-0.2 times the chord). For high angles of attack, $\alpha = 10° - 15°$, the drag value calculated with PIV grows with bigger integration paths that are further from the mask. On the other hand, the lift values are not influenced by the integration path chosen.

On the whole, there are some difference between the balance measurements and the ME load calculation with PIV, and the tendency is similar for the three Re considered. Taking into account that the method responded accurately when using DNS data, the disagreement in the results are most possibly due to uncertainties in the measurements:

- Regarding the balance, 3D effects could be a possible source of errors; there is a very thin gap between the flat plate and the test chamber wall, otherwise the flat plate would be fixed by the test chamber and the balance would not be measuring real forces on it...but this, in turn, may cause small tip vorticity. On the other hand, considering the aluminum structure that holds the balance, although it has been carefully optimized in this way, it could be introducing small vibrations that alter the measurements.

- Regarding PIV measurements, lack of resolution and velocity gradients inside the interrogation windows chosen are the main sources of error. This is particularly important in the wake, where the turbulence and the vorticity is greater. Therefore, drag measurements are less accurate, and vary significantly depending on the integration path chose. It is interesting to mention how the thin interpolated area in the pressure side or the flat plate does not hinder having good results in lift: on the contrary, lift calculation are more precise and remain constant regardless of the integration path chosen.

When computing forces, it is observed that the results do no vary much if Reynolds stress terms are ignored in the formulation. Figure 4.12, Figure 4.13 and Figure 4.14 try to bring some light into this issue. This figures show the resultant of the forces:

- PIV with RST: Using Reynolds stress terms to calculate the pressure gradient (Equation 3.11) and to calculate forces (Equation 3.12).

- PIV without RST: Ignoring the Reynolds stress terms both in Equation 3.11 and in Equation 3.12.

- PIV (f with RST): Using Reynolds stress terms only to calculate forces (Equation 3.12), but ignoring them when computing the pressure gradient (Equation 3.11) .

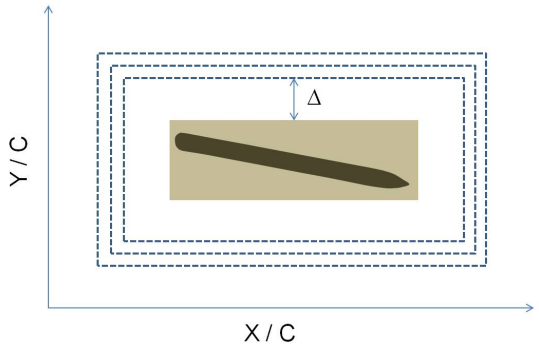

Figure 4.8: 2D PIV-Loads contours used as integration paths.

- PIV (p with RST): Using Reynolds stress terms only to calculate the pressure gradient (Equation 3.11), but ignoring them when computing forces (Equation 3.12).

At first sight, it would seem that the first two options (PIV with RST and PIV without RST) provide identical results, as if the the Reynolds stress terms canceled themselves when introducing the pressure term in the integral ME. This is not true, and in the figures showing drag, it is clear that the results of these two ways of computing forces do not always coincide, although they are very close to each other. The explanation to this phenomenon can be obtained when considering the last two options, i.e, (PIV (f with RST) and PIV (p with RST)) : it is evident that the Reynolds stress terms in the differential ME and in the integral ME are introducing opposite tendencies in the total load calculation. This is the reason why, when ignoring them altogether, the force, in this case, does not change much. However, if an accurate pressure field needs to be reconstructed, it is essential to take into account the Reynolds stress terms, as was proven in Section 3.3.2.2.

Moreover the impact of Reynolds stress terms in drag computation is very high, since one of the integration path walls involved in this force measurement directly crosses the wake, which is the region where most turbulence is involved. Whereas, regarding lift, no differences are encountered regardless of the option chosen.

Finally, mean forces (Figure 4.16) and mean force coefficients (Figure 4.17) are calculated and compared with the balance results. In order to avoid the uncertainty introduced in the drag by the turbulent flow, only five integration paths were used, avoiding crossing the wake as much as possible. The first path used to get these results is depicted in Figure 4.15, for each angle of attack.

In general, there is a good agreement between both methods, although small differences are encountered in all cases, whose sources of uncertainties have been already discussed. Experimental measurements, conducted in a flat plate for Re = 42,000 by Schmitz (1942), have been included in the figure as a reference, showing good agreement with the balance measurements at Re = 30,000.

In general, the effect of Re in the curves $C_L - \alpha$ and $C_D - \alpha$ in an airfoil is that, the higher the Re, the smaller the drag, for the same angle of attack (see Franchini & Lopez Alegria (2011)). The reason for this is, at higher Re, the boundary layer of the airfoil becomes turbulent, thus delaying the separation of the flow, producing a thinner wake, and therefore, less pressure drag. However, this is not the case in our study. It can be observed that, for same the α, the higher the Re, the higher is the drag coefficient. For

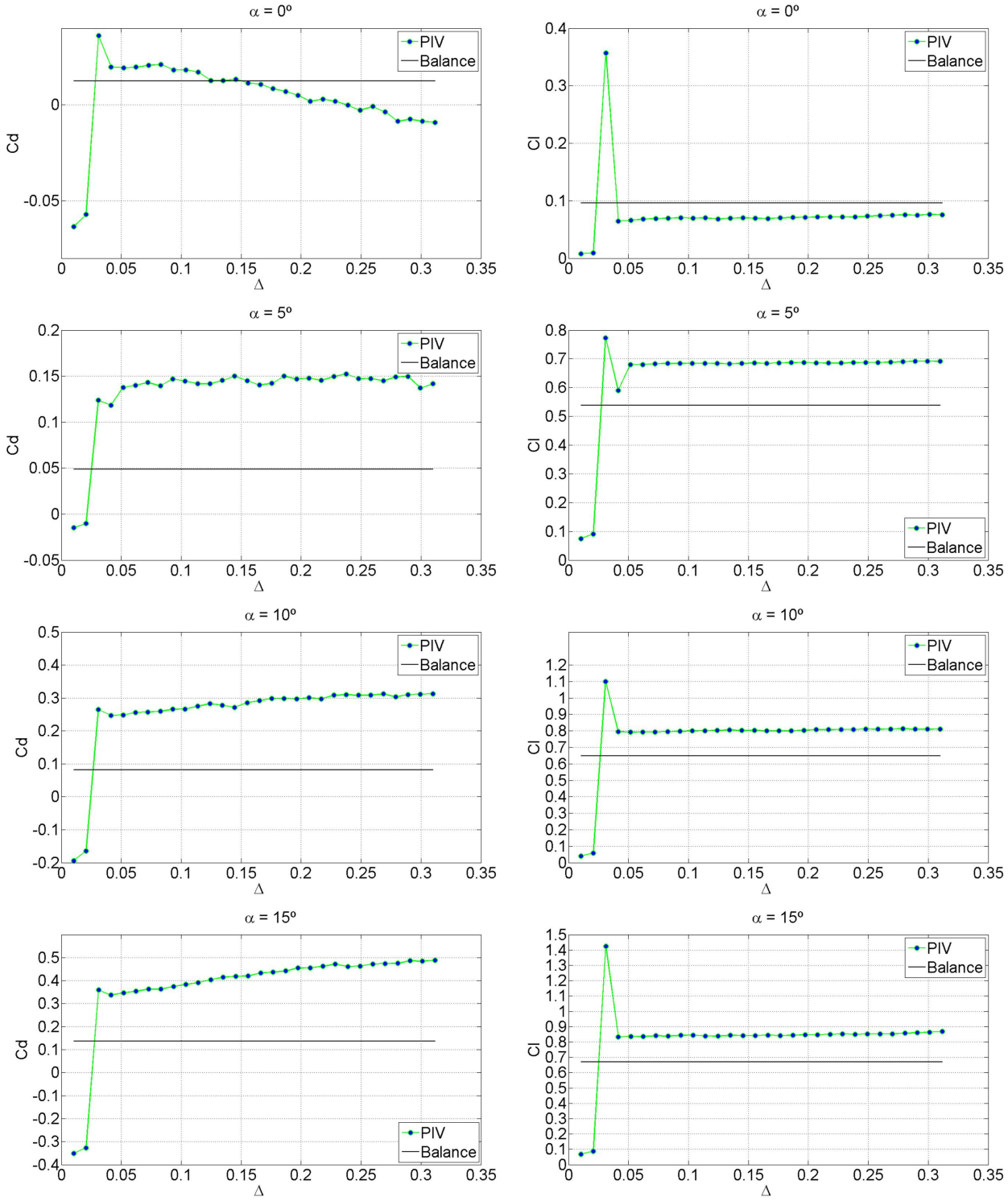

Figure 4.9: Variation of the flat plate force coefficients with the integration path (Re = 30,000).

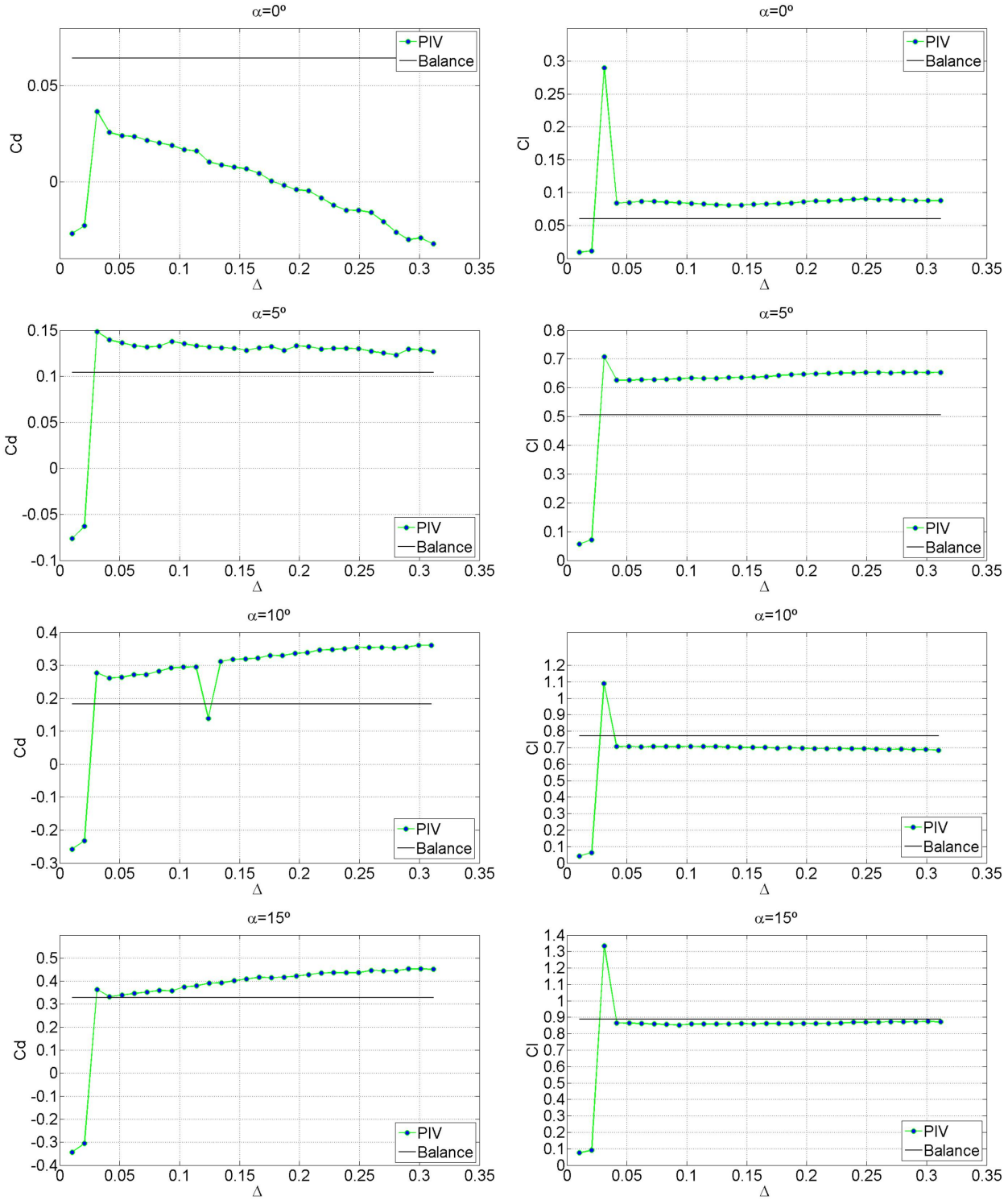

Figure 4.10: Variation of the flat plate force coefficients with the integration path (Re = 70,000).

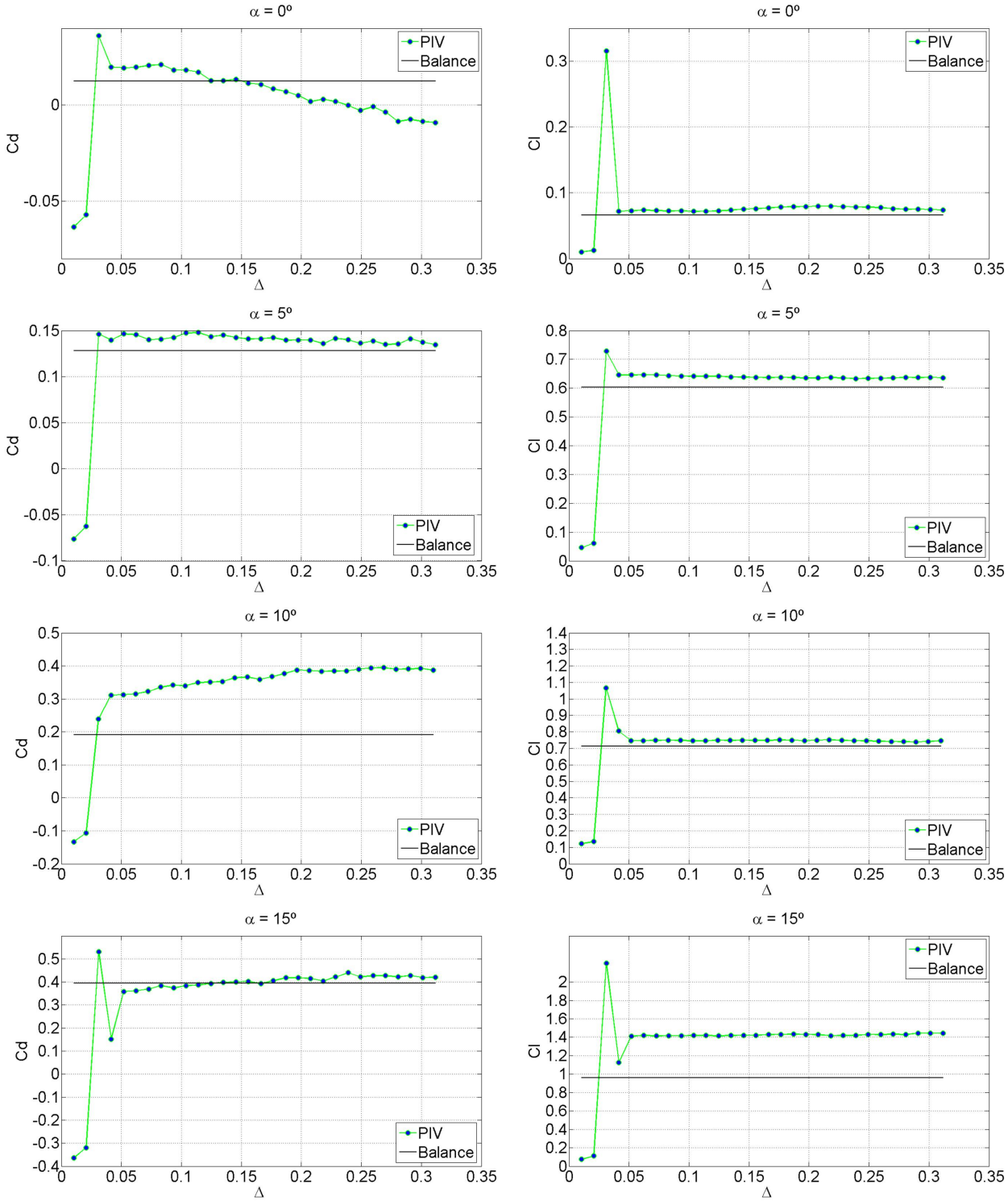

Figure 4.11: Variation of the flat plate force coefficients with the integration path (Re = 120,000).

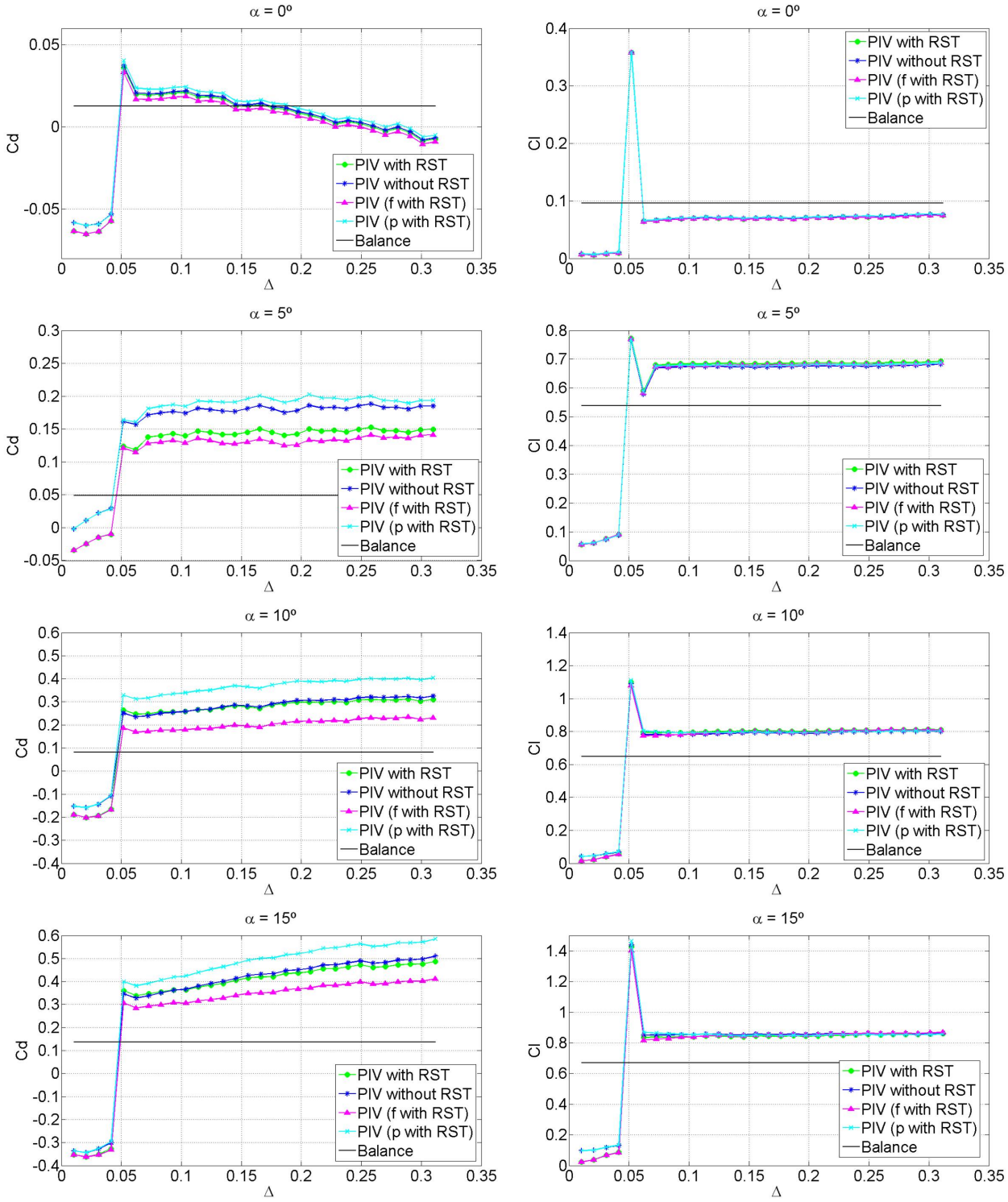

Figure 4.12: Influence of the Reynolds stress terms in the 2D load calculation (Re = 30,000).

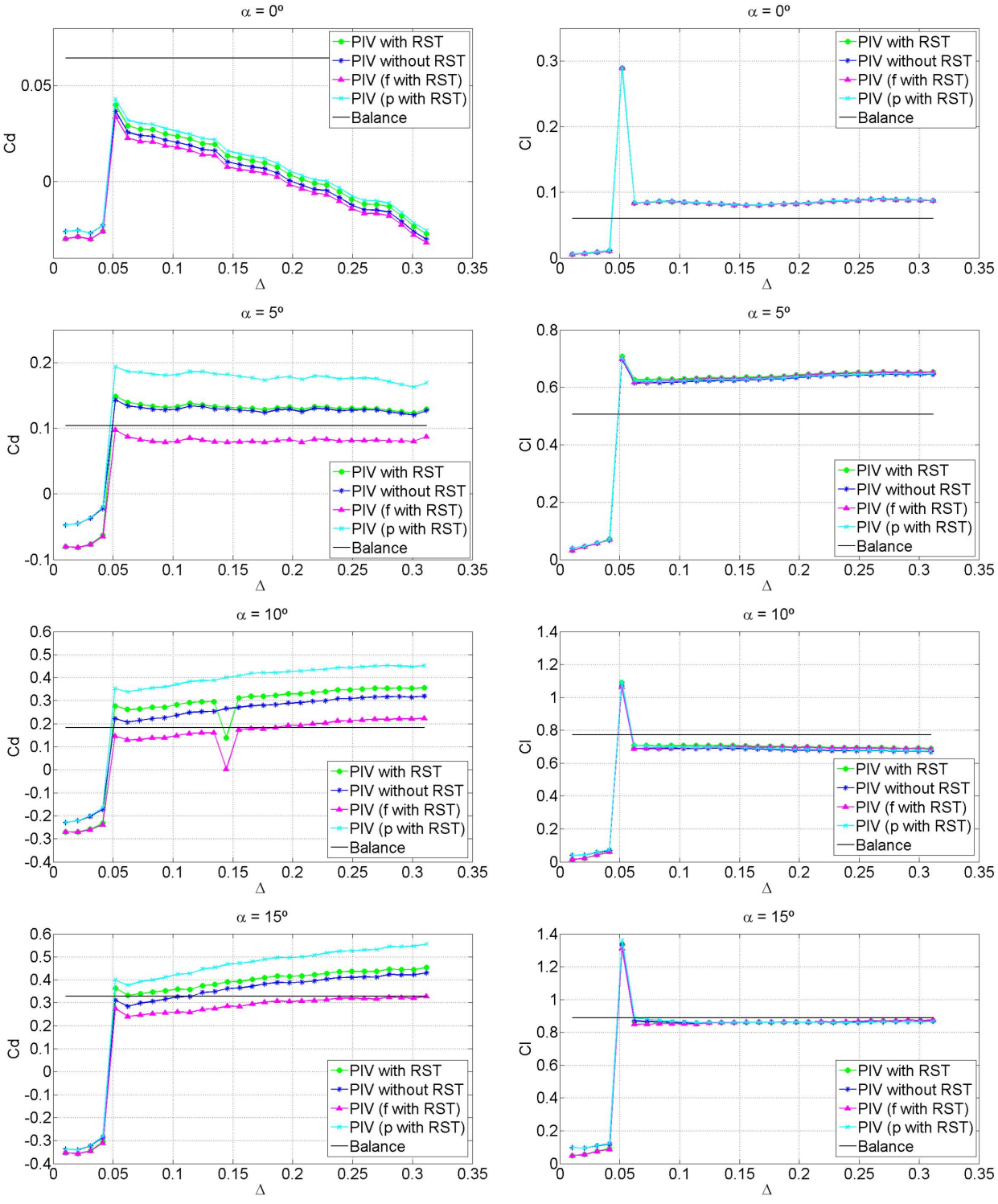

Figure 4.13: Influence of the Reynolds stress terms in the 2D load calculation (Re = 70,000).

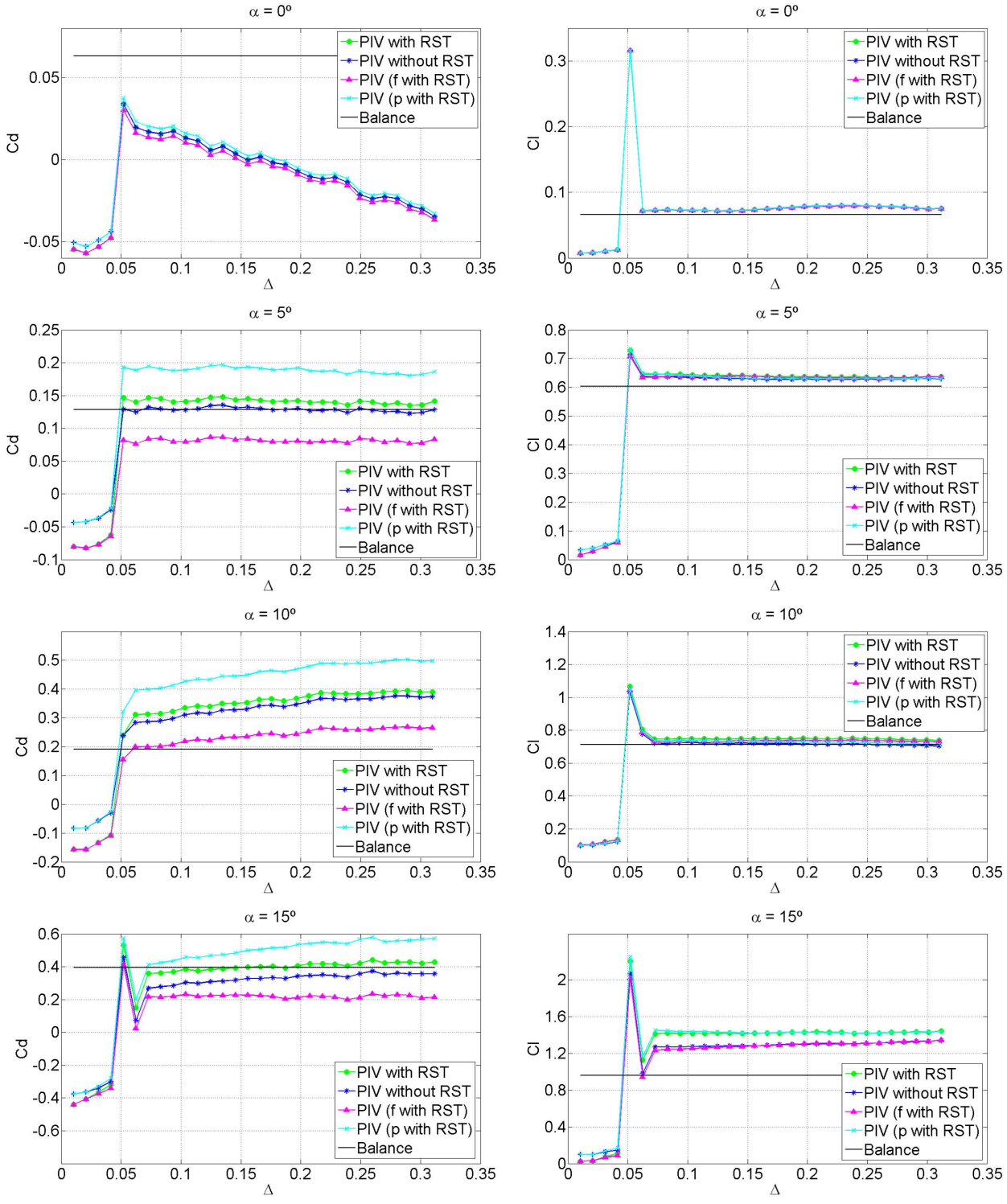

Figure 4.14: Influence of the Reynolds stress terms in the 2D load calculation (Re = 120,000).

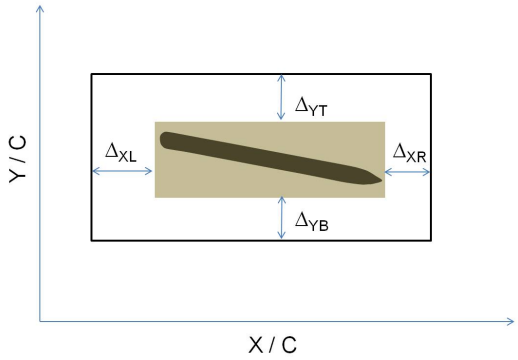

	$\triangle_{XR}$	$\triangle_{XL}$	$\triangle_{YT}$	$\triangle_{YB}$
$\alpha = 0°$	0.156	0.156	0.156	0.156
$\alpha = 5°$	0.156	0.156	0.156	0.156
$\alpha = 10°$	0.207	0.155	0.207	0.155
$\alpha = 15°$	0.208	0.156	0.208	0.156

Figure 4.15: 2D PIV-Loads optimum first integration path.

$\alpha = 15°$, this is evident, since the flow is fully separated from the leading edge. For $\alpha = 5° - 10°$, the wake velocity profile does not become thinner with higher Re, as can be checked in Figure 4.18. According to Schlichting (2000) , the critical transition Re_x for a flat plate with no adverse pressure gradient ($\alpha = 0°$) is regarded to be between the values $\mathrm{Re_x} = [3,5 \cdot 10^5..10^6]$. Since the maximum Reynolds number based on chord studied is Re = 120,000, the boundary layer at $\alpha = 0°$ should be laminar for all Re numbers considered.

4.5 Conclusions

The flow around an inclined flat plate was investigated via 2D-PIV (f =7.5Hz) in a low speed wind tunnel. Simultaneously, aerodynamic forces were measured by means of a high sensitive balance. The main goal was to validate the forces calculated using only velocity data, with the results provided by the balance.

Built in methacrylate, the flat plate had a round leading edge, 0.075 relative thickness, and a wedge form in the trailing edge. Measurements were carried out for Re = 30,000, Re = 70,000 and Re = 120,000 and angles of attack ranging between $\alpha = 0°$ and $\alpha = 15°$. The low speed wind tunnel had a closed test chamber of $135 \times 160\mathrm{mm}^2$ and the balance was connected to the airfoil by an external structure made of aluminum. The balance results were validated with experimental results available in the literature, finding good agreement. However, for lower forces, the dispersion of the data was bigger.

Using only velocity data and its derivatives, the lift and drag force (per unit length) was calculated, using a Momentum based contour approach. A Poisson solver was used to determine the pressure field. It was a two dimensional, steady, aerodynamic problem in which Reynolds stress terms were considered to account for the turbulence present in the wake.

Load calculation found good agreement with balance results. It has been concluded that disagreements encountered between PIV-Loads and Balance results are due to:

- Balance uncertainties: structure vibrations and 3D effects in the test chamber.
- PIV uncertainties: lack of resolution, velocity gradients inside the interrogation window chosen, laser reflections.

From these, PIV sources of error were more important, since it was computing drag where

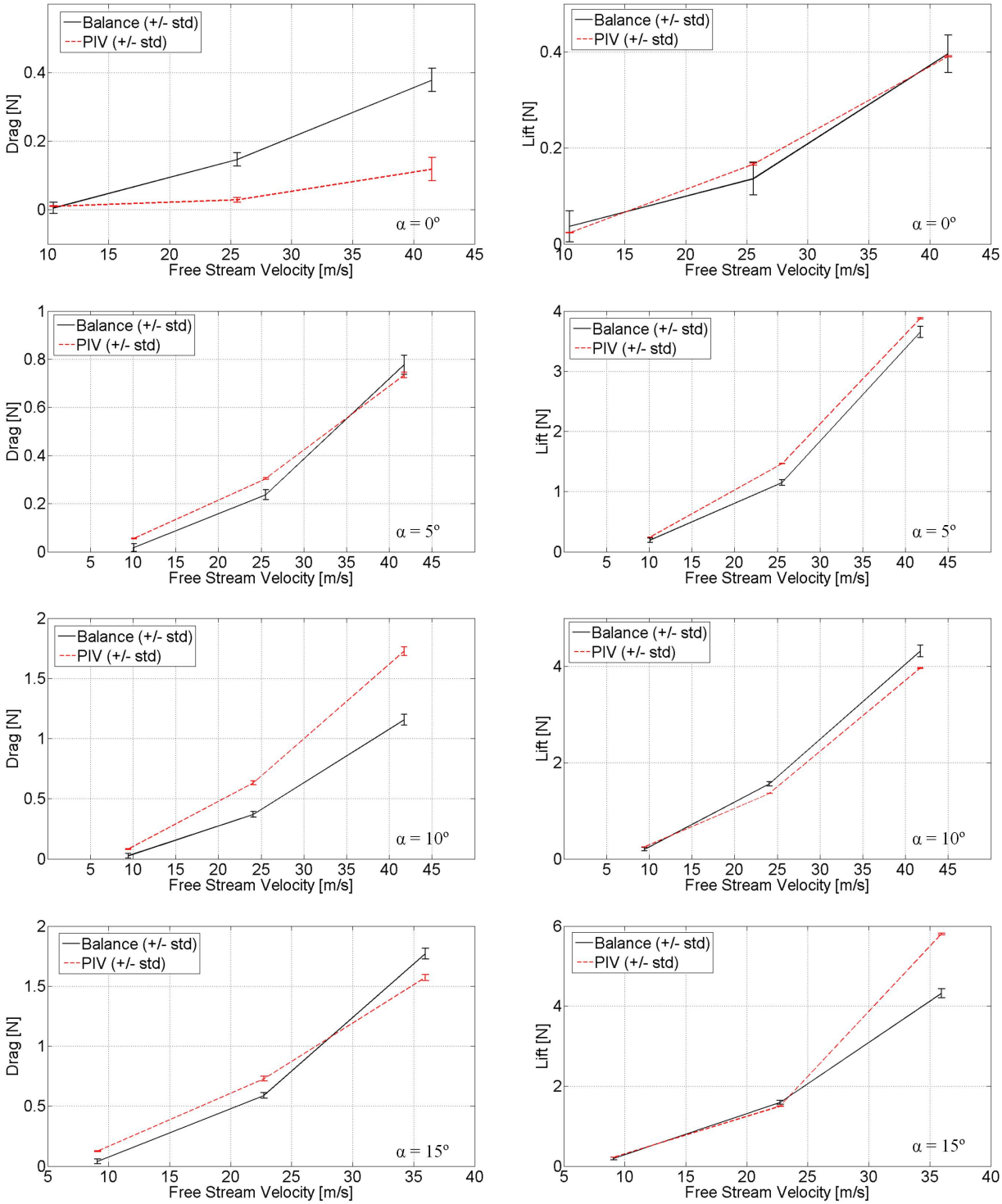

Figure 4.16: Comparison of PIV and balance force measurements (2D PIV-Loads).

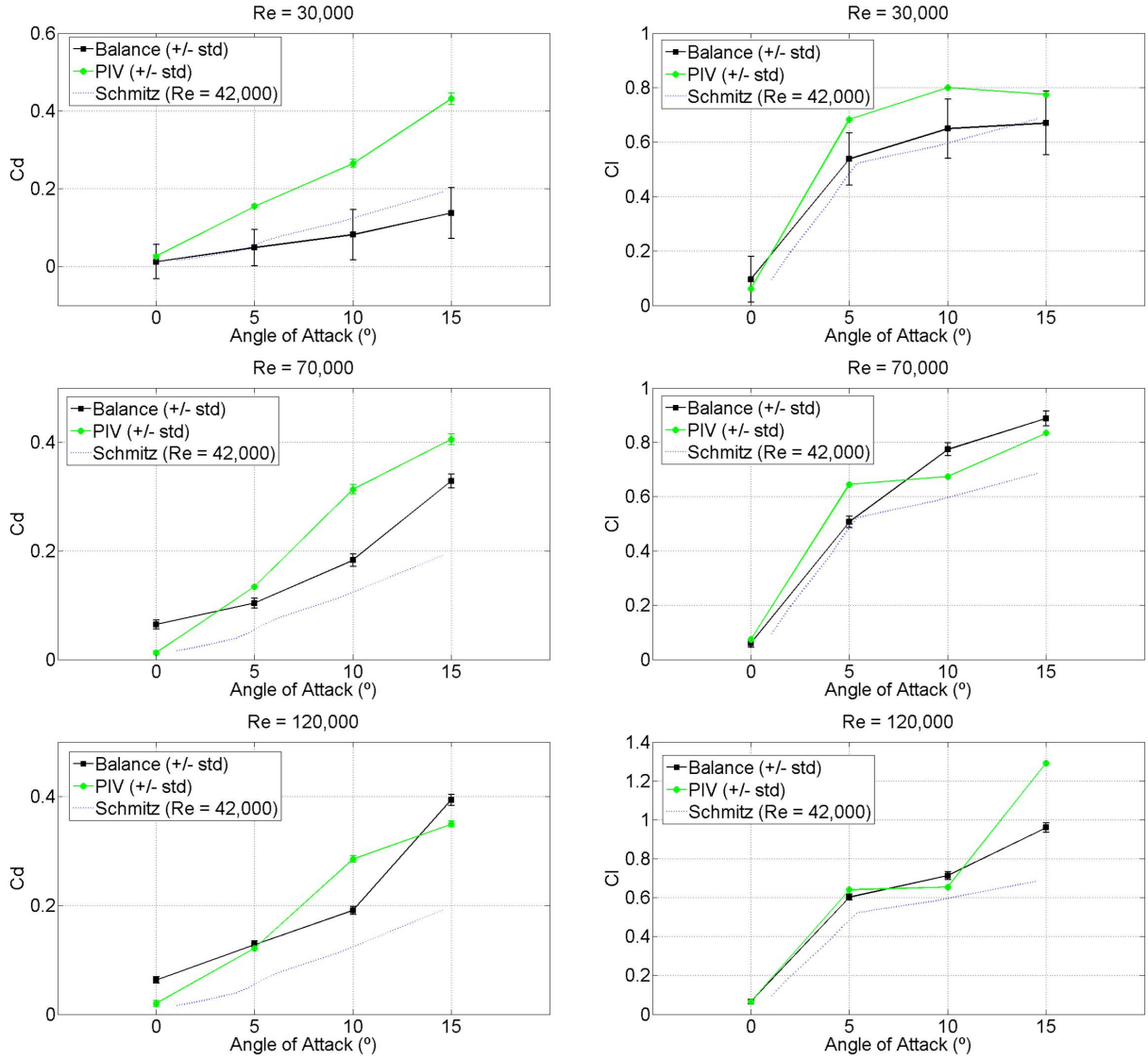

Figure 4.17: Comparison of PIV and balance force coefficients (2D PIV-Loads).

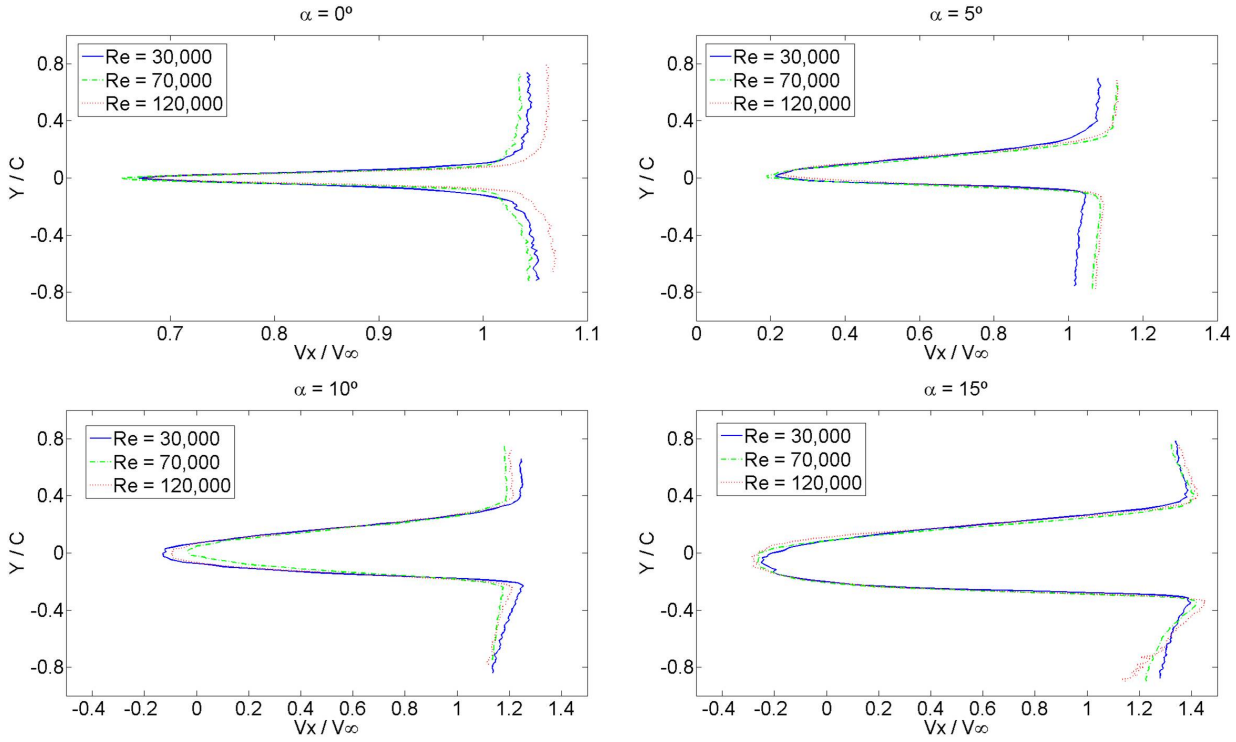

Figure 4.18: Flat plate wake profile for different Reynolds numbers.

bigger differences were encountered; specially when dealing with higher angles of attack. Theses cases are directly connected with a bigger turbulent wake, where velocity gradients are higher and not completely captured by the available PIV system.

For the three Re conditions studied, the velocity wake profile coincided in all cases, indicating there is no boundary layer transition reached when increasing the flow velocity. Lift and drag coefficients increase with the angle of attack and this rise is higher for bigger Re.

Finally, the study provided with means for characterizing the stalling conditions of the flat plate and its vorticity shedding, at different Re and angles of attack. The results were contrasted with DNS data, RANS data and existing literature experimental data. The flat plate flow disattachement starts near the trailing edge and expands towards the leading edge when increasing the angle of attack. For $\alpha = 15°$ the flow is fully disattached, but there is still suction and therefore lift, although drag has also increased. For fully separated flow, vortices start to come off the leading edge with a frequency of f = 350Hz.

Chapter 5

3D Load Calculation on a Wind Turbine Blade

5.1 Introduction

Aerodynamic loading control is a main topic of interest by the wind energy community nowadays (Van Kuik *et al.* (2006)). In this sense, the present study aims at providing with a new method for measuring the loads impinged on the blade of a Horizontal Axis Wind Turbine (HAWT) by means of a non intrusive technique obtaining, simultaneously, the pressure and velocity fields around it.

Conventionally, wind turbine blade loads have been measured with pressure taps and Pitot-tube wake rakes. As an example, results obtained using these methods might be found in the NREL UAE phase VI and the MEXICO project. Although these techniques have proven to be reliable for a static model, they presented some implementation difficulties when applied to a rotating blade (see Schreck *et al.* (2010)). Besides, apart from only providing information at discrete points, wake rakes introduce flow perturbations and pressure taps require the modification of the model. This last issue becomes an important drawback when testing a highly scaled down wind turbine model; in these cases, the installation of pressure taps inside the blades is almost impracticable. Another way of measuring forces is the use of multi-component balances. However, they offer limited information since only global forces and/or moments on the HAWT can be attained, without providing with local information on the blade itself.

In recent years, there have been several studies that proved the feasibility of calculating aerodynamic loads using only velocity fields and their derivatives; Noca *et al.* (1999), Kurtulus *et al.* (2007), van Oudheusden *et al.* (2007) and Ragni *et al.* (2011), among others. A brief summary of the state of the art of this methodology can be found in Section 1.2.

The present work calculates the forces exerted on the rotating blade of a HAWT of 2m diameter operating at its optimal condition in axial and yawed flow. Firstly, the flow around the blade was examined by means of Stereoscopic Particle Image Velocimetry (SPIV), at a given azimuthal position. The SPIV equipment was mounted on a traverse system that enabled the scanning of the blade from the root to the tip. Next, the whole pressure field was reconstructed integrating the Momentum Equation by a second order Poisson

algorithm, thus avoiding the path dependency associated with the spatial marching procedures. Finally, axial and tangential forces were determined all along the blade with a 3D formulation using the experimental velocity data obtained and the calculated pressure distribution. As means of reference and discussion, the attained results were compared with the velocity fields and loads produced with a 3D Panel Method model and a BEM model.

The experimental campaign was performed at the Open Jet Facility (OJF) of TU-Delft (The Netherlands). The main challenge was to measure forces in a rotating blade with a 3D formulation, both in steady and unsteady flow conditions (axial and yawed flow, respectively).

5.2 Experimental Apparatus and Procedure.

5.2.1 Wind Tunnel, HAWT Model and Operating Regimes.

The Open Jet Facility (OJF) is a closed circuit wind tunnel; it has an octagonal jet exit of 2.85m equivalent diameter and its test section size is 6m $\times$ 6.5m $\times$ 13.5m. During all measurements, the flow velocity in the test chamber was fixed at 6m/s.

Regarding the upwind HAWT model tested, it was composed of 2 blades and had a total radius of $R = 1$m (the hub radius was $R_h = 0.147$m). It was operated by and electrical engine at a constant angular velocity of 400rpm, which made the turbine run at tip speed ratio TSR = 7. Considering axial flow, the Reynolds number and the relative Mach number at the tip were, respectively, Re = $275,000$ and M = 0.12. The airfoil section used all along the blade (except at the connection with the hub) was a DU-96-W180. The blade was not pitched but it was tapered and twisted, with a maximum chord length of 0.123m at the radial position $r/R = 0.29$ and a maximum twist of $\theta = -15°$ at the root ($r/R = 0.16$).

A brief summary of the experimental conditions is presented in Table 5.1, and Figure 5.1 shows the blade twist and chord distribution characterizing the blade.

Turbine Geometry	
Rotor radius	1 m
Hub radius	0.147m
Number of blades	2
Pitch	0°
Blade max. chord	0.123 m
Airfoil geometry	DU-96-W180
Twist (at the root)	$-15°$

Operating Conditions	
Flow velocity	6 m/s
Angular velocity	400 rpm
Re (at the tip)	2.75e+05
M (at the tip)	0.12
Tip speed ratio	7
Atm. pressure	1010.5 hPa
Yaw angle	30^{o}

Table 5.1: 3D PIV-Loads experimental conditions.

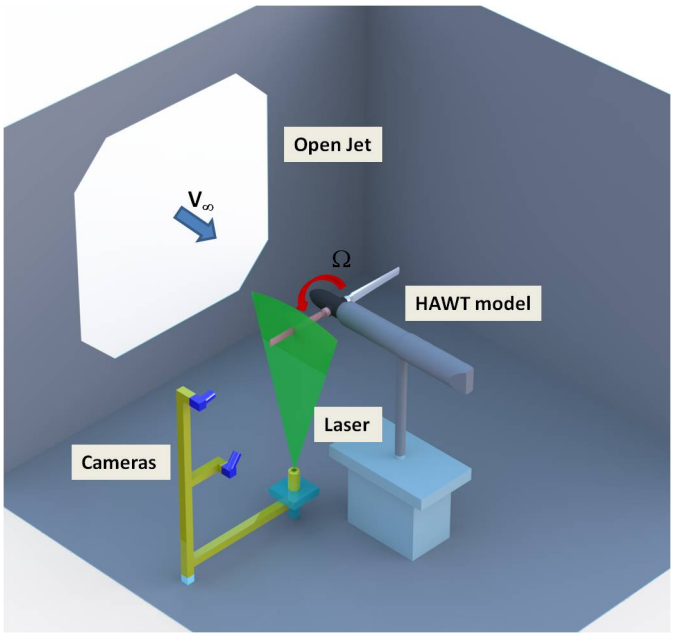

Figure 5.2: Scheme of the 3D PIV-Loads experimental set up.

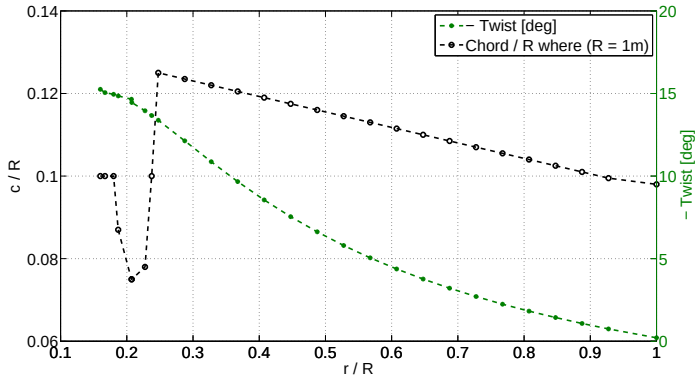

Figure 5.1: Twist and chord distribution along the HAWT blade.

5.2.2 Stereoscopic PIV Measurements

With the aim to explore the flow surrounding the blade, SPIV planes were acquired perpendicularly to the axis of the blade, distributed from the root to the tip. The planes were more compactly laid out near the tip, in the last 10% of the blade, where the loading gradient is steeper and the radial flow is bigger due to the tip vortex. A sketch of the experimental set up can be seen in Figure 5.2.

When doing SPIV, shadows and reflections are always an important issue: in this case, the blade itself shaded some part of the SPIV image. To be able to encompass a closed contour around the blade, two sets of measurements were performed; one set imaging the pressure side of the blade and another set imaging the suction side. Figures 5.5 and 5.8

show the cameras disposition for axial and yaw flow, respectively. After post-processing, these two sets were combined to have full view of the blade cross-section velocity field. This procedure was performed at each radial position measured and regions with laser reflections were masked out in order to avoid unreliable data. Figure 5.3 includes some photographs showing various aspects of the experimental setup.

The illumination was provided by a double pulsed Nd:YAG laser with a maximum energy of 200mJ per pulse. Laser optics formed a 3mm thickness light sheet. In addition, a SAFEX generator seeded smoke particles of diethylene glycol and water with a median diameter of 1μm .The fog was introduced directly downstream of the wind tunnel test section and mixed uniformly during the recirculation. Main illumination and seeding characteristics are shown in Table 5.2.

Illumination		**Seeding**	
Laser type	Double pulsed Nd:YAG	Fluid composition	Diethylene glycol and water
Energy per pulse	200 mJ	Fog generator	SAFEX
Sheet thickness	3mm	Particle diameter	1μm (median)

Table 5.2: 3D PIV-Loads illumination and seeding characteristics.

In order to obtain phase-locked images, both laser and cameras were triggered at the same chosen azimuthal position of the blade. This was achieved by means of an angular position encoder, embedded inside the hub, that allowed the phase synchronization of the PIV measurements with the blade position. The two Imager Pro LX cameras (16 Mpx resolution) were equipped with Nikon objectives of 180mm focal length and a diaphragm aperture of $f^{\#}$=5.6. With the purpose of reducing the reflections of the laser ($\lambda = 532$nm), the blade was painted with rodhamine, which reflects in red, and a green filter was adapted to each of the camera objectives.

The SPIV images were acquired and processed using LaVision Davis 7.2 software and they were corrected for residual misalignment through self calibration. The time separation between images was 100μs (each particle would move around 10px from frame A to frame B, the image resolution being 18 px/mm) and the field of view observed by the cameras was FOV $\approx$ 250mm $\times$ 170mm. During processing, the dewarped images were evaluated with an iterative multigrid from a window size of 128px $\times$ 128px down to a window size of 32px $\times$ 32px and 50% overlap (see Scarano *et al.* (2000)), which rendered an spatial resolution (see Nogueira *et al.* (2005)) of 1.78mm, that is, 1.4% of the maximum chord. Once the pressure side and suction side were combined to form the final image, the FOV was consequently enlarged up to FOV $\approx$ 250mm $\times$ 220mm.

With the aim of reducing the uncertainties from recalibration of the rearranged setup, both cameras and laser were mounted in a traverse system so that they moved together each time a different span position was considered. A brief summary of the imaging and acquisition parameters is shown in Table 5.3.

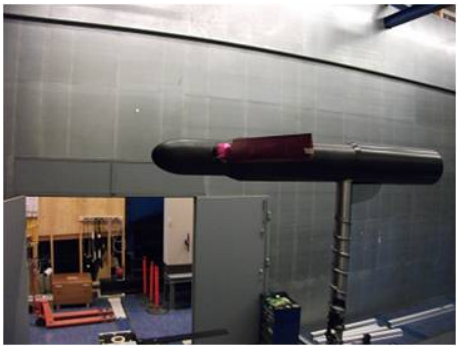

a) HAWT blade at 90°azimuth.

b) HAWT model at the OJF.

c) Pressure side configuration.

d) Suction side configuration.

Figure 5.3: Details on the 3D PIV-Loads experimental set up.

Imaging	
Camera	2 Imager Pro LX
Resolution	4830 × 3230 px
Focal length	180 mm
Diaph. aperture	5.6
Field Of View	250mm × 220mm
Shift (in $\triangle t$)	$\triangle$px =10px

Acquisition	
Recordings	100 image pairs
Pulse separation	$\triangle t$=100μs
Int. window	128×128 ⇒ 32×32
Overlap	50%
Image resolution	18 px/mm
Spatial resolution	1.78mm

Table 5.3: 3D PIV-Loads imaging and acquisition parameters.

5.2.3 Computational models

In order to compare the results attained experimentally a computational panel method model was used to simulate the HAWT working in the same conditions. It provided velocity fields all along the blade within the same study regions, as well as axial and tangential loads exerted in every section of it.

The panel method model utilized was developed by Dixon [11] following the formulation presented by Katz and Plotkin [25] and validated by Simão Ferreira [49]. It is a 3D model that assumes potential flow and can solve multibody, unsteady problems. The blades are

modeled with 3D surface panels of sources and doublets with a constant distribution (the non-entry requirement on the airfoil surface is implemented by imposing a Dirichlet boundary condition on the potential function). As the blades rotate, a wake of free convecting doublets is released from the trailing edge. By imposing the Kutta condition the vorticity at the trailing edge is set to zero. Therefore, the near wake doublet strength is given by the difference in doublet strengths between upper and lower surfaces of the airfoil. Finally, the far wake is modeled with a mesh of vortex rings. The model contains methods to realistically treat blade-wake interactions and vortex stretching and contraction.

In addition, a BEM model was used to have a second reference in the load calculation results. The model used was developed following the formulation presented by Hansen [20] and Burton *et al.* [8]. It combines the conservation of Momentum across the rotor and the integration of aerodynamic forces over the blade elements. To achieve closure, the thrust calculated from the Momentum Equation is equated with that calculated with the blade element equations; in this way, the induced velocities across the rotor can be calculated. Once the inflow conditions for each blade element have been determined, aerodynamic forces are computed using lift and drag coefficients from existing experimental airfoil data.

5.3 Load Calculation Procedure

5.3.1 Axial Flow Condition

Aerodynamic forces exerted on a wind turbine blade element immersed in an air current originate by the surface pressure distribution and the viscous shear stresses. Due to the difficulty of measuring these quantities on the model surface, the aerodynamic lift and drag forces can be retrieved from the change in Momentum of the flow inside a finite control volume (surrounding the airfoil) that has no other external forces apart from those caused by the blade element itself, as described in Section 3.3.1. The finite control volume is chosen with a rectangular shape ($aghi$) for simplicity: it has two cuts ($bc - ef$) that connect with the internal shape of the control volume, which is wrapping the airfoil (edc), as shown in Figure 3.5. The force impinged by the airfoil on the flow causes a change in Momentum inside the control volume and can therefore be assessed with Equation 5.1, (see Anderson [5]). The maximum free stream velocity encountered (at the tip of the blade) is M_{tip}=0.12 and the flow is considered incompressible.

$$\begin{aligned}\overrightarrow{F}_{flow \Longrightarrow airfoil} = & -\frac{\mathrm{d}}{\mathrm{d}t}\iiint_{\upsilon}\rho\overrightarrow{V}_r \mathrm{d}\upsilon - \iint_{s_{aghi}} p\,\overrightarrow{n}\,\mathrm{d}s + \iint_{s_{aghi}} \overline{\overline{\tau'}}\,\overrightarrow{n}\,\mathrm{d}s - \iint_{s_{aghi}} \rho(\overrightarrow{V}_r \cdot \overrightarrow{n})\overrightarrow{V}_r \mathrm{d}s \\ & - \iiint_{\upsilon} 2\rho(\overrightarrow{\Omega} \times \overrightarrow{V}_r)\mathrm{d}\upsilon - \iiint_{\upsilon}\rho(\overrightarrow{\Omega} \times (\overrightarrow{\Omega} \times \overrightarrow{r}))\mathrm{d}\upsilon \end{aligned} \tag{5.1}$$

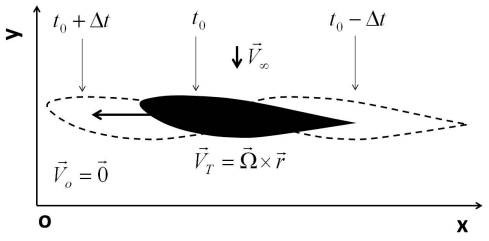

a.1) Stationary frame of reference

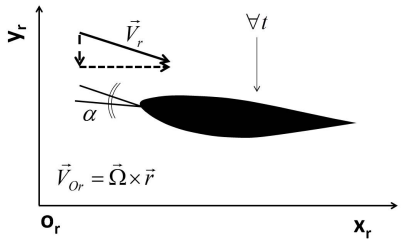

b.1) Moving frame of reference

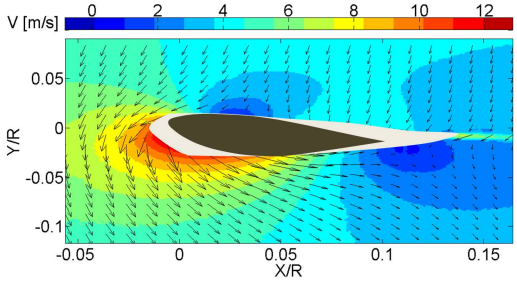

a.2) Absolute velocities (z/R =0.61)

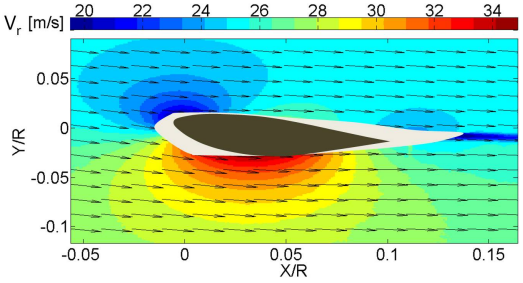

b.2) Relative velocities (z/R =0.61)

Figure 5.4: Possible frames of reference: a.1) stationary and b.1) rotating (with an example of their corresponding velocity fields a.2 and b.2).

$$
\begin{bmatrix} F_x \\ F_y \end{bmatrix} = \overbrace{\int_{aghi} \mu \begin{bmatrix} 2\frac{\partial u}{\partial x} & \left(\frac{\partial u}{\partial y}+\frac{\partial v}{\partial x}\right) \\ \left(\frac{\partial u}{\partial y}+\frac{\partial v}{\partial x}\right) & 2\frac{\partial v}{\partial y} \end{bmatrix} \vec{n}\,\mathrm{d}s - \frac{\mathrm{d}}{\mathrm{d}z}\iint_s \mu \begin{bmatrix} \left(\frac{\partial u}{\partial z}+\frac{\partial w}{\partial x}\right) \\ \left(\frac{\partial v}{\partial z}+\frac{\partial w}{\partial y}\right) \end{bmatrix} \mathrm{d}x\mathrm{d}y}^{Viscous\ force}
$$

$$
\overbrace{-\int_{aghi} \rho \begin{bmatrix} uu & uv \\ uv & vv \end{bmatrix} \vec{n}\,\mathrm{d}s - \frac{\mathrm{d}}{\mathrm{d}z}\iint_s \rho \begin{bmatrix} uw \\ vw \end{bmatrix} \mathrm{d}x\mathrm{d}y}^{Convective\ acceleration}
$$

$$
\overbrace{-\int_{aghi} \rho \begin{bmatrix} \overline{u'u'} & \overline{u'v'} \\ \overline{u'v'} & \overline{v'v'} \end{bmatrix} \vec{n}\,\mathrm{d}s - \frac{\mathrm{d}}{\mathrm{d}z}\iint_s \rho \begin{bmatrix} \overline{u'w'} \\ \overline{v'w'} \end{bmatrix} \mathrm{d}x\mathrm{d}y}^{Reynolds\ force}
$$

$$
\overbrace{-2\iint_s \rho \begin{bmatrix} -\Omega w \\ 0 \end{bmatrix} \mathrm{d}x\mathrm{d}y}^{Coriolis\ force} \overbrace{-\int_{aghi} \begin{bmatrix} p & 0 \\ 0 & p \end{bmatrix} \vec{n}\,ds}^{Pressure\ force} \tag{5.2}
$$

Figure 5.4 shows the two possible frames of reference with their respective velocity fields. In this case, a moving frame of reference placed on the rotating blade itself was chosen for the formulation. Thus, the time derivative in Equation 3.5 goes to zero because the flow is always the same in the moving frame, which is a cause of the azimuthal symmetry of the flow in the turbine. Since the frame of reference was non-inertial, Coriolis and centrifugal forces had to be taken into account, although the contribution of the latter to the normal and tangential forces was null. Due to the fluctuations from the mean values in the phase-locked velocity fields (see Section 5.4.2), Reynolds stresses were also taken into account. Since the frame of reference was rotating with the turbine, all velocities considered in Equation 3.5 were relative to the blade.

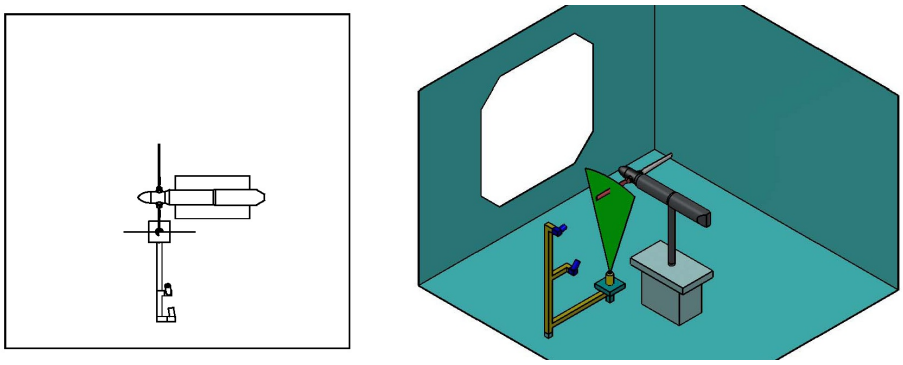

a) Suction side configuration.

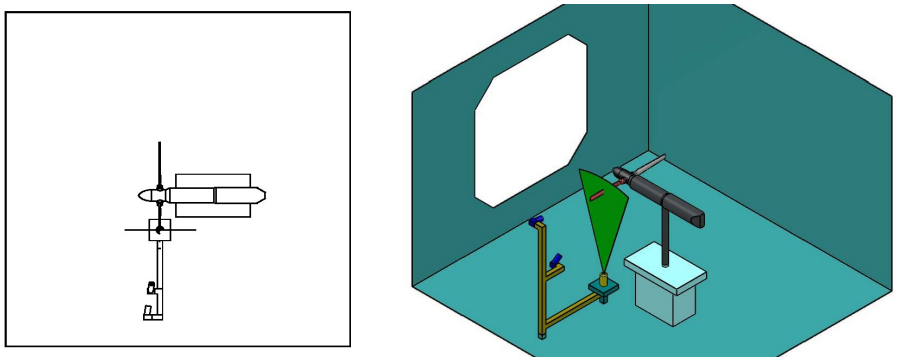

b) Pressure side configuration.

Figure 5.5: 3D PIV-Loads set up: Axial flow conditions.

The final Momentum Equation formulation used is described in Equation 5.2, which explicitly describes Equation 3.5 for the case of study. The forces were calculated per span unit length in each section of the blade, using the three-dimensional information of the flow. For each plane, the information of both the previous and next sectional planes (placed at a distance $\triangle z/2$) was used to form a control volume with the shape of a slice, whose width was $\triangle z$ (where $\triangle z \lll \triangle x, \triangle y$), as depicted in Figure 5.6. The terms that include a derivative with z in Equation 5.2 are used to calculate the out-of-plane variations of the velocity fields.

The integral Momentum Equation used (see Equation 5.1) requires the velocity and the pressure fields to calculate the aerodynamic forces on the airfoil. Hence, it is necessary

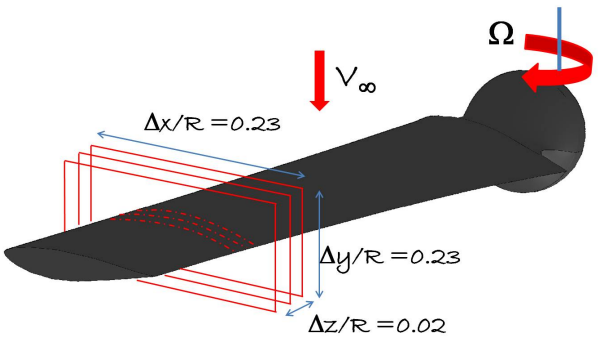

Figure 5.6: 3D Control volume formed by 3 consecutive SPIV planes.

to compute the pressure inside the control volume. The pressure gradient is derived from the Momentum Equation in its differential form, using the relative velocity field and its derivatives (see White *et al.* [61]), considering inertial forces, Reynolds stresses and incompressible flow, as expressed in Equation 5.4.

$$\nabla p = -\frac{\mathrm{d}}{\mathrm{d}t}\left(\rho\overrightarrow{V_r}\right) - \rho\overrightarrow{V_r}\cdot\nabla\overrightarrow{V_r} + 2\rho(\overrightarrow{\Omega}\times\overrightarrow{V_r}) + \rho(\overrightarrow{\Omega}\times(\overrightarrow{\Omega}\times\overrightarrow{r}) + \mu\triangle\overrightarrow{V_r} \tag{5.3}$$

$$\begin{aligned}\begin{bmatrix}\frac{\partial p}{\partial x}\\ \frac{\partial p}{\partial y}\end{bmatrix} &= -\rho\begin{bmatrix}u\frac{\partial u}{\partial x}+v\frac{\partial u}{\partial y}+w\frac{\partial u}{\partial z}\\ u\frac{\partial v}{\partial x}+v\frac{\partial v}{\partial y}+w\frac{\partial v}{\partial z}\end{bmatrix} - \rho\begin{bmatrix}\frac{\partial\overline{u'u'}}{\partial x}+\frac{\partial\overline{u'v'}}{\partial y}+\frac{\partial\overline{u'w'}}{\partial z}\\ \frac{\partial\overline{u'v'}}{\partial x}+\frac{\partial\overline{v'v'}}{\partial y}+\frac{\partial\overline{v'w'}}{\partial z}\end{bmatrix}\\ &\quad -2\rho\begin{bmatrix}\Omega w\\ 0\end{bmatrix} + \mu\begin{bmatrix}\frac{\partial^2 u}{\partial x^2}+\frac{\partial^2 u}{\partial y^2}+\frac{\partial^2 u}{\partial z^2}\\ \frac{\partial^2 v}{\partial x^2}+\frac{\partial^2 v}{\partial y^2}+\frac{\partial^2 v}{\partial z^2}\end{bmatrix}\end{aligned} \tag{5.4}$$

Once the pressure gradient has been assessed in the control volume, there are different approaches to calculate the pressure in every point of the field. Historically, several authors (see Liu *et al.* [32] and Kurtulus *et al.* [27]) have addressed this topic by implementing a space-marching algorithm that starts on the boundary conditions, and marches towards the interior of the field, calculating pressures from the spatial derivatives. The main disadvantage of this method is that the error accumulates and propagates with the marching procedure [10].

In the present approach, the pressure was obtained solving the Poisson pressure equation (see Ragni *et al.* [42]), as expressed in Equation 5.5, using a forcing function $g(u,v)$ which was derived from the Momentum Equation, as shown in the Equation 5.6. The discretization of the Laplace operator was done using finite differences, which provides a matrix $\mathbf{D}$ containing information about the flow discretization.

$$\nabla^2 p \approx \mathbf{D}p = g(u,v) \Rightarrow p = \mathbf{D}^{-1}g(u,v) \tag{5.5}$$

$$\left\{\begin{array}{ll}\left[\frac{p_{i+1,j}-2p_{i,j}+p_{i-1,j}}{\triangle x^2}+\frac{p_{i,j+1}-2p_{i,j}+p_{i,j-1}}{\triangle y^2}\right] & i=1...n \\ & j=1...m \end{array} = \mathbf{D}p \right\}$$
$$\left\{\frac{\left[\frac{\partial p}{\partial x}\right]_{i+1,j}-\left[\frac{\partial p}{\partial x}\right]_{i-1,j}}{2\triangle x}+\frac{\left[\frac{\partial p}{\partial y}\right]_{i,j+1}-\left[\frac{\partial p}{\partial y}\right]_{i,j-1}}{2\triangle y} = g(u,v)_{i,j}\right\} \tag{5.6}$$

Finally, a Neumann condition was used on the airfoil surface, imposing $\frac{\partial p}{\partial n}$ (calculated with the Momentum Equation, as expressed in Equation 5.4), where $\overrightarrow{n}$ is the direction perpendicular to the airfoil surface. On the outer control, in the regions where the flow can be considered irrotational, a Dirichlet condition was used, calculating pressure with the Bernoulli theorem (see Equations 5.7 and 5.8). In the wake region a Neumann condition was imposed again, using the pressure gradient ($\frac{\partial p}{\partial x}$) resulting from the Momentum Equation (see Equation 5.4).

$$p_t = p_\infty + \frac{1}{2}\rho\left(V_\infty^2 + (\Omega r)^2\right) \tag{5.7}$$

$$p = p_t - \frac{1}{2}\rho(u^2+v^2+w^2) \tag{5.8}$$

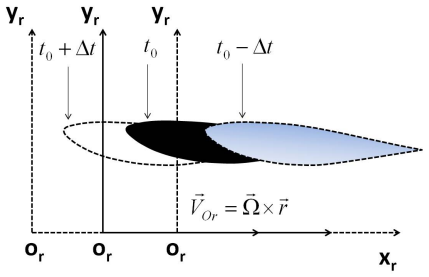

Figure 5.7: Moving frame of reference: three different time instants.

5.3.2 Yawed Flow Condition

In order to calculate loads in the yaw condition, there are two options: one is to consider a moving frame of reference mounted on the rotating blade, as we did for axial flow. The other one is to use a stationary frame of reference. In both cases non steady cases will have to be taken into account, because for the yawed flow condition, there is no azimuthal symmetry in the flow around the blade. Therefore, five planes are needed to compute forces with a 3D formulation: the plane where forces are computed, the two planes that are disposed in the same azimuth but with a different span position (slightly nearer to the tip and slightly nearer to the hub) and two more planes which are in the same span position but with a different azimuth (one instant before, one instant afterward).

5.3.2.1 Moving Frame of Reference

If a moving frame of reference is used, the images corresponding to different times photographed with the cameras at the same position, considering the distance that the blade has moved is so small, that the movement can be evaluated in the same plane (that is, considering the the circular movement has been almost linear). Therefore, when evaluating the velocity fields, the images need to be cropped, so that for each image, (x, y) coordinates correspond to the same relative location towards the airfoil. This is shown in Figure 5.7.

Using a moving frame of reference, forces are calculated with a similar integral ME as in the axial case, just adding the local acceleration term, as expressed in Equation 5.9 and Equation 5.10, where all velocities are relative to the rotating blade.

$$\begin{aligned}\overrightarrow{F}_{flow \Longrightarrow airfoil} = & -\iint_{s_{aghi}} p\overrightarrow{n}\,\mathrm{d}s + \iint_{s_{aghi}} \overline{\overline{\tau'}}\overrightarrow{n}\,\mathrm{d}s - \iint_{s_{aghi}} \rho(\overrightarrow{V_r}\cdot\overrightarrow{n})\overrightarrow{V_r}\mathrm{d}s - \frac{\mathrm{d}}{\mathrm{d}t}\iiint_{\upsilon}\rho\overrightarrow{V_r}\mathrm{d}\upsilon \\ & - \iiint_{\upsilon} 2\rho(\overrightarrow{\Omega}\times\overrightarrow{V_r})\mathrm{d}\upsilon - \iiint_{\upsilon}\rho(\overrightarrow{\Omega}\times(\overrightarrow{\Omega}\times\overrightarrow{r}))\mathrm{d}\upsilon \end{aligned} \quad (5.9)$$

$$\begin{bmatrix} F_x \\ F_y \end{bmatrix} = \overbrace{\int_{aghi} \mu \begin{bmatrix} 2\frac{\partial u}{\partial x} & \left(\frac{\partial u}{\partial y}+\frac{\partial v}{\partial x}\right) \\ \left(\frac{\partial u}{\partial y}+\frac{\partial v}{\partial x}\right) & 2\frac{\partial v}{\partial y} \end{bmatrix} \overrightarrow{n}\,\mathrm{d}s - \frac{\mathrm{d}}{\mathrm{d}z}\iint_s \mu \begin{bmatrix} \left(\frac{\partial u}{\partial z}+\frac{\partial w}{\partial x}\right) \\ \left(\frac{\partial v}{\partial z}+\frac{\partial w}{\partial y}\right) \end{bmatrix} \mathrm{d}x\mathrm{d}y}^{Viscous\ force}$$
$$\overbrace{-\int_{aghi} \rho \begin{bmatrix} uu & uv \\ uv & vv \end{bmatrix} \overrightarrow{n}\,\mathrm{d}s - \frac{\mathrm{d}}{\mathrm{d}z}\iint_s \rho \begin{bmatrix} uw \\ vw \end{bmatrix} \mathrm{d}x\mathrm{d}y}^{Convective\ acceleration} \overbrace{-\frac{\mathrm{d}}{\mathrm{d}t}\iint_s \rho \begin{bmatrix} u \\ v \end{bmatrix} \mathrm{d}x\mathrm{d}y}^{Local\ acceleration}$$
$$\overbrace{-\int_{aghi} \rho \begin{bmatrix} \overline{u'u'} & \overline{u'v'} \\ \overline{u'v'} & \overline{v'v'} \end{bmatrix} \overrightarrow{n}\,\mathrm{d}s - \frac{\mathrm{d}}{\mathrm{d}z}\iint_s \rho \begin{bmatrix} \overline{u'w'} \\ \overline{v'w'} \end{bmatrix} \mathrm{d}x\mathrm{d}y}^{Reynolds\ force}$$
$$\overbrace{-2\iint_s \rho \begin{bmatrix} -\Omega w \\ 0 \end{bmatrix} \mathrm{d}x\mathrm{d}y}^{Coriolis\ force} \overbrace{-\int_{aghi} \begin{bmatrix} p & 0 \\ 0 & p \end{bmatrix} \overrightarrow{n}\,ds}^{Pressure\ force} \tag{5.10}$$

Moreover, to calculate the pressure gradient with moving frame of reference and yawed flow, the problem is similar; non stationary terms need to be added to the ME in its differential form, and, again, all velocities should be relative velocities to the blade. This formulation is presented in Equation 5.11 and Equation 5.12.

$$\nabla p = -\frac{\mathrm{d}}{\mathrm{d}t}\left(\rho\overrightarrow{V_r}\right) - \rho\overrightarrow{V_r}\cdot\nabla\overrightarrow{V_r} + 2\rho(\overrightarrow{\Omega}\times\overrightarrow{V_r}) + \rho(\overrightarrow{\Omega}\times(\overrightarrow{\Omega}\times\overrightarrow{r}) + \mu\triangle\overrightarrow{V_r} \tag{5.11}$$

$$\begin{bmatrix} \frac{\partial p}{\partial x} \\ \frac{\partial p}{\partial y} \end{bmatrix} = -\rho\begin{bmatrix} \frac{\mathrm{d}u}{\mathrm{d}t} \\ \frac{\mathrm{d}v}{\mathrm{d}t} \end{bmatrix} -\rho\begin{bmatrix} u\frac{\partial u}{\partial x}+v\frac{\partial u}{\partial y}+w\frac{\partial u}{\partial z} \\ u\frac{\partial v}{\partial x}+v\frac{\partial v}{\partial y}+w\frac{\partial v}{\partial z} \end{bmatrix} - \rho\begin{bmatrix} \frac{\partial\overline{u'u'}}{\partial x}+\frac{\partial\overline{u'v'}}{\partial y}+\frac{\partial\overline{u'w'}}{\partial z} \\ \frac{\partial\overline{u'v'}}{\partial x}+\frac{\partial\overline{v'v'}}{\partial y}+\frac{\partial\overline{v'w'}}{\partial z} \end{bmatrix}$$
$$-2\rho\begin{bmatrix} \Omega w \\ 0 \end{bmatrix} + \mu\begin{bmatrix} \frac{\partial^2 u}{\partial x^2}+\frac{\partial^2 u}{\partial y^2}+\frac{\partial^2 u}{\partial z^2} \\ \frac{\partial^2 v}{\partial x^2}+\frac{\partial^2 v}{\partial y^2}+\frac{\partial^2 v}{\partial z^2} \end{bmatrix} \tag{5.12}$$

5.3.2.2 Stationary Frame of Reference

Nevertheless, using a moving frame of reference does not entail an advantage in the case of yawed flow, since non-steady terms have to be computed anyway. Therefore, it was decided to try the formulation corresponding to a stationary frame of reference and compare the results obtained. Equations 5.13 and 5.14 define the procedure used; velocities are now absolute velocities.

$$\overrightarrow{F}_{flow\Longrightarrow airfoil} = -\iint_{s_{aghi}} p\,\overrightarrow{n}\,\mathrm{d}s + \iint_{s_{aghi}} \overline{\overline{\tau'}}\,\overrightarrow{n}\,\mathrm{d}s - \iint_{s_{aghi}} \rho(\overrightarrow{V}\cdot\overrightarrow{n})\overrightarrow{V}\,\mathrm{d}s$$
$$-\frac{\mathrm{d}}{\mathrm{d}t}\iiint_{\upsilon}\rho\overrightarrow{V}\,\mathrm{d}\upsilon \tag{5.13}$$

$$\begin{bmatrix} F_x \\ F_y \end{bmatrix} = \overbrace{\int_{aghi} \mu \begin{bmatrix} 2\frac{\partial u}{\partial x} & \left(\frac{\partial u}{\partial y}+\frac{\partial v}{\partial x}\right) \\ \left(\frac{\partial u}{\partial y}+\frac{\partial v}{\partial x}\right) & 2\frac{\partial v}{\partial y} \end{bmatrix} \overrightarrow{n}\mathrm{d}s - \frac{\mathrm{d}}{\mathrm{d}z}\iint_s \mu \begin{bmatrix} \left(\frac{\partial u}{\partial z}+\frac{\partial w}{\partial x}\right) \\ \left(\frac{\partial v}{\partial z}+\frac{\partial w}{\partial y}\right) \end{bmatrix} \mathrm{d}x\mathrm{d}y}^{Viscous\ force}$$
$$\overbrace{-\int_{aghi} \rho \begin{bmatrix} uu & uv \\ uv & vv \end{bmatrix} \overrightarrow{n}\mathrm{d}s - \frac{\mathrm{d}}{\mathrm{d}z}\iint_s \rho \begin{bmatrix} uw \\ vw \end{bmatrix} \mathrm{d}x\mathrm{d}y}^{Convective\ acceleration} \overbrace{-\frac{\mathrm{d}}{\mathrm{d}t}\iint_s \rho \begin{bmatrix} u \\ v \end{bmatrix} \mathrm{d}x\mathrm{d}y}^{Local\ acceleration}$$
$$\overbrace{-\int_{aghi} \rho \begin{bmatrix} \overline{u'u'} & \overline{u'v'} \\ \overline{u'v'} & \overline{v'v'} \end{bmatrix} \overrightarrow{n}\mathrm{d}s - \frac{\mathrm{d}}{\mathrm{d}z}\iint_s \rho \begin{bmatrix} \overline{u'w'} \\ \overline{v'w'} \end{bmatrix} \mathrm{d}x\mathrm{d}y}^{Reynolds\ force}$$
$$\overbrace{-\int_{aghi} \begin{bmatrix} p & 0 \\ 0 & p \end{bmatrix} \overrightarrow{n}ds}^{Pressure\ force} \tag{5.14}$$

Equations 5.15 and 5.16 show the expression used to compute the pressure gradient with a stationary frame of reference. Velocities involved are absolute velocities.

$$\nabla p = -\frac{\mathrm{d}}{\mathrm{d}t}\left(\rho\overrightarrow{V}\right) - \rho\overrightarrow{V}\cdot\nabla\overrightarrow{V} + +\mu\triangle\overrightarrow{V} \tag{5.15}$$

$$\begin{bmatrix} \frac{\partial p}{\partial x} \\ \frac{\partial p}{\partial y} \end{bmatrix} = -\rho \begin{bmatrix} \frac{\mathrm{d}u}{\mathrm{d}t} \\ \frac{\mathrm{d}v}{\mathrm{d}t} \end{bmatrix} - \rho \begin{bmatrix} u\frac{\partial u}{\partial x}+v\frac{\partial u}{\partial y}+w\frac{\partial u}{\partial z} \\ u\frac{\partial v}{\partial x}+v\frac{\partial v}{\partial y}+w\frac{\partial v}{\partial z} \end{bmatrix}$$
$$-\rho \begin{bmatrix} \frac{\partial \overline{u'u'}}{\partial x}+\frac{\partial \overline{u'v'}}{\partial y}+\frac{\partial \overline{u'w'}}{\partial z} \\ \frac{\partial \overline{u'v'}}{\partial x}+\frac{\partial \overline{v'v'}}{\partial y}+\frac{\partial \overline{v'w'}}{\partial z} \end{bmatrix} + \mu \begin{bmatrix} \frac{\partial^2 u}{\partial x^2}+\frac{\partial^2 u}{\partial y^2}+\frac{\partial^2 u}{\partial z^2} \\ \frac{\partial^2 v}{\partial x^2}+\frac{\partial^2 v}{\partial y^2}+\frac{\partial^2 v}{\partial z^2} \end{bmatrix} \tag{5.16}$$

Stationary Frame of Reference and DMT

Regardless of the frame of reference chose, the evaluation of the local acceleration term, as part of the overall aerodynamic loading, requires complete SPIV velocity measurements within the control volume. However, laser reflections near the blade surface, where accelerations are often highest, may lead to large errors in the prediction of the local acceleration term. To avoid the challenge of measuring the velocity field within the control volume, in particular near the model, Wu *et al.* (2005) applied a transformation of the volume integral into a surface integral. This transformation is termed a derivative-moment transformation (DMT). It was found to produce reliable results on a synthetic two dimensional data, in a study carried out by Mohebbian *et al.* (2012). The method is only valid for incompressible flows, and relies on a transformation such as the Gauss theorem. The general form of this theorem is defined in Equation 5.17, where T_{ijk}can be a scalar, vector or a tensor parameter and n_l is a unit normal vector.

$$\iiint_\nu \frac{\partial}{\partial x_l} T_{ijk}\mathrm{d}\nu = \iint_s T_{ijk}n_l\mathrm{d}s \tag{5.17}$$

The DMT method is thus advantageous in that only velocity measurements on the control surfaces are required for the overall estimation of loadings. In vector notation, this transformation provides with a new ME integral expression, as shown in Equation 5.18, where $\overrightarrow{x} = (x, y, z)$ is the position vector measured from any fixed frame of reference.

$$\begin{aligned}\overrightarrow{F}_{flow \Longrightarrow airfoil} &= -\iint_{s_{aghi}} p\overrightarrow{n}\,\mathrm{d}s + \iint_{s_{aghi}} \overline{\overline{\tau'}}\overrightarrow{n}\,\mathrm{d}s - \iint_{s_{aghi}} \rho(\overrightarrow{V}\cdot\overrightarrow{n})\overrightarrow{V}\,\mathrm{d}s \\ &\quad -\frac{\mathrm{d}}{\mathrm{d}t}\iint_{s} \rho\overrightarrow{x}(\overrightarrow{V}\cdot\overrightarrow{n})\mathrm{d}s \end{aligned} \tag{5.18}$$

The same equation applied to our control volume results into Equation 5.19. Since a stationary frame of reference is used, velocities are absolute velocities as provided by the SPIV processing.

$$\begin{aligned}\begin{bmatrix} F_x \\ F_y \end{bmatrix} = &\overbrace{\int_{aghi} \mu \begin{bmatrix} 2\frac{\partial u}{\partial x} & \left(\frac{\partial u}{\partial y}+\frac{\partial v}{\partial x}\right) \\ \left(\frac{\partial u}{\partial y}+\frac{\partial v}{\partial x}\right) & 2\frac{\partial v}{\partial y} \end{bmatrix} \overrightarrow{n}\,\mathrm{d}s - \frac{\mathrm{d}}{\mathrm{d}z}\iint_s \mu \begin{bmatrix} \left(\frac{\partial u}{\partial z}+\frac{\partial w}{\partial x}\right) \\ \left(\frac{\partial v}{\partial z}+\frac{\partial w}{\partial y}\right) \end{bmatrix} \mathrm{d}x\mathrm{d}y}^{Viscous\ force} \\ &\overbrace{-\int_{aghi} \rho \begin{bmatrix} uu & uv \\ uv & vv \end{bmatrix} \overrightarrow{n}\,\mathrm{d}s - \frac{\mathrm{d}}{\mathrm{d}z}\iint_s \rho \begin{bmatrix} uw \\ vw \end{bmatrix} \mathrm{d}x\mathrm{d}y}^{Convective\ acceleration} \overbrace{-\frac{\mathrm{d}}{\mathrm{d}t}\int_{aghi} \rho \begin{bmatrix} xu & xv \\ yu & yv \end{bmatrix} \overrightarrow{n}\,\mathrm{d}s}^{Local\ acceleration} \\ &\overbrace{-\int_{aghi} \rho \begin{bmatrix} \overline{u'u'} & \overline{u'v'} \\ \overline{u'v'} & \overline{v'v'} \end{bmatrix} \overrightarrow{n}\,\mathrm{d}s - \frac{\mathrm{d}}{\mathrm{d}z}\iint_s \rho \begin{bmatrix} \overline{u'w'} \\ \overline{v'w'} \end{bmatrix} \mathrm{d}x\mathrm{d}y}^{Reynolds\ force} \\ &\overbrace{-\int_{aghi} \begin{bmatrix} p & 0 \\ 0 & p \end{bmatrix} \overrightarrow{n}\,ds}^{Pressure\ force}\end{aligned} \tag{5.19}$$

5.4 Error Analysis

5.4.1 PIV Measurement Uncertainties

PIV sources of uncertainty can be divided into two groups; the random errors and the systematic errors.

In the results presented herein, main random errors were primarily caused by cross-correlation uncertainty, arising from the process of computing the position of the correlation peak with subpixel accuracy; a typical value of $\varepsilon_{cc} = 0.05 - 0.1$pixel standard error is associated with a three-point Gaussian peak fit estimator using uniform weight kernels (see Westerweel *et al.* (1993)). Due to statistical convergence, the effect of this uncertainty decreases with the square root of the number of samples (here$N = 100$). Thus, the displacement error was reduced to $\epsilon = \frac{\varepsilon_{cc}}{\sqrt{N}} = 0.01$px, which, with a pulse separation between frames of $\triangle t = 100\mu$s, entailed a relative velocity uncertainty of less than 0.1m/s (2% of the free stream tunnel velocity V_∞= 6m/s).

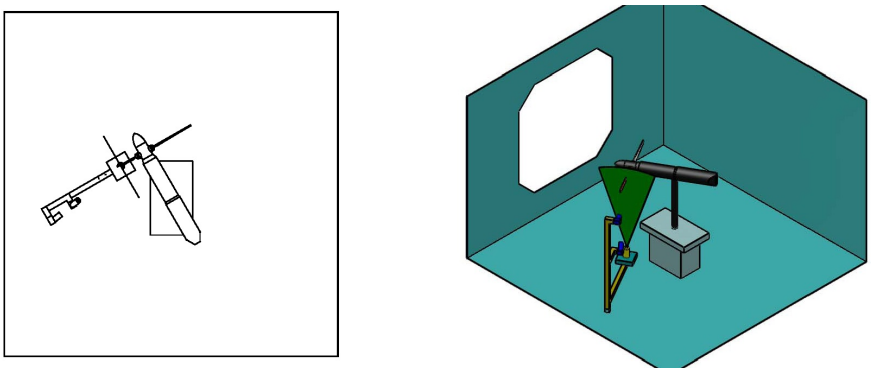

a) Suction side configuration.

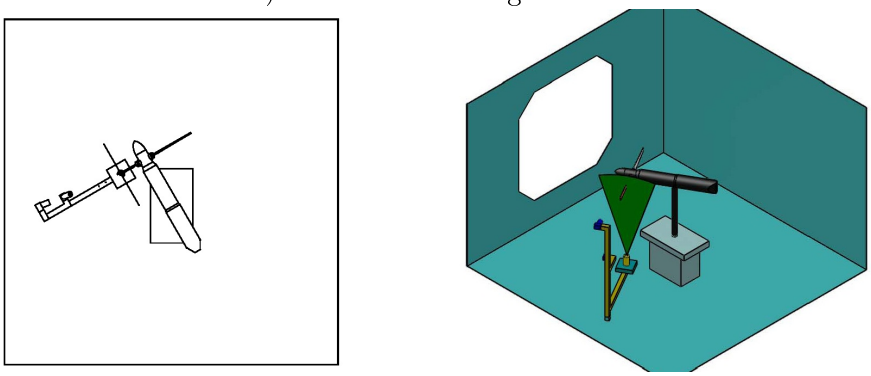

b) Pressure side configuration.

Figure 5.8: 3D PIV-Loads set up: 30º yawed flow conditions.

Peak locking was one of the two more relevant sources of systematic errors in the current study. This error consists of an improper sub-pixel displacement estimation that tends to bias the results towards integer values (see Raffel *et al.* (1998)), and becomes an important issue if the size of the particle image is too small ($d_\tau < 2$px), which is not the present case. The error due to peak locking $I_\varepsilon$was assessed by a statistical analysis on the displacement histograms, plotting the difference between the estimated shifts and their rounded off values. The result brought up a bias displacement error of $\varepsilon_{pl} = 0.02$px, which lead to an uncertainty in velocity of less than 0.2m/s.

Spatial resolution was the other relevant cause for systematic errors; if the interrogation windows used to process the data are not small enough, there might be deformation or rotation of the flow inside the area of study, leading to a loss of correlation. In the images processed herein, this problem was only present in the thin region of the airfoil's viscous wake (see Figure 5.9). With an interrogation area of IA $= 1.78 \times 1.78$mm, the minimum structure that can be resolved with 90% accuracy is $\lambda_{sr90} = 2.1$mm, as shown by Schrijer and Scarano (2008).

Table 5.4 summarizes the velocity uncertainties associated to random and systematic errors in the present study.

5.4.2 Load Calculation Uncertainty

Concerning the fluctuation levels, there was a big difference between the wake regions and the rest of the flow field. Thus, in the wake area the turbulence intensity reached $I =$

	Uncertainties	Reference	Velocity	Velocity Ratio
Random	Cross-correlation	$\varepsilon_{cc} = 0.1$px	$\triangle V \leq 0.1$m/s	$\triangle V/V_\infty \leq 0.02$
Systematic	Peak Locking	$\varepsilon_{pl} = 0.02$px	$\triangle V \leq 0.2$m/s	$\triangle V/V_\infty \leq 0.035$
	Spatial resolution	$\lambda_{sr90} = 2.1$mm	$\triangle V \leq 1.2$m/s	$\triangle V/V_\infty \leq 0.2$

Table 5.4: SPIV uncertainties.

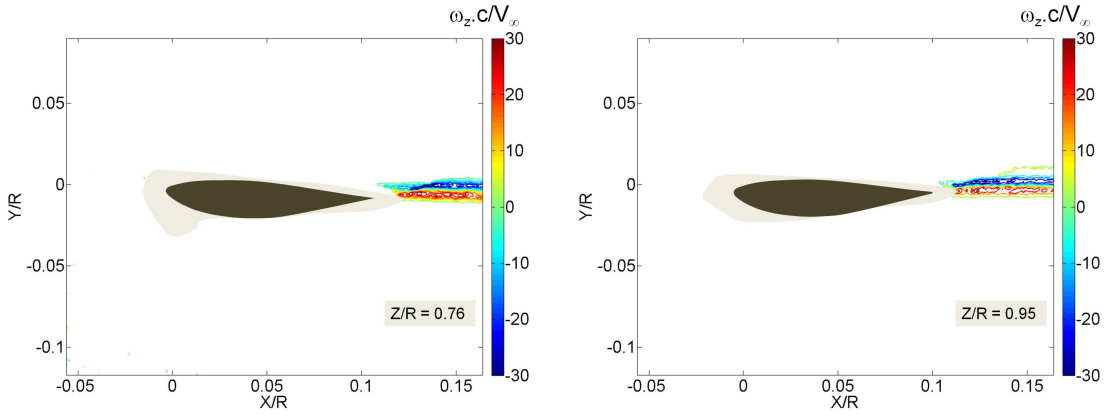

Figure 5.9: Blade section non-dimensionalized wake vorticity at different span positions.

$\frac{V_{rmse}}{\overline{V}} = 2$ in some parts of the blade (where $V_{rmse} = \sqrt{\frac{1}{3K}\left(\sum (u')^2 + \sum (v')^2 + \sum (w')^2\right)}$ is the turbulence strength and $\overline{V}$ is the mean velocity), while in the rest of the flow field investigated, it did not exceed $I = 0.01$ in any case. The free stream turbulence intensity in the Open Jet Facility is smaller than $I = 0.003$. In order to account for these turbulent effects, Reynolds stress terms were taken into account in the load calculations.

PIV errors together with turbulence intensity, specially in the wake region, are responsible for deviations in the load measurements when applying different integration paths, for their calculation. The uncertainties on the single values of the normal and tangential forces were thus based on the standard deviation of the different values computed with different contours. Taking into account the 25 planes studied and making use of 15 different integration contours, the maximum standard deviation of the normal forces was 0.17 N/m, while the maximum standard deviation of the tangential forces was 0.39 N/m.

5.5 Results and Discussion

5.5.1 Axial Flow Conditions

The flow around the blade of a HAWT model was investigated by means of SPIV in 25 phase-locked sectional planes located along the span, from positions Z/R = 0.37 to Z/R = 0.99. Near the tip the planes were acquired closely spaced between each other ($\triangle Z/R = 0.01$) in order to better resolve the gradients of velocity in the out-of-plane component. In the mid region of the blade the flow does not overcome important variations radially and the planes were placed further from each other ($\triangle Z/R = 0.03$).

The left column of Figure 5.10 shows the total relative velocity around the airfoil, non-

dimensionalized with the relative free stream velocity, obtained with SPIV for different sections along the blade. The right column of the same figure depicts the same velocity planes provided by the panel method, for the same operating conditions. In terms of details, close to the surface of the blade or in the wake, there are some differences, since SPIV can not reach the surface of the blade and the thin viscous wake is not present in the panel code velocity fields (since the model only reproduces potential flow). Nonetheless, the external flow field shows good consistency in each of the planes studied between both methods, allowing to use the panel method as means of comparison to justify the use of the SPIV-Loads methodology in wind turbine aerodynamics.

When the turbine is operating at its optimal condition and axial flow, there is an increase of the local effective angle of attack when going from tip of the blade to the root of it. Figure 5.10 shows this increase in the local angle of attack; when moving from planes that are near the tip towards planes that are near the hub, there is an increase of velocity in the suction side and a decrease of velocity in the pressure side.

In the present study, the pressure in each plane was calculated using a Poisson solver algorithm. Figure 5.12 depicts two examples of reconstructed pressure fields at different span positions. All along the blade, the convective terms represented the major contribution to the pressure gradient in Equation 5.12. To a much lesser extent, Reynolds stresses were only important in the wake region of each plane, while the Coriolis force contribution was only relevant in the planes acquired near the tip of the blade. Viscous stresses were negligible everywhere.

Regarding total loads computation, the pressure term in Equation 5.2 represented one of the major contributions, together with the convective term, as can be seen in Figure 5.13. The contribution of the Reynolds stresses was small, and that of the viscous stresses completely negligible. The Coriolis force was important in order to accurately measure tangential loads.

The PIV-Loads code was first tested with synthetic 2D DNS data (provided by Albrecht *et al.* [3]) producing accurate results. However, when using experimental PIV data, there are always uncertainties such as peak locking, lack of spatial resolution in the wake and laser reflections (resulting in masked areas), that can lead to some source of error in the loads estimation. Final SPIV-Load estimation results for each of the 25 planes examined are summarized in Figure 5.15, together with the results provided by the panel method code and the BEM code, which were included as means of comparison.

PIV normal force calculations show the same tendency as the panel code, and the values are in close agreement near the tip of the blade and passed the half span of it. However, between these two regions, there is an offset of 10% in the values, approximately. The discrepancies found in these axial loads are mainly attributed to the potential character of the panel code (given the fact that $Re \sim 10^5$ in the experimental case).

Regarding tangential forces, PIV results follow the same tendency of the ones produced by the panel code. However, tangential force results estimated with SPIV are not as smooth and show some fluctuations; the wake region here is playing an important role, and in this area SPIV uncertainties are larger due to the lack of spatial resolution. It is therefore difficult to have accurate pressure information on the wake and this leads to results that show a bigger dependency on the integration path chosen. An example of load calculation results using different contours is shown in Figure 5.14, and the force standard deviations encountered for each plane are also depicted in Figure 5.15.

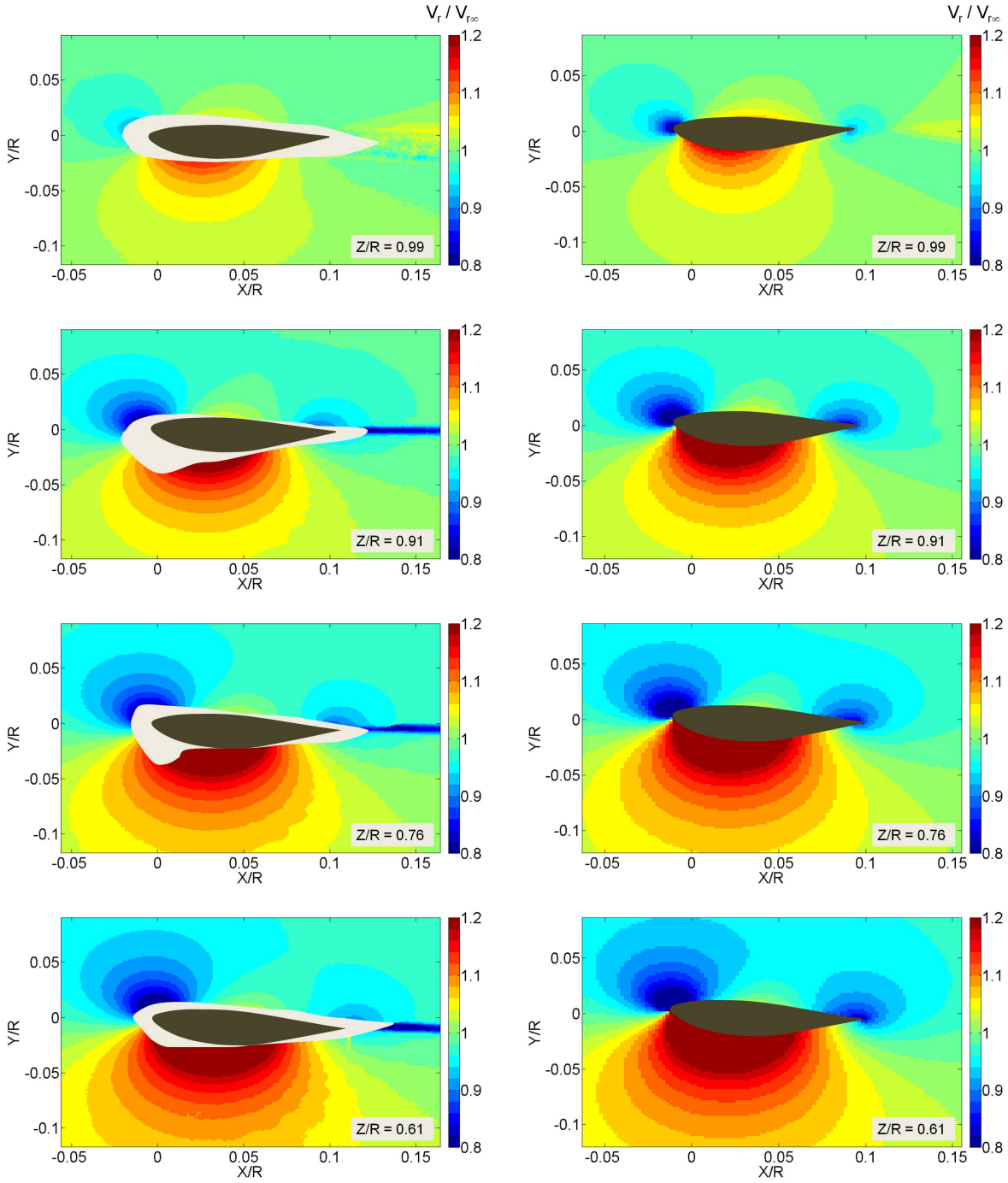

Figure 5.10: *Left:* Relative velocity magnitude obtained with SPIV. *Right:* Relative velocity magnitude provided by the panel method model.

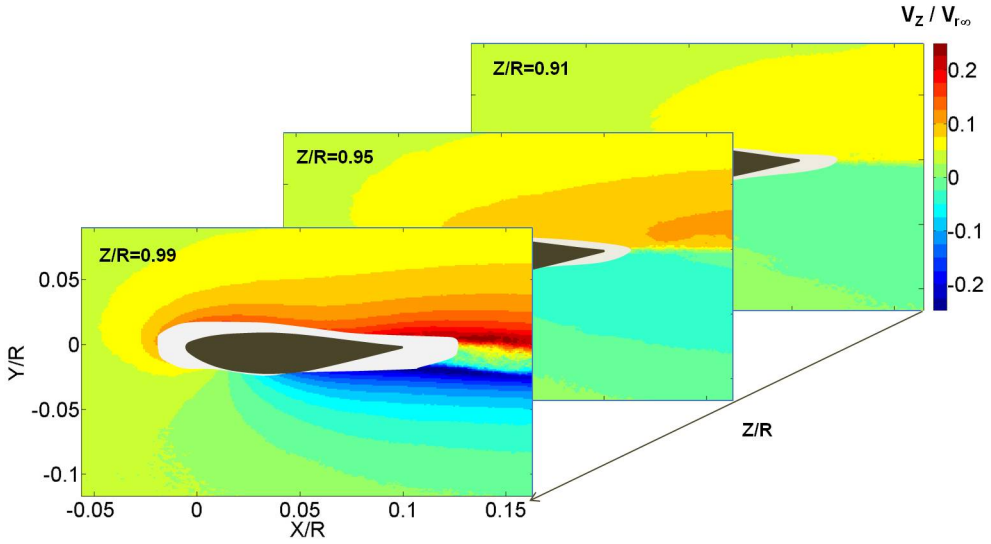

Figure 5.11: Relative radial velocity in three different planes near the tip of the blade.

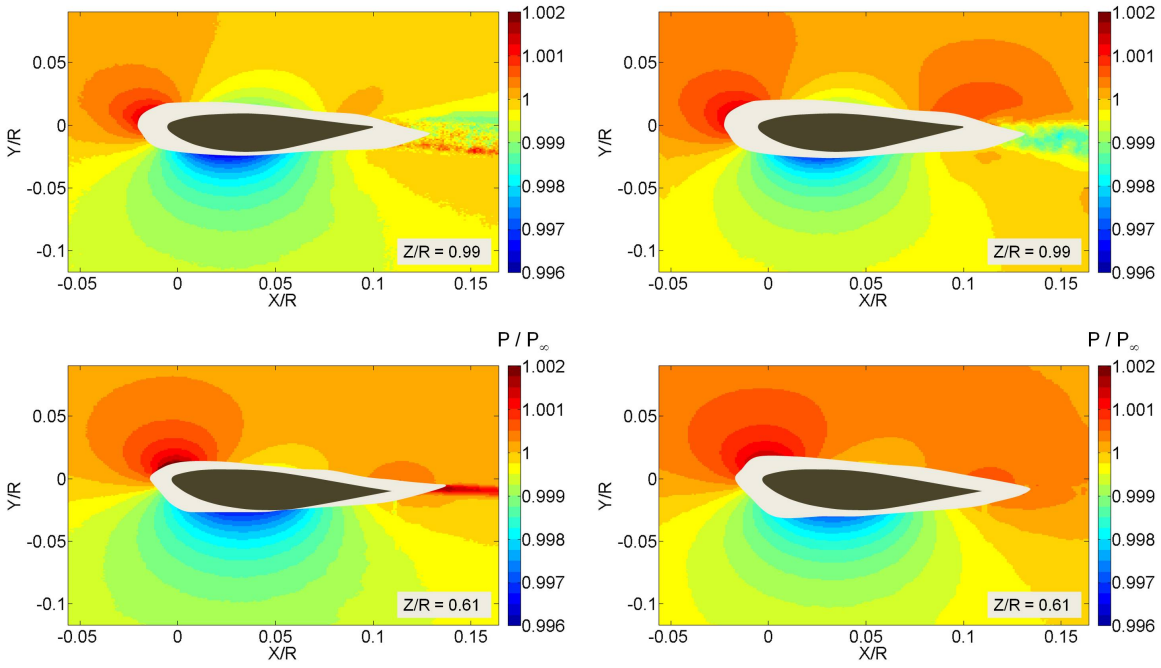

Figure 5.12: Pressure reconstruction for z/R = 0.61 and z/R=0.99 (*left:* Bernoulli, *right:* Poisson solver).

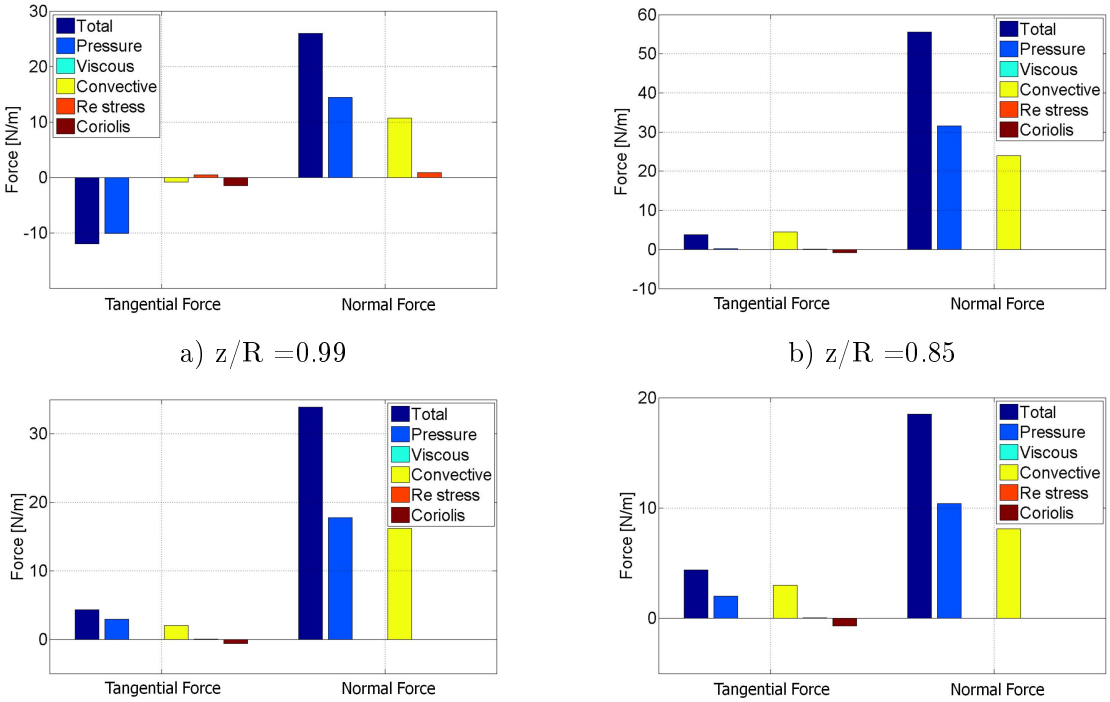

a) z/R =0.99 b) z/R =0.85

c) z/R =0.58 d) z/R =0.37

Figure 5.13: Contribution of the different Momentum Equation terms to the total force calculation at different span positions.

The computation of the surface integrals present in Equation 5.2 is approximate, due to the laser reflections that hinder obtaining velocity measurements in the area close to the airfoil surface. The bigger influence of this approximation is encountered in the contribution of the Coriolis term to the tangential force, in the planes near the tip of the blade, where the tip vortex produces intense radial velocities, as can be seen in Figure 5.11. Thus, near the tip region, masked areas where reduced as much as possible, although some level of uncertainty has to be taken into account due to this lack of information near the surface of the blade.

Finally, BEM code predicts normal forces in between the values produced by PIV and the Panel code, except for the region near the tip where the predictions are bigger than the other two. Regarding tangential forces, BEM predictions are higher than those provided by both PIV and the panel code, all along the blade, although following the same tendency. BEM simplifying assumptions together with SPIV mentioned uncertainties can be responsible for these discrepancies. Overall there is a good consistency of the results, and BEM predictions have been included in the comparison for completeness.

5.5.2 Yaw Flow Conditions

The main purpose of this yawed condition experiment was to measure forces on blade in conditions that would resemble, more realistically, real working conditions of a wind turbine. If the flow is yawed by 30^{o}, there is no azimuthal symmetry in the blade rotating trajectory, and the steady condition can no longer be applied in the formulation, regardless of the frame of reference chosen.

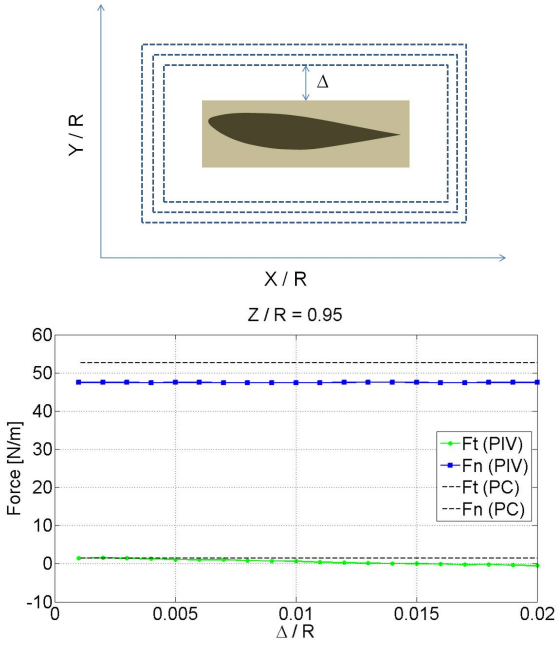

Figure 5.14: Influence of the integration path for panel code and SPIV load calculations (F_t= Tangential force, F_n= Normal force)

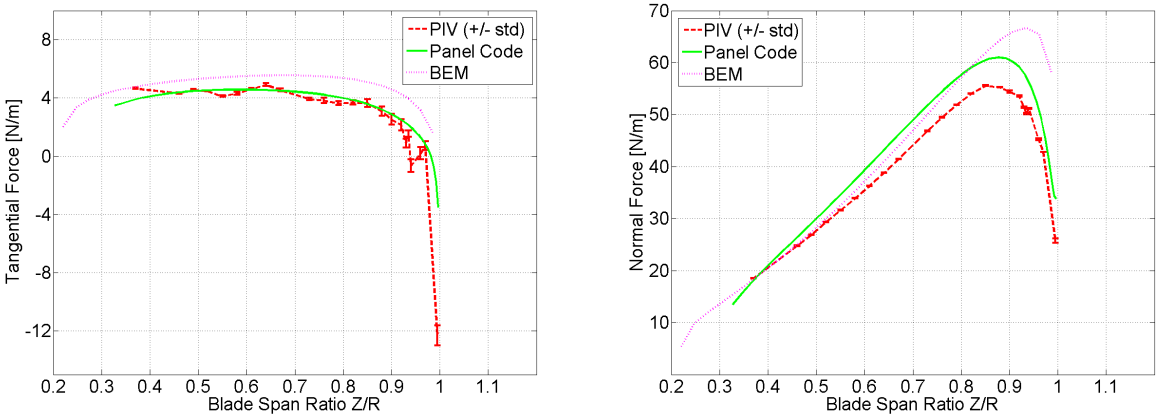

Figure 5.15: Load calculation per unit length along the blade (*left:* Tangential force, *right:* Normal force)

In order to visualize the flow around the blade, 21 span positions were considered, which ultimately brought about force measurements in 7 different planes. In the planes where forces wanted to be calculated, three SPIV images were acquired, corresponding to three different time instants.

Figure 5.16 shows absolute and relative velocity fields for four different span positions. Regarding absolute velocities, it is interesting to note how near the tip, velocities are very small in the downwash region, near the trailing edge: this is a clear evidence of the tip vortex that is slowing the axial flow. This effect, indeed, disappears when moving towards the hub of the blade. Although same tip vorticity is obviously present when showing relative velocities, the effect in the representation is not so clear, since the blade velocity is much higher than the undisturbed flow (TSR = 7). On the other hand, when looking to relative velocities, it is evident that at the mid span (z/R = 0.46), where the chord of the airfoil is bigger (and therefore also its thickness), the viscous wake is also thicker. Lastly, it can be observed that the angle of attack increases towards the hub and that the flow is attached around the airfoil in every span position studied.

Radial velocity in the blade is now increased due to the 30^{o} flow yaw angle: For the 90^{o} azimuth where SPIV were carried out, this yaw angle, together with a 6 m/s tunnel velocity, results in a radial velocity of 3m/s and an axial velocity of 5.3 m/s, relative to the blade. On the one hand, smaller axial velocity will derive in smaller loads impinged on the blade, since the angle of attack will be reduced all along it. On the other hand, bigger radial velocities will enhance the Coriolis contribution to drag when using a moving frame of reference. The increase of radial velocity due to yaw can be clearly seen if Figure 5.17 and Figure 5.11 are compared, since they plot radial velocities in the yaw and axial cases, respectively. The tip vortex generated can also be identified if the planes z/R = 0.99 and z/R = 0.89 are considered.

With the aim of computing forces as accurately as possible and study the differences encountered following different approaches, three different formulations were considered, as explained in Section 5.3.2. The first one uses a moving frame of reference, following a similar methodology as the one proposed for axial flow. The last two use a stationary frame of reference. Figures 5.18, 5.19, 5.20 and 5.21 reproduce the different contributions, of the ME in its differential form, to the pressure gradient: the first two figures illustrate the results based in a moving frame of reference while the last two figures represent the stationary frame of reference results. It is important to note the convective acceleration terms were only outstanding contribution to the pressure gradient, when considering a moving frame of reference; whereas this position was occupied by the local acceleration terms (non steady terms), when considering a stationary frame of reference. Another issue that arises from this comparison ,is the fact that the pressure gradient calculated with a moving frame of reference, is more affected by the peak locking effect (see Figure 5.18a)), and is therefore less smooth. This fact could lead to a lower accuracy in the pressure calculation.

Figure 5.22 shows the pressure field calculated with the Poisson solver by means of stationary frame of reference formulation. The figure is compared with the pressure field calculated with the Bernoulli equation. The differences encountered in the wake region emphasize the importance of using a non-potential solver, since the pressure recovery near the trailing is decisive for the generation of torque.

Finally, aerodynamic forces are calculated with the three different approaches exposed, and the results are presented in Figure 5.23. One of the main sources of error, regarding

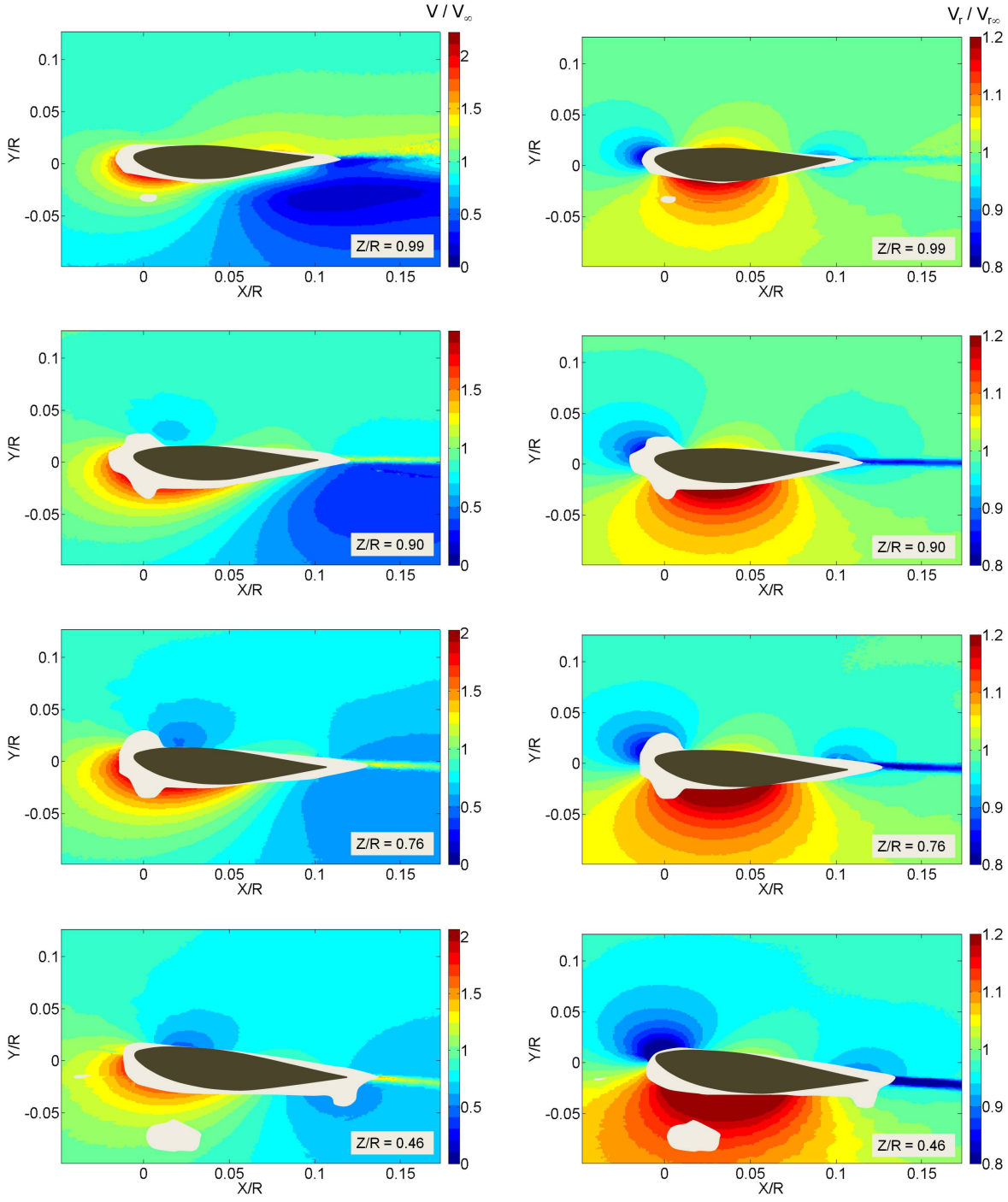

Figure 5.16: Blade section relative velocity fields, in yawed flow (*left:* absolute velocities, *right:* relative velocities).

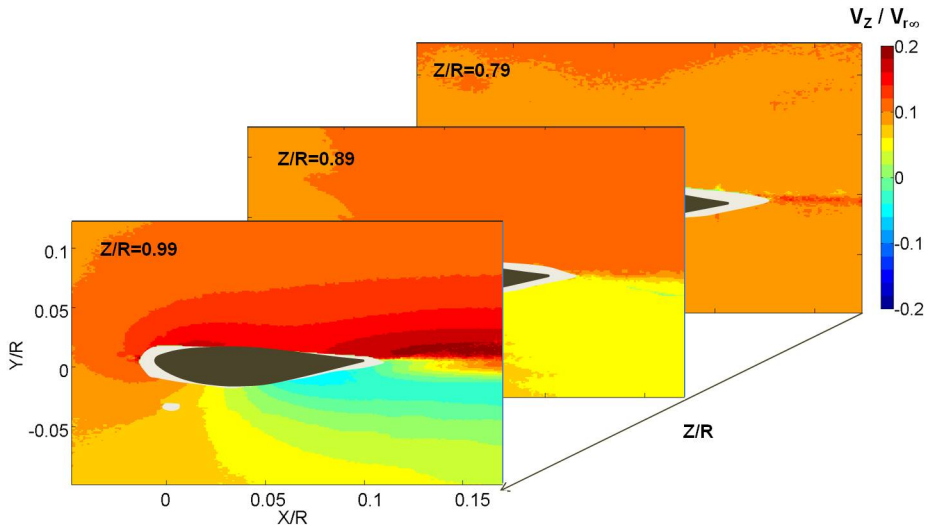

Figure 5.17: Radial velocity in yawed flow (non-dimensionalized with non-disturbed relative velocity).

the moving frame or reference formulation, is that, although the frame of reference is fixed to the blade and moves with it, the SPIV equipment did not move with the blade; this meant that images had to be cropped manually, to simulate the displacement the equipment should have had. Thus, non-steady terms had less accuracy with this methodology. Another source of error was that introduced by peak-locking when calculating the pressure gradient, as was previously discussed. Lastly, lack of accuracy in radial velocities could be originating uncertainties in the non-inertial terms, which have a big importance in the tangential force calculation, as can be seen in Figure 5.24.

Hence, stationary frame of reference results were more satisfactory. Nevertheless, using the formulation disclosed in Section 5.3.2.2 still did not render a good agreement with the panel code predictions, regarding tangential forces. Unsteady terms of the ME in its integral form (see Equation 5.14) were the main source of error, as can be seen in the left side of Figure 5.24. Indeed, the volume integral associated with these non steady terms could not be accurately evaluated, due to laser reflections next to the blade and the lack of resolution in the wake. This reason led to the decision of implementing the derivative-moment transformation (DMT) proposed by Wu et al. (2005), presented in Section 5.3.2.2, that transforms the volume integral of the unsteady terms, into a surface integral. This way, the information needed to calculate the local acceleration terms (unsteady terms) was less error-prone, and the tangential force results were consistent with those predicted by the Panel code.

Normal forces calculations can be considered acceptable for all cases. Pressure and local acceleration terms were the main sources of thrust in the moving frame of reference, whereas for the stationary frame of reference, pressure and convective acceleration terms were the principals sources of thrust, as can be seen in the right side of Figure 5.24.

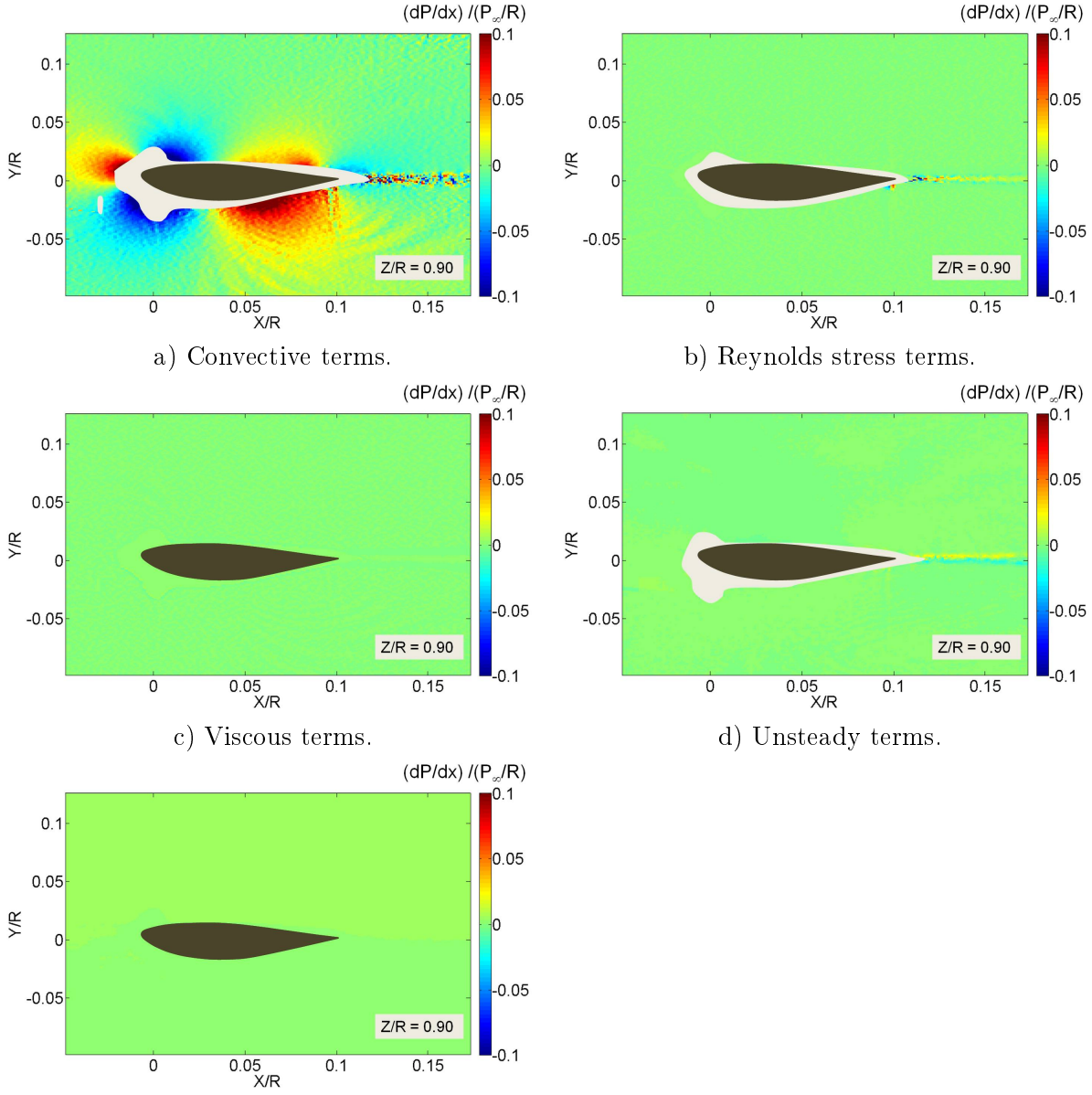

a) Convective terms.

b) Reynolds stress terms.

c) Viscous terms.

d) Unsteady terms.

e) Non inertial terms.

Figure 5.18: Yawed flow case: dp/dx contributions in the moving frame of reference.

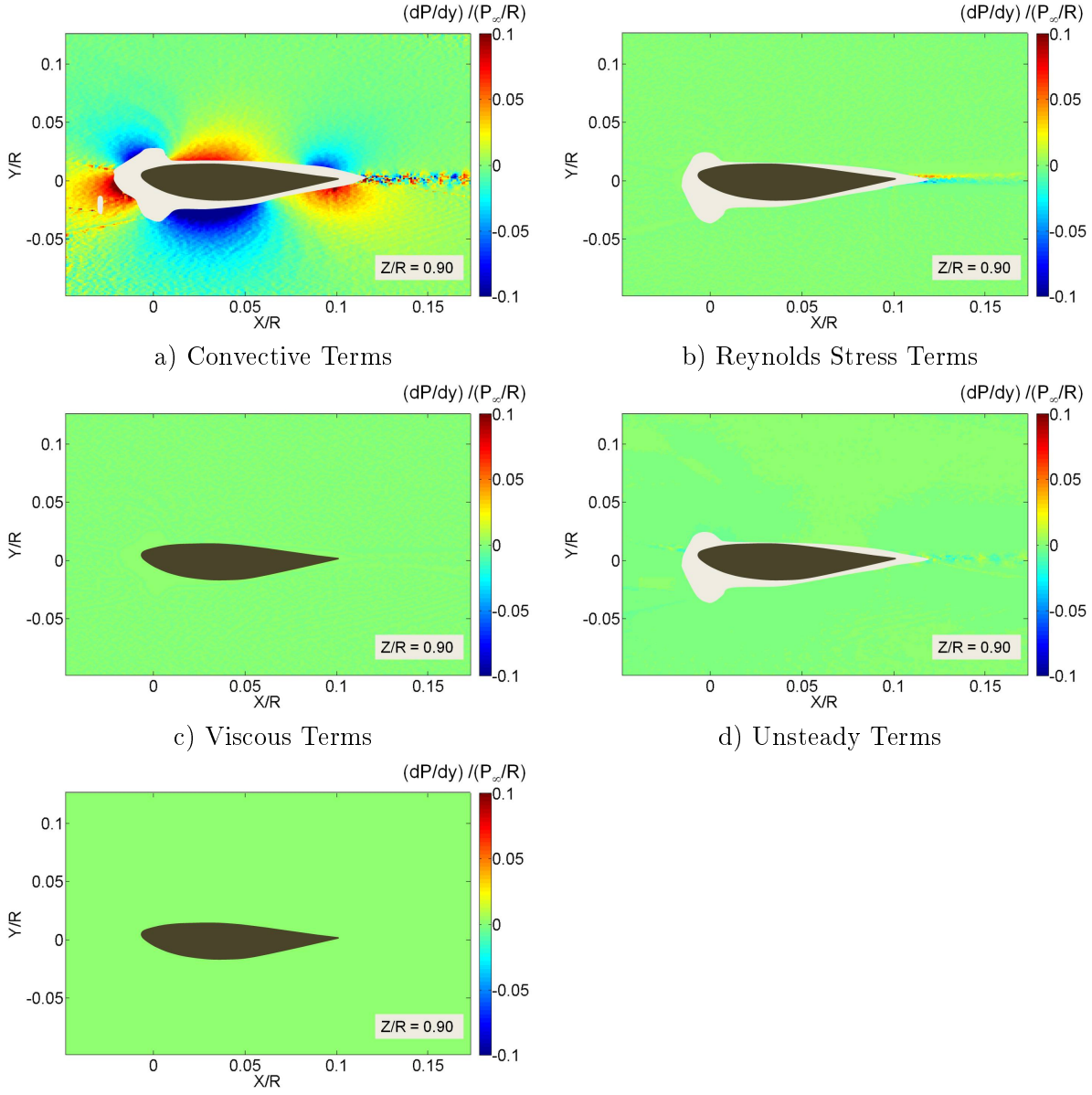

a) Convective Terms

b) Reynolds Stress Terms

c) Viscous Terms

d) Unsteady Terms

e) Non Inertial Terms

Figure 5.19: Yawed flow case: dp/dy contributions in the moving frame of reference.

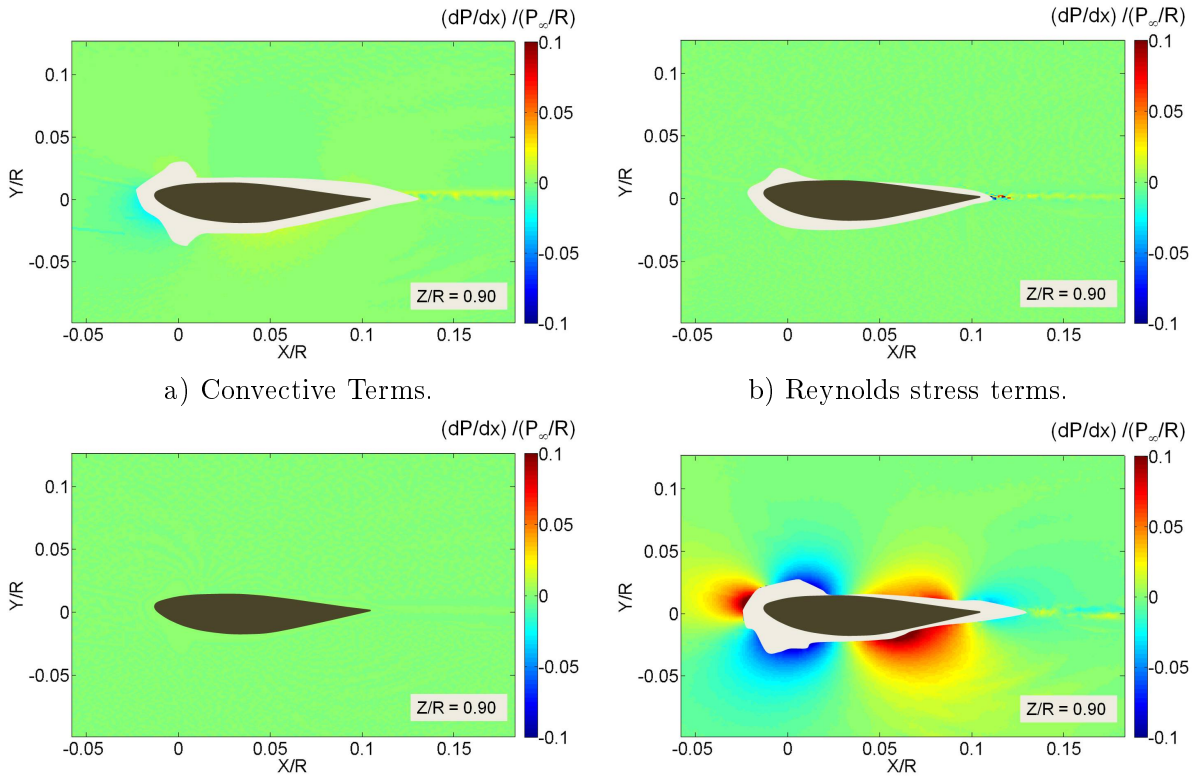

a) Convective Terms.

b) Reynolds stress terms.

c) Viscous stress terms.

d) Unsteady terms.

Figure 5.20: Yawed flow case: dp/dx contributions in the stationary frame of reference.

5.6 Conclusions

The aerodynamic loads acting on a Horizontal Axis Wind Turbine blade have been assessed by means of a non intrusive technique using Stereoscopic Particle Image Velocimetry. The HAWT model had a diameter of 2m and was operating at its optimal tip speed ration in axial flow (TSR = 7). In total, 25 phase-locked sectional planes of the blade were investigated, and both tangential and normal forces were estimated in each of these planes.

Pressure reconstruction was carried out by means of a Poisson solver, avoiding the accumulated errors associated with marching-schemes algorithms. Results evidenced the importance of using a pressure solver that would assumed non potential flow, assuring a reliable pressure reconstruction in the wake region, leading to consistent results of the torque generating forces.

Concerning the 3D flow visualization around the blade undertaken, it was interesting to study the increase of angle of attack that took place in the blade when moving towards the hub. Besides, the flow observed was attached in every span position considered, and the viscous wake grew thicker also when moving towards the hub, because of the chord law. Moreover, tip vorticity could also be characterized.

In the case of axial flow conditions, a moving frame of reference was considered for the formulation. The convenience of this election lied in the azimuthal symmetry of the flow around the rotating blade (i.e, the blade sees and identical flow field in its rotating movement, regardless of the azimuthal position); this symmetry eliminated the non steady terms

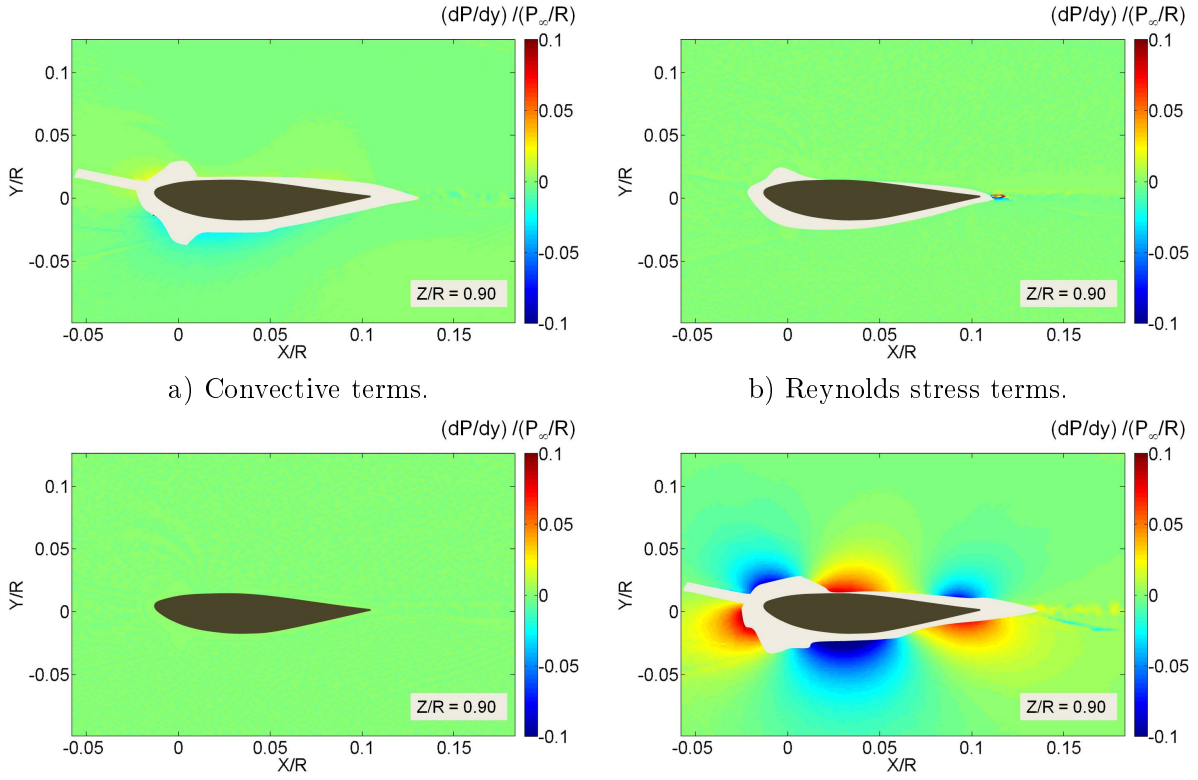

a) Convective terms.

b) Reynolds stress terms.

c) Viscous stress terms.

d) Unsteady terms.

Figure 5.21: Yawed flow case: dp/dy contributions in the stationary frame of reference.

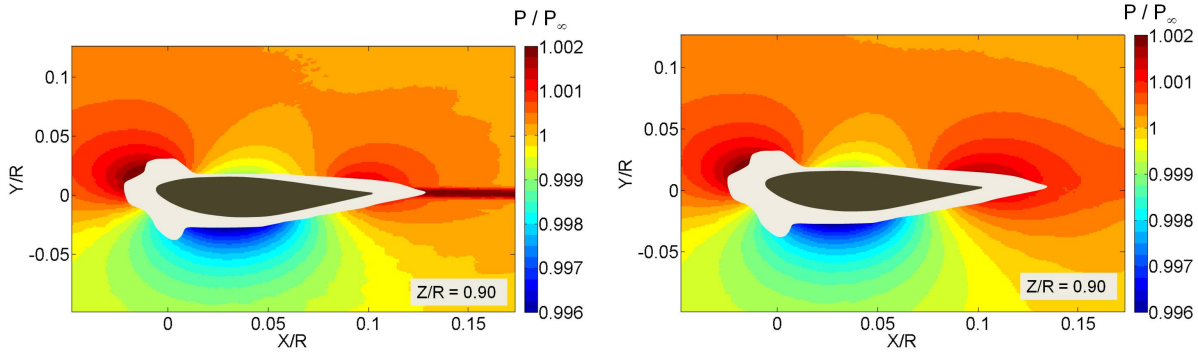

Figure 5.22: Comparison of pressure fields, in the yawed flow case (*left:* Bernoulli, *right:* Poisson solver).

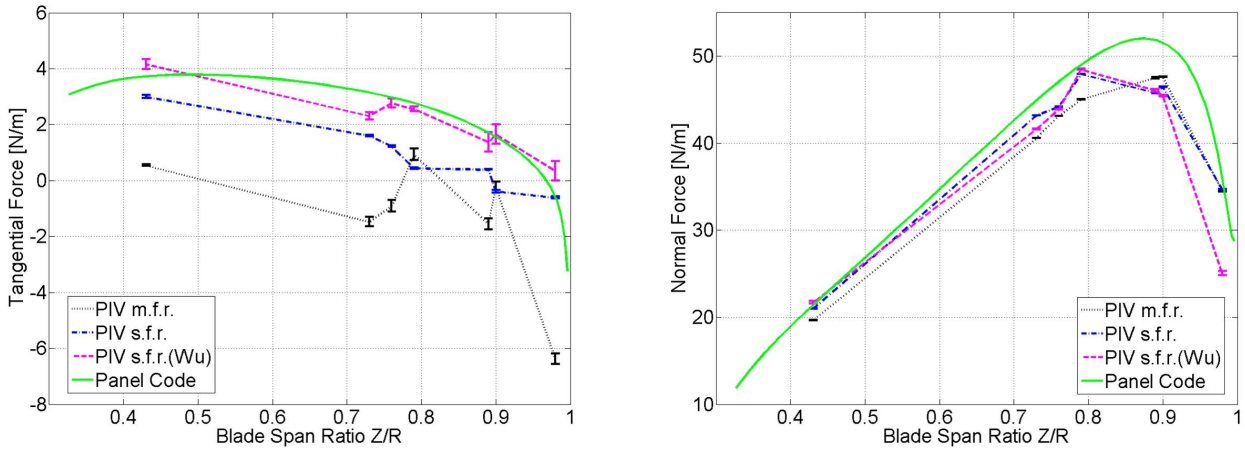

Figure 5.23: Comparison of the load calculation results along the HAWT blade, for the yawed flow case (*m.f.r.:* moving frame of reference, *s.f.r.:* stationary frame of reference).

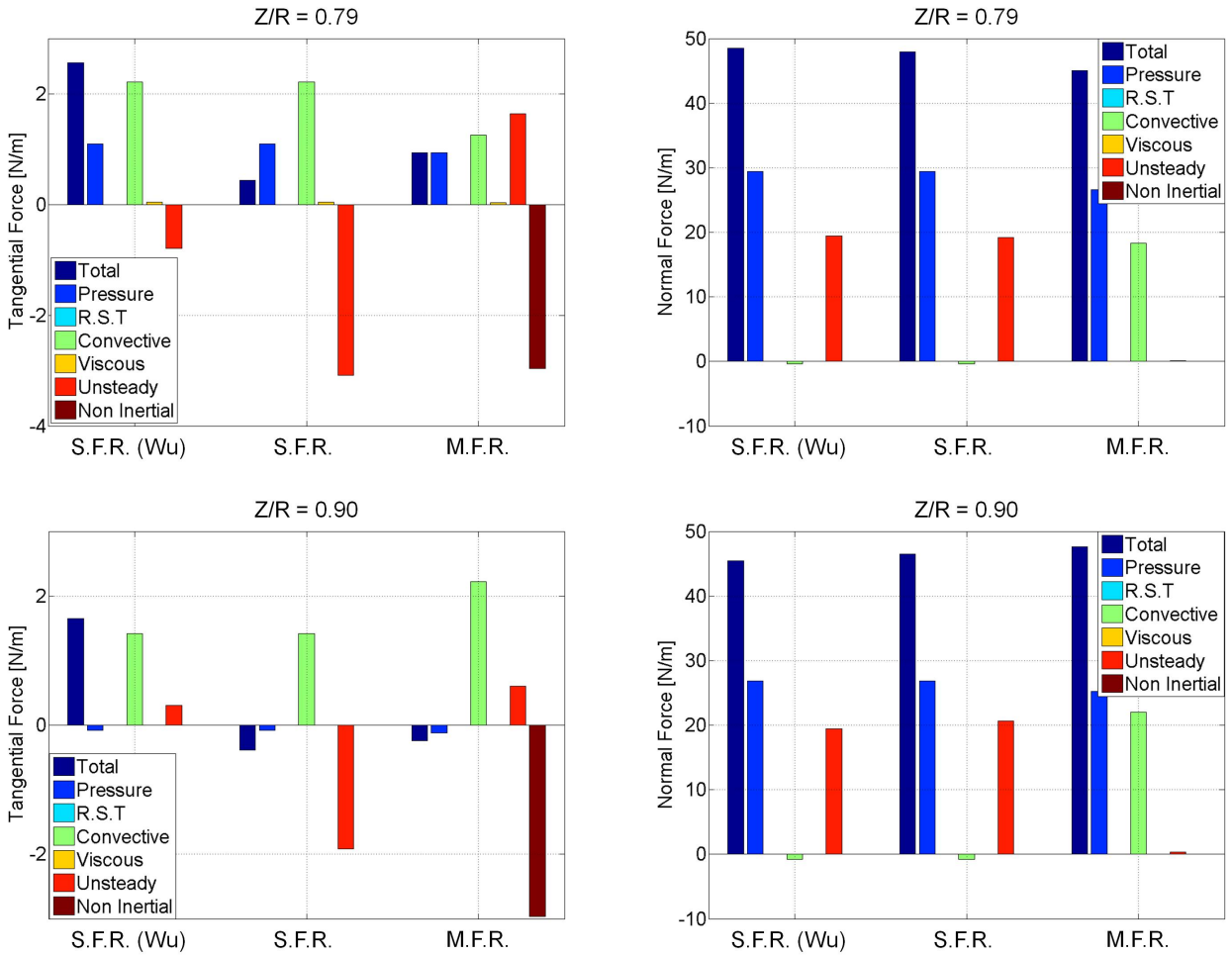

Figure 5.24: Contributions of the ME terms to the total force calculation, for the yawed flow case (M.F.R: moving frame of reference, S.F.R.: stationary frame of reference).

in the equations, when using a frame of reference that was fixed to the blade.

The results proved a very good consistency with those provided by the panel code implementation: regarding lift, there was an offset (less than 10%) near the tip region, and for the rest, the curve tendencies (force per unit length along the blade) matched perfectly. On the other hand, tangential force values results had good consistency in terms of values with the panel code ones, although the curve tendency was not so smooth.

Moreover, in the case of yawed flow conditions, it was proved that using a stationary frame of reference was more convenient for this case, where unsteadiness of the flow had to be considered (even when using a moving frame of reference). However, local acceleration terms (unsteady terms) involve a volume integral in the conventional ME formulation: due to laser reflections near the model, and lack of resolution in the wake, this volume integral introduced large errors in the tangential force calculations. Thus, a derivative-moment transformation (DMT) was applied, converting the volume integral into a surface integral, and providing a less error-prone methodology.

Final results using a stationary frame of reference together with DMT found good consistency with those provided by the panel code. Similar conclusions as those met for the axial flow calculations were presented: the normal force curves followed a similar tendency, although a 10% offset could be found near the tip region, and, regarding tangential forces, the values were consistent, but the ME results were more disperse and did not depict a smooth curve.

In short, main problems encountered were due to PIV uncertainties such as peak locking, lack of spatial resolution on the wake region and laser reflections hindering the observation of the area closely surrounding the airfoil. Any technological improvements in this direction would certainly lead to a more reliable implementation of the method. The use of a panel code approach has served as a preliminary comparison to justify the use of the SPIV-Loads methodology in wind turbine aerodynamics. Future work will focus on CFD based approaches.

This research provided a new way of measuring aerodynamic loads with a non intrusive technique on a wind turbine with an acceptable accuracy. The methodology allows to experimentally measure forces without the need of pressure taps, which are complicated to implement and, in some cases where the model is small, almost unfeasible. In addition, the method provides with consistent pressure fields around the blade together with a complete insight of the velocity field.

Finally, the technique offers the possibility of testing the efficiency of active load control methods or deeper studying rotational effects. Using higher resolution cameras and time resolved SPIV, the method would also work for blades that are stalled, enlarging the possible operating HAWT regimes that can be investigated.

Chapter 6

Visualization of the Near Wake of a HAWT

6.1 Introduction

In this chapter, the near vortex wake of a HAWT model was investigated, focusing on the tip vortices. Besides, the vorticity field around a section of the HAWT blade was also studied, with the aim of providing a basis to evaluate the resulting unsteady forces through the Momentum Equation.

Nowadays, standard codes for calculating and predicting wind energy aerodynamics are based on simplifying hypothesis, which allow them to offer a good compromise between computational cost and reliability. However, these assumptions lead to results that are not always as precise as needed. It is therefore important that some effort is made to characterize the flow around a wind turbine rotor, in order to have a wide experimental database, that would serve as a means of validation for new prediction codes.

Firstly, the aerodynamics of the HAWT were addressed through BEM. This theory was implemented in a code which was subsequently validated with existing experimental data, and then used to design a HAWT model. The constructed model had a 38cm diameter, two blades, GOE531 airfoil all along the blade, twist and no pitch. Its near wake was studied both with TRPIV (1000Hz) and PIV (15Hz), on planes containing the axis of rotation. The results depicted the velocity and vorticity fields of the near wake up to one radius distance downstream. The tip vortices were visualized, and their evolution and dissipation were characterized. Axial and tangential velocity were also measured and compared to BEM predictions.

Secondly, the flow field around a rotating blade element situated at the blade mid-span was investigated. The TRPIV images presented a sectional view of the blade, just as the cases presented in Chapters 4 and 5. The aim of this experiment was to bring up a future research, linking the concepts of shed vorticity and load calculation on the blade. This approach has been recently undertaken by Jardin *et al.* (2009).

Due to the available apparatus, the experiments were undertaken at low Reynolds numbers ($\mathrm{Re} \sim 10^4$). Although this is not the regime in which big commercial wind turbines work, a good characterization of the near wake at low Re is important for the development of small domestic wind turbines. This area, which have been called "Micro Wind Energy," is

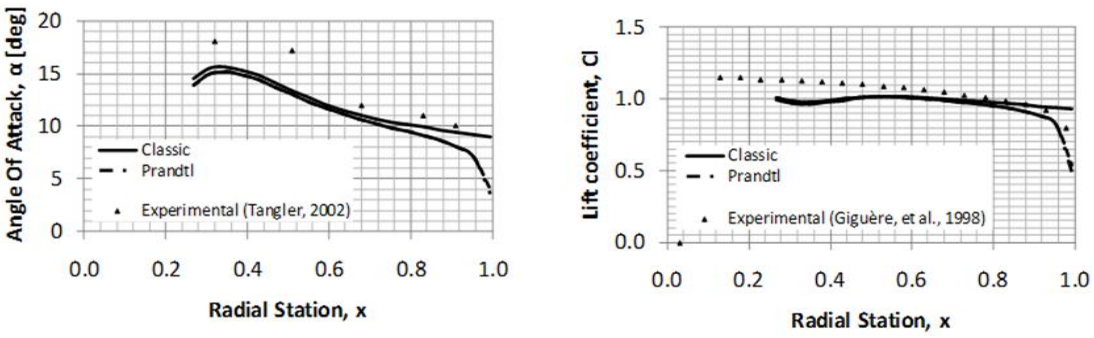

Figure 6.1: Comparison of BEM code and NREL experimental results

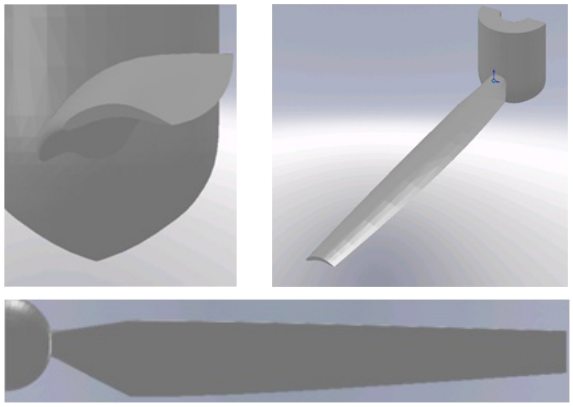

Figure 6.2: Details on the HAWT model design.

gaining more and more popularity, and there is a possibility that it will become a frequent energy resource in the future.

The experimental campaign constituted the initial investigation done for this PHD thesis dissertation, and was carried out in the Mechanical & Aerospace Laboratory, at Rutgers University (USA), in a water tunnel of $0.9 \times 0.55\text{m}^2$ test section. Although this chapter's topic might seem disconnected from the main purpose of the thesis, it was indeed an important step in the achievement of this research project, since it was decisive for focusing in what later became the main purpose of this investigation.

6.2 Optimization and Design of a HAWT Model via BEM

The BEM theory was used to design a HAWT model that could be used in the experiments presented herein. Firstly, as means of validation, the BEM code was run for a high Re case and the same parameters that described the NREL experiments undertaken by Guiguère *et al.* (1999) and those undertaken by Tangler *et al.* (2002). The results reproduced by the BEM code were consistent with those reported by NREL, as can be seen in Figure 6.1.

The code was then used to design a new model which would operate with Re $\sim 10^4$ and moderate tip speed ratios TSR ~ 4. The resulting geometry is presented in Figure 6.2and Figure 6.3. The model was manufactured using a rapid prototyping machine.

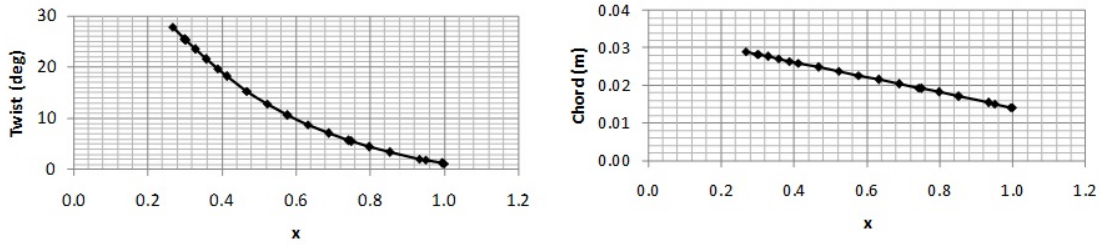

Figure 6.3: Twist and chord distribution of the HAWT model.

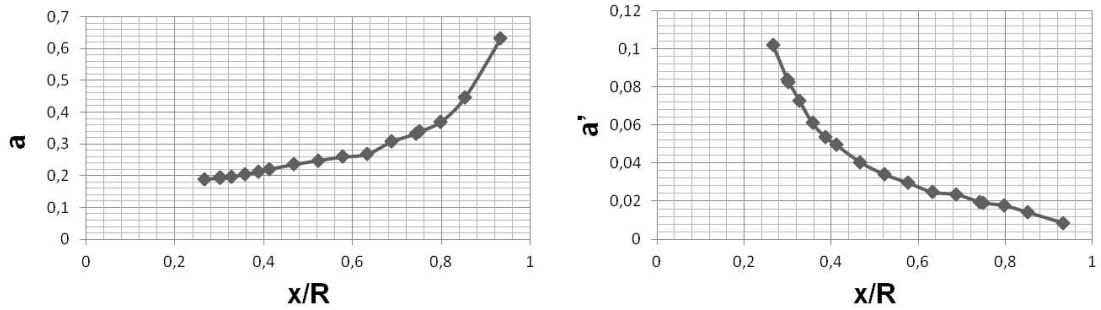

Figure 6.4: Axial (a) and tangential (a') induction factors predicted for the HAWT model.

Figure 6.4 shows the BEM performance predictions for the HAWT model, under conditions similar to those corresponding to the experimental case, i.e, $\Omega = 52$rpm and $V_\infty = 0.25$m/s. However, $\mathrm{Re} = 25,000$ is the smallest Re number for which there is lift and drag coefficients data available for the GOE531 airfoil, and the Re describing the water tunnel tests ranged between $\mathrm{Re} \sim 10,000 - 18,000$ (from hub to tip). Therefore, differences between BEM predictions and experimental results are expected: on the one hand, due to the lack of data available for actual Re conditions and, on the other hand, because of BEM simplifying hypothesis.

6.3 Experimental Set Up and Facilities

The experimental set up used for the measurements was composed by the following main items:

- Two different *objectives* were used with corresponding fixed focal lengths of $f_l =$ 100mm and $f_l = 50$mm and a minimum numerical aperture of $f^\sharp = 3.5$ and $f^\sharp = 1.4$ respectively.
- A combination of a *cylindrical lens* (25mm) and a *spherical lens* (1000mm) that formed the light sheet. In order to enlarge the divergence of the light sheet, another cylindrical lens (15mm) was used in the last experiments.
- *Hollow glass microspheres* of density 1.1g/cc and diameter between 30μm, used as tracers.
- A *synchronizer*.

a) TRPIV camera.

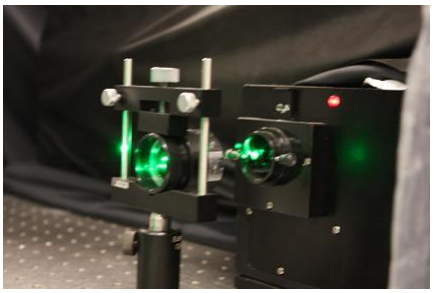

b) NdYag laser.

c) Micro-spheres.

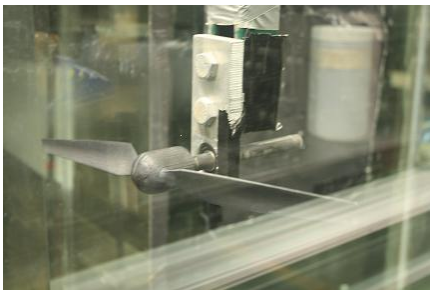

d) HAWT model.

Figure 6.5: Details on the near wake visualization experimental set up.

- Commercial Insight3G *software* .

Laser and camera were changed depending on whether conventional PIV or TRPIV was being used. In the case of TRPIV, these were the apparatus needed:

- *A dual NdYag laser* (Neodymium-doped Yttrium aluminum garnet) New Wave Pegasus. The energy per pulse of this laser is 10mJ at an optimum frequency of 1000Hz and its wave length is $\lambda = 527$nm.
- A *high speed camera* Photron Ultima APX which can obtain between 60-3,000 fps at maximum resolution (1024×1024pixels) and up to $250,000$ fps with reduced resolution (128×16pixels).

In the case of conventional PIV measurements, the set up was completed with the following items:

- A *dual NdYag laser* (Neodymium-doped Yttrium aluminum garnet) New Wave SoloPIV 120. The energy per pulse of this laser can reach 120mJ at a maximum frequency of 15Hz, and its wave length is $\lambda = 532$nm.
- Powerview *camera* (15fps at 1024×1024pixels).

6.3.1 Methodology

In order to redirect the laser light sheet to the place that wanted to be observed, a mirror was placed inside the tunnel, sufficiently downstream so that it would not affect the flow studied. In the last experiment configuration, the flow surrounding the blade had to

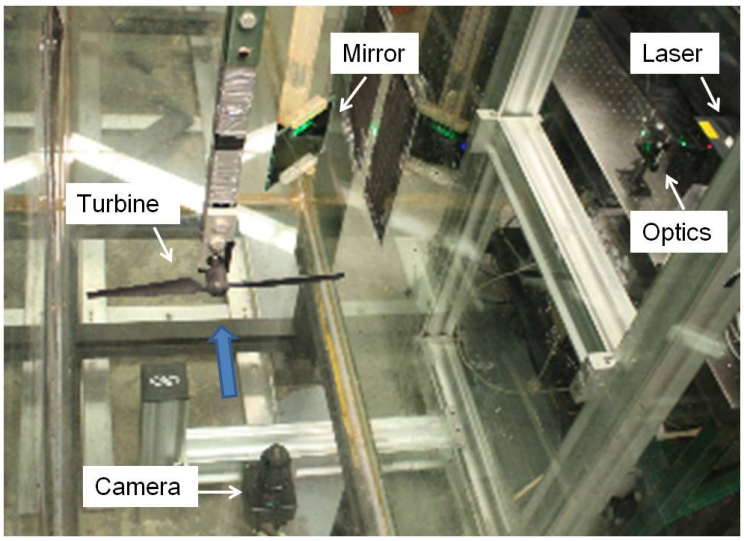

Figure 6.6: Near wake visualization experimental set up.

be visualized: in this case, the mirror was used to redirect the laser light once it had illuminated the zone that wanted to be studied, so that the shadows caused by the blade would be avoided. This proved to be a very good solution, as will be shown in Section 6.4.2.

When doing TRPIV, the laser optimum operation frequency was 1000Hz and therefore, the maximum time separation between frame A and frame B was 950μs. This time separation between frames was too short, since the free stream velocity of the flow was only 0.25m/s, and thus each seeding particle in the mean flow would only move one pixel when the two pair of images were analyzed. This could have caused too much uncertainty in the correlation technique. Because of this reason, it was decided to work with pairs of pictures that were taken with 2000μs time separation, both as frame A, and rename them as "new frame A" and "new frame B" respectively. With this solution not only the pixel displacement per particle was bigger but also the errors due to laser misalignment were avoided.

Raw images were analyzed using the Fast Fourier Transform correlation method (see Section 3.2.4), with interrogations windows of 32×32 pixels. The bad vectors encountered, which were in all cases less than 2% of the total, where replaced with the local median and the local mean was used to fill eventual holes.

For all the experiments described below, it will be considered that the blade has an azimuthal position of $\theta = 0°$when it is pointing towards the floor of the water tunnel (see Figure 6.6). The wind turbine moves counterclockwise when faced from upstream. Main experimental conditions are summarized in Table 6.1. Since the turbine model is driven by any motor, its rotation is due, uniquely, to the torque exerted by the fluid. Thus, slight differences in the free stream velocity in the tunnel result in different angular velocities of the model.

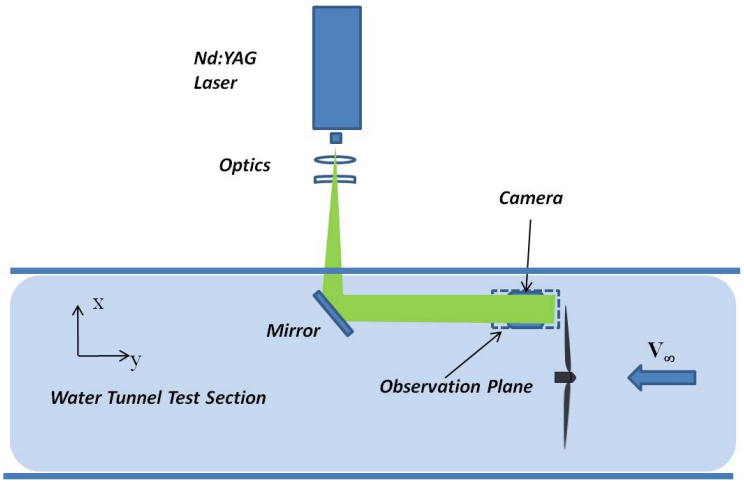

Figure 6.7: Scheme of the near wake visualization experimental set up.

	Wake (TRPIV)	Wake (PIV)	Blade (TRPIV)
V_∞	0.26 m/s	0.25 m/s	0.25 m/s
TSR	4.6	4.1	4.1
Ω	60 rpm	52 rpm	52 rpm
Re (tip)	18,000	16,000	16,000
fps	1000	14.5	1000
Δt	2000µs	2000µs	2000µs
$f^\sharp$	2	2.8	3.5
f_l	50mm	50mm	100mm

Table 6.1: Near wake visualization experimental conditions.

6.4 Near Wake Visualization

6.4.1 Near Vortex Wake

The wake of the HAWT model was studied by means of Time Resolved PIV (TRPIV). The field of view covered the part of the near wake that is next to the tip region, in order to visualize the tip vorticity shed. Figure 6.7 shows a schematic plant view of the set up. The tip speed ratio was TSR = 4.8 and maximum Reynolds was Re = 18,000, at the tip of the blade. Hollow glass microspheres of 30μm diameter were used as seeding particles, and a 50mm focal length objective with numerical aperture $f^\sharp$=2 provided with clear PIV images, even taking into account the loss of light due to the mirror.

The obtained velocity and vorticity fields are depicted in Figure 6.8. This figure shows the flow field from just behind the rotor to a distance of one radius downstream ($0 \leq y/R \leq 1$), in the region surrounding the tip of the blade ($0.9 \leq x/r \leq 1.1$). Tip vortices are clearly seen, and the distance between them is approximately 0.6 radius, resulting in a pitch of the helical vortex equal to $1.2R$, for a TSR = 4.8. This distance defines how compact the helical form of the wake is, and shows good consistency with the results published by Whale *et al.* (2000).

The TRPIV images were taken on a fully developed wake. Each picture shows, in fact,

a different vortex, which originated at the tip of the blade at a different instant (the visualization plane is fixed in space, but the wake is rotating and moving axially). This is the reason why, even if the frequency of images was very high (1000Hz), the form of the vortex is not continuous from one image to the other.

Since the tip vortices turn from the lower side of the blade to the upper side of it, the axial velocity is bigger in the outer part of the field wake, and smaller in the inner part of the wake, which can be also seen in Figure 6.9. The convective axial velocity of the vortex is almost 10% smaller than the mean axial velocity of the wake flow (for the same x/R).

In addition, a conventional PIV study was made with a similar configuration to the one used in the previous experiment. Working with a conventional PIV equipment offered some advantages: the laser power was bigger, and the visualization more precise, offering a bigger field of view. However, velocity information resolved in time was lost, since the frequency of acquisition shrinked to 15Hz. In the images shown in Figure 6.10 and Figure 6.11, the tip vortices are also clearly seen. These figures depict velocity fields (in the left side) and the corresponding iso-vorticity contours (on the right side), for different time instants, starting in the moment when the blade is passing by the plane of acquisition ($\theta = 90°$), and ending when the blade has moved almost half of one rotation ($\theta = 247°$), and a new vortex, corresponding to the other blade, is about to be generated. For TSR = 4.1, the vortices are separated a distance of 0.65radius, which results in a pitch of the helical tip vortex of $1.3R$. The core of the vortices can be identified in the contour plots inside the curves of maximum normalized vorticity.

Figure 6.12 features a juxtaposition of all iso-vorticity fields captured at different azimuthal angle of the blade. There is no substantial expansion of the wake in the region observed. The convective speed of the tip vortices is again almost 10% smaller than the mean axial velocity of the wake, at this x/R position. These results show good agreement with those published by Snel et al. (2007).

6.4.2 Velocity Field around a Rotating Blade Element

Finally, the flow around a blade section was visualized by means of TRPIV. The laser sheet was illuminating the blade at its midspan position ($x/R = 0.5$), at $\theta = 0°$ azimuthal position. The acquisition position remained fixed, and the images show the flow field resolved in time, for the different positions of the blade. The results allowed a better understanding of the 3D problem, and established the basis to investigate the relation between shed vorticity and unsteady loading.

The whole field of view around the blade element was resolved with just one image. This was achieved through the use of a mirror that redirected the light, with a slight angle displacement, enlightening the shadow zones, as can be seen in Figure 6.13. This set up configuration represents and advantage when compared with the methodology used in Chapter 5, since there is no need to combine two different phase-averaged images in order to have the whole velocity field around the blade.

The velocity and vorticity fields computed are shown in Figure 6.14, for the different azimuthal positions of the blade, all of them near $\theta = 0°$, which is the position in which the blade is completely perpendicular to the field of view. A mask has been used to avoid computing velocities in the regions with reflections coming from the blade. The velocity field show that the flow is producing lift, a part of which is used for moving the turbine. The

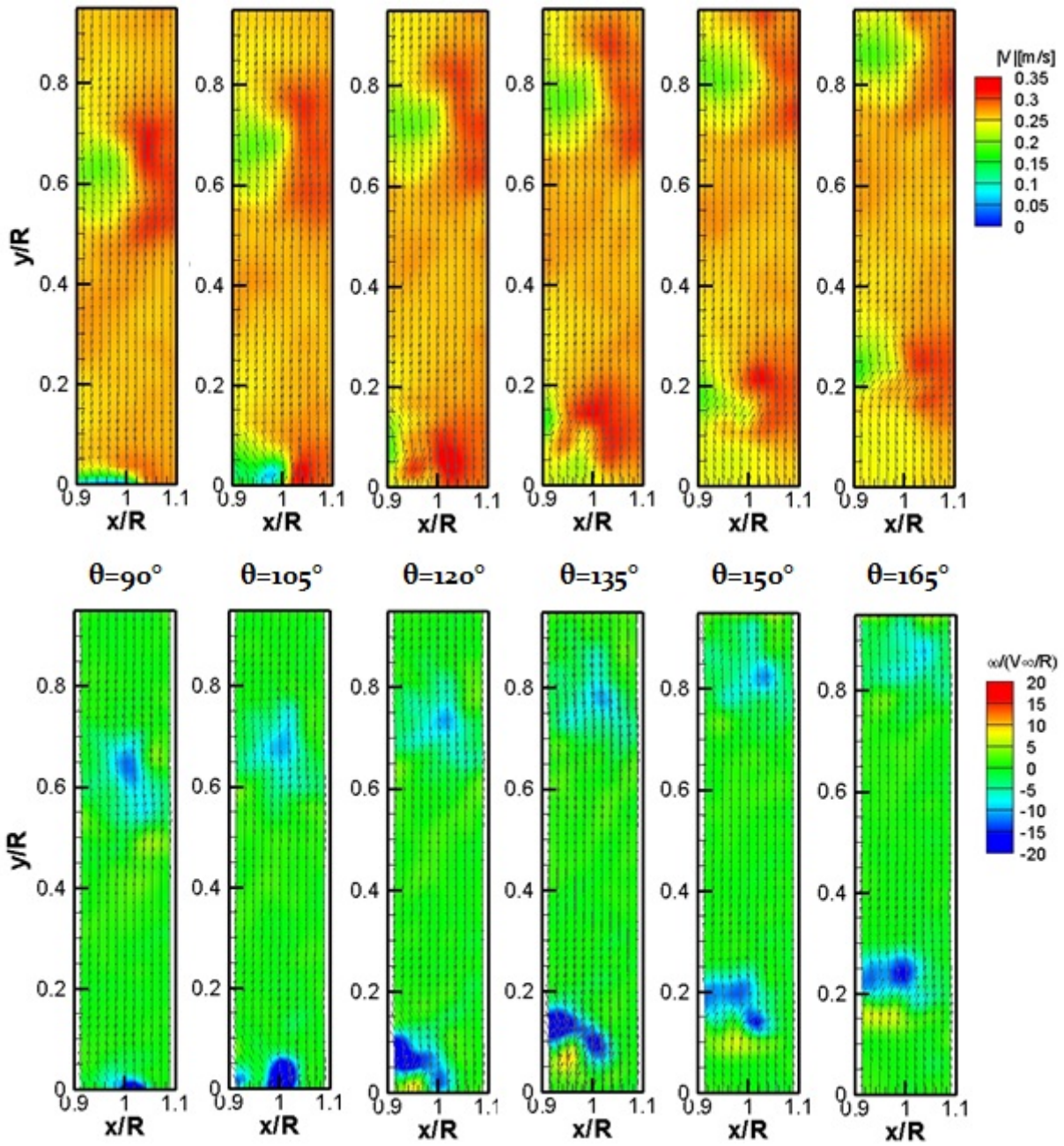

Figure 6.8: Velocity and vorticity fields downstream of the rotor.

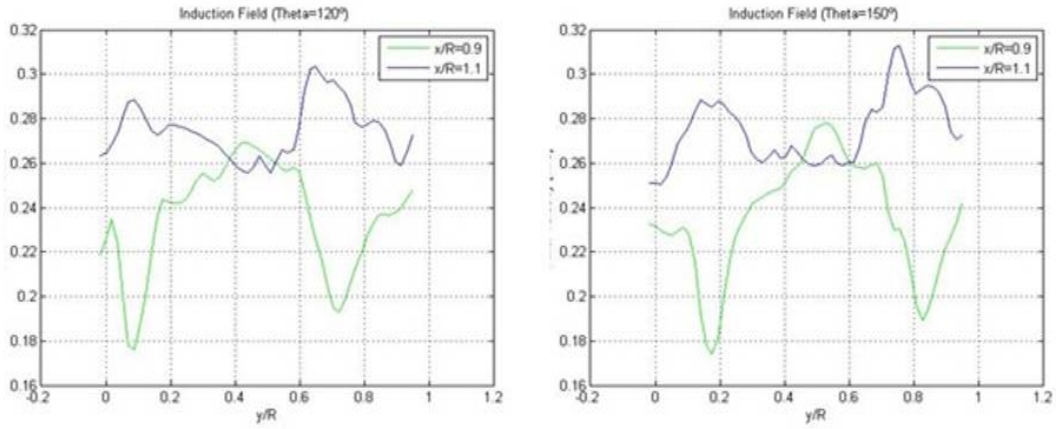

Figure 6.9: Axial velocity downstream of the rotor.

flow in the upper surface of the airfoil is accelerated (it reaches up to 0.55m/s) producing a lower pressures on the airfoil, and the opposite occurs in the lower surface of the airfoil; the velocity is decreased (up to 0.15m/s) originating bigger pressures.

The right column of Figure 6.14 shows the instantaneous iso-vorticity contour around the GOE531 at $355° \leq \theta \leq 5°$. The airfoil is shedding vortices of counteracting direction of rotation, alternately, due to the interaction and roll-up of the two shear layers of opposing vorticity separating from the upper and lower airfoil surfaces near the trailing edge. The high camber of the airfoil chosen induces the separation of the boundary layer near the trailing edge. This vorticity pattern can also be appreciated in the velocity field in the left column. The vorticity shed by an airfoil was studied through PIV by Lee *et al.* (2008).

Figure 6.15 shows the axial and tangential velocity measured along the streamwise direction (y axis) of the flow, when the blade has not yet reached the position where the velocities are being measured ($\theta = 355°$), and when the blade is exactly in this position ($\theta = 0°$).

The blue line is depicting axial velocity streamwise (that is, along the y-axis). For $\theta = 0°$, it decreases as the flow approaches the rotor, and increases considerably just after the rotor plane, due to the fact that the airfoil is located in this position and it is producing lift, so that the velocity is increased in the upper surface.

The green line is depicting tangential velocity in the same location. For $\theta = 0°$, the tangential velocity diminishes as z decreases, which means that the airfoil is impinging a tangential velocity in the inverse direction of the blade rotation, so that the wake will rotate in the opposite direction of the turbine. In the areas near the blade, the tangential velocity diminishes drastically, but it stabilizes between values $-0.08 \leq V_t \leq -0.01$, which would be equal to a tangential velocity induction factor $0.08 \leq a' \leq 0.1$; values that are slightly superior to BEM predictions ($a' \sim 0.05$).

6.5 Conclusions

In this research study the near wake of a horizontal axis wind turbine was visualized and characterized. The results obtained make up a good contribution to the experimental database available that may be used to validate numerical codes and compose an improved

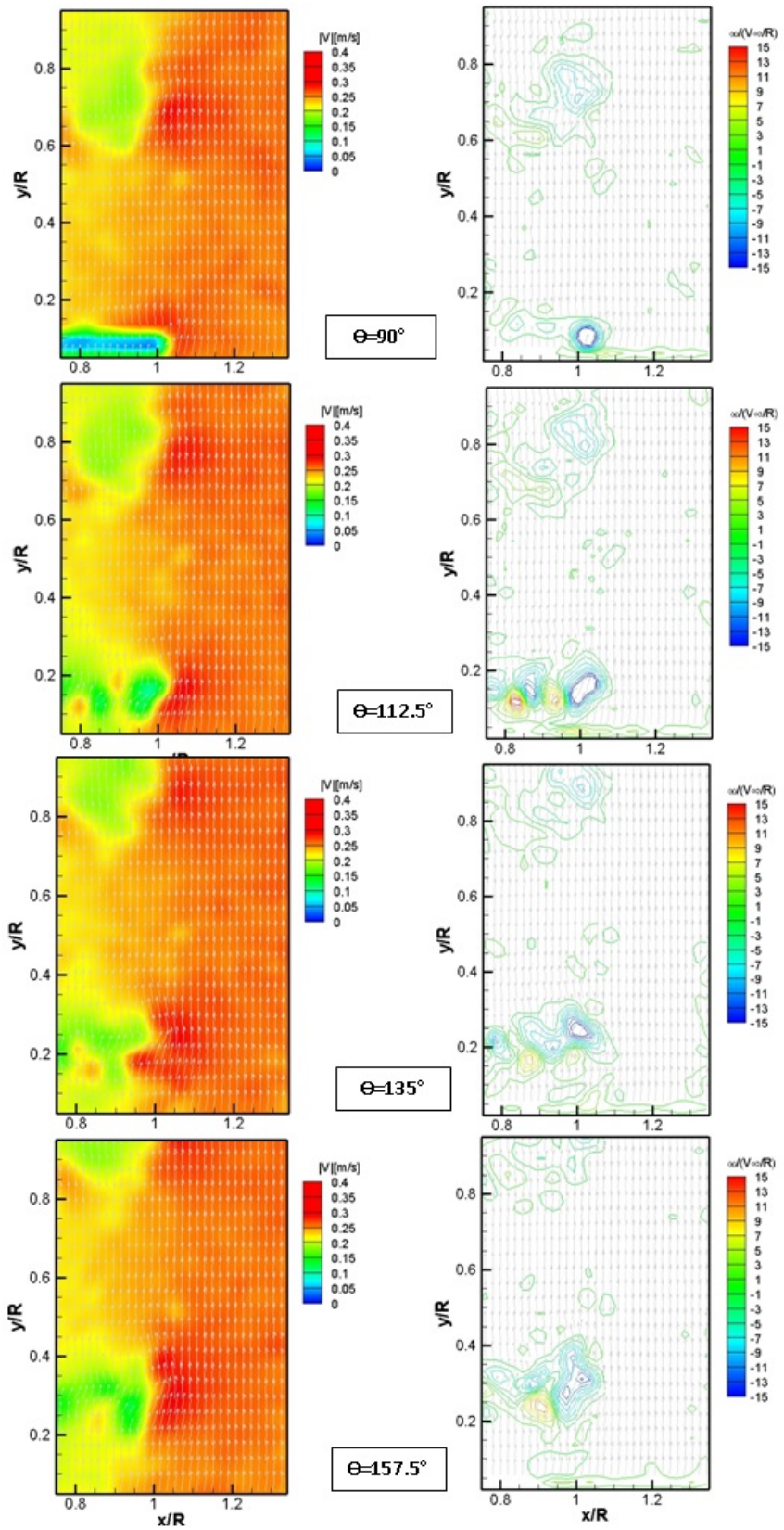

Figure 6.10: Velocity field and iso-vorticity contour downstream of the rotor.

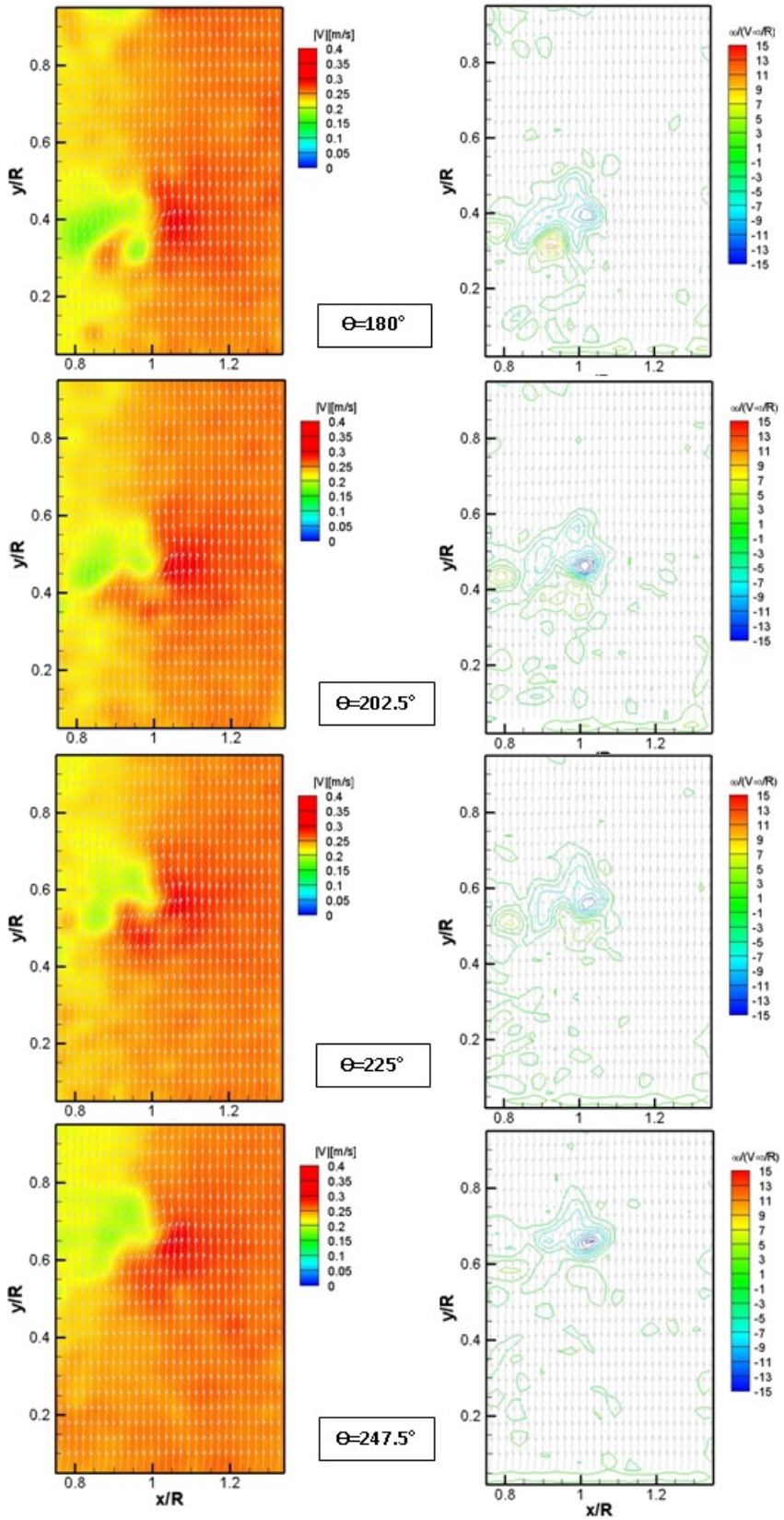

Figure 6.11: Velocity field and iso-vorticity contour downstream of the rotor *(continued)*.

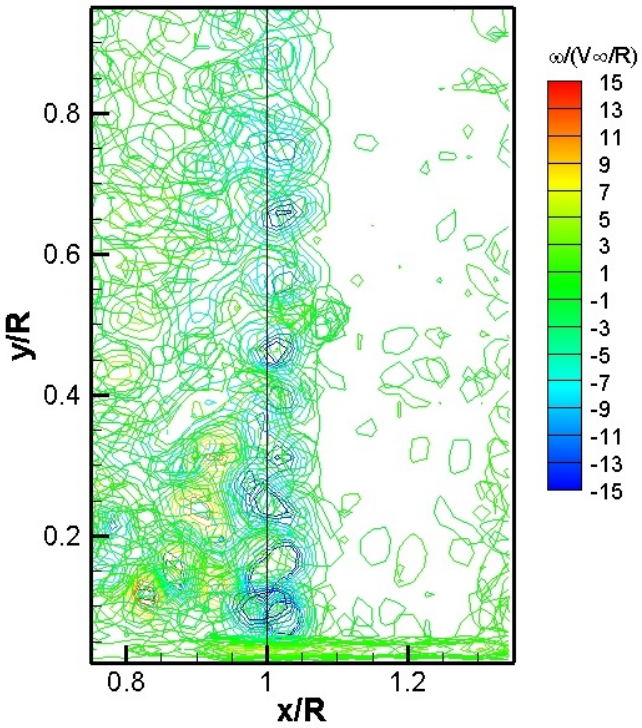

Figure 6.12: Juxtaposition of iso-vorticity curves ($90° \leq \theta \leq 247°$).

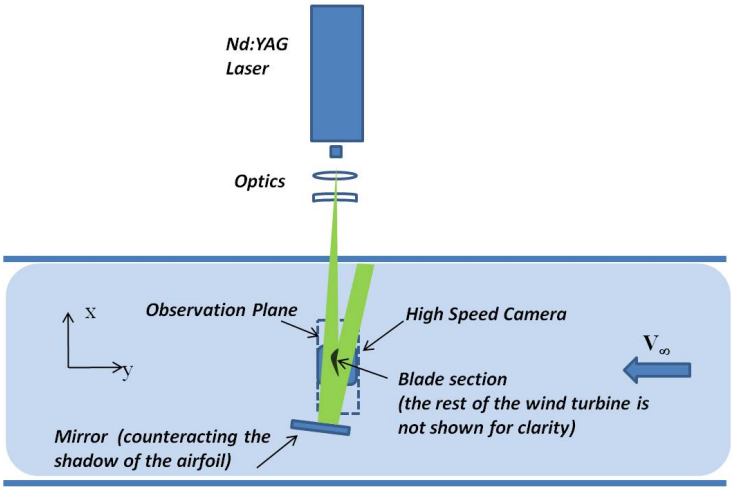

Figure 6.13: Scheme of the blade element visualization experimental set up.

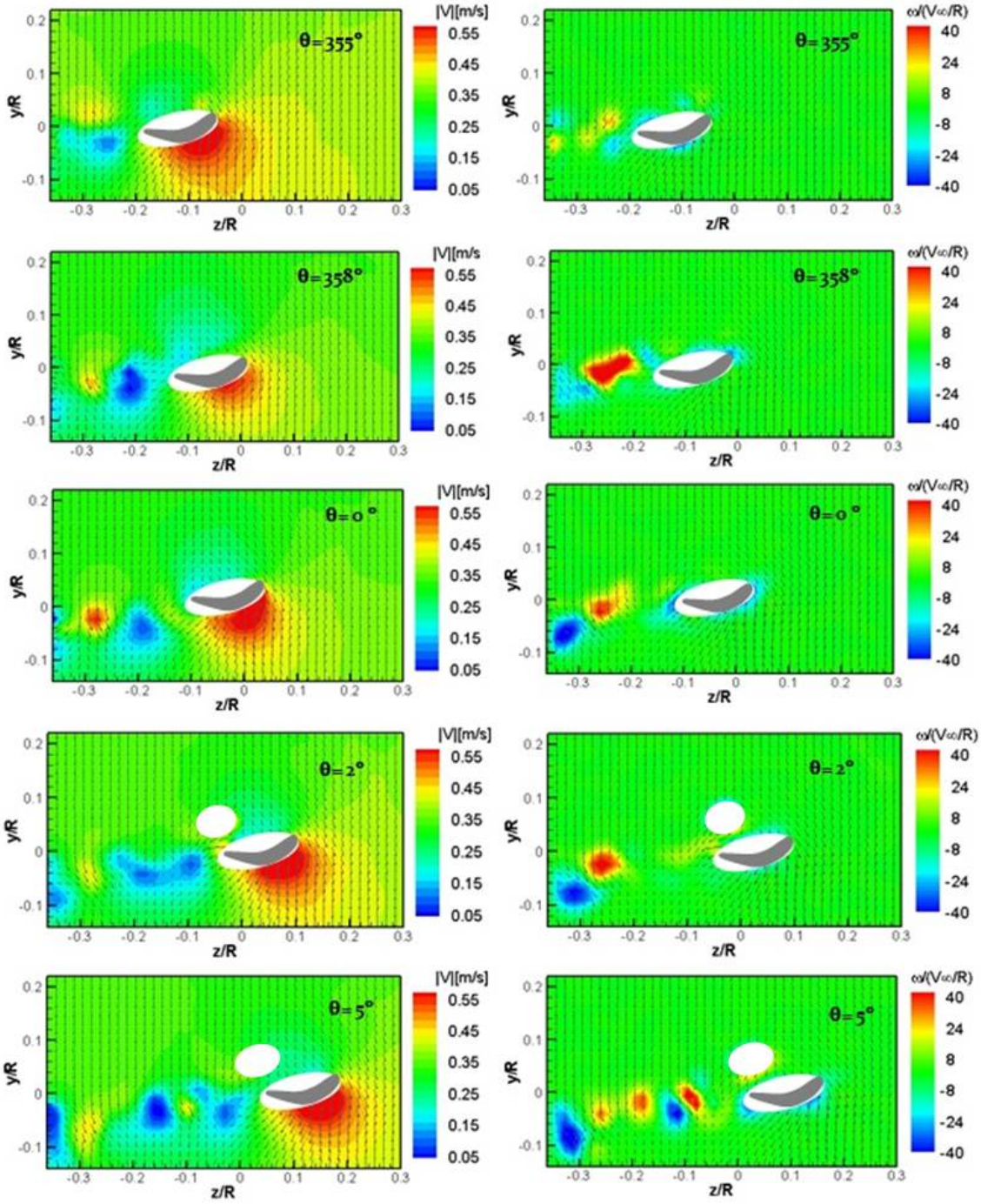

Figure 6.14: Velocity field *(left)* and vorticity field *(right)* around a rotating blade element situated at the midspan of the blade, $x/R = 0.5$, for different azimuthal positions of the blade.

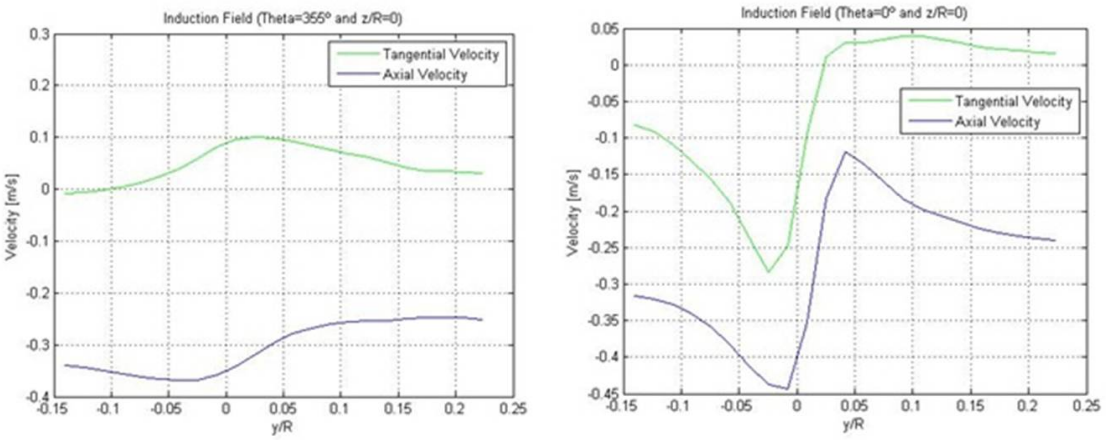

$\theta = 355°$ $\theta = 0°$

Figure 6.15: Axial and tangential velocity for z/R = 0 along the streamwise direction.

theoretical model that predict the performance of a HAWT.

The experiments were done at low Reynolds number conditions Re $\sim 10000 - 18000$ and tip speed ratio TSR $\sim 4 - 5$, in a water tunnel with 0.25m/s free stream velocity, on a two blade rotor model of 38cm of diameter. PIV and TRPIV techniques were used in order to visualize and compute the velocity and vorticity fields in the near wake of the rotor model.

The study focused on areas where current wake modeling requires more attention, in particular, the characterization of the trailing tip vortex spiral, particularly interesting for the load prediction on the rotor blades. The results gave a good concordance with previous publications. The pitch of the helical tip vortex ranged between $1.2R$ and $1.3R$ and there was no substantial expansion of the wake (less than 0.1radius in a distance of one diameter). The normalized strength of the vorticity and the velocity field were also calculated.

Axial and tangential velocities measured in the near wake and across the rotor were in good agreement with data available in the literature, and in good qualitative agreement with the theory predictions. However, values obtained via BEM were slightly different: the fact that BEM theory assumes frictionless flow and that the aerodynamics coefficients available for the airfoil used are based on Re $= 25,000$ may explain these differences.

In addition, the whole velocity and vorticity fields around a rotating blade element situated at mid-span of the blade was resolved by means of TRPIV. Hereby, generating a basis to evaluate the resulting forces through the Momentum Equation and link the concepts of unsteady loading and shed vorticity.

Chapter 7

Conclusions

7.1 Contributions to the State of the Art

The main contributions of this research work, to the experimental study of the aerodynamics of wind turbines, and in particular, to the estimation of loads via PIV and its application to a Horizontal Axis Wind Turbine (HAWT) blade were:

Chapter 2

- Overview of the different existing methods to describe and predict, numerically, the aerodynamics of wind turbine.
- Summary of the fundamental concepts in which the Blade Element and Momentum is based.

Chapter 3

- Brief description of the basic aspects related with Particle Image Velocimetry (PIV), in particular those which are more relevant in order to undertake an experimental campaign.
- Detailed explanation of the Momentum Equation contour-based approach used to calculate loads out of PIV velocities (PIV-Loads method).
- Numerical validation of the PIV-Loads method, by means of Direct Numerical Simulation data. The comparison of results was done for two different test cases:
  - Unsteady, laminar flow around a circular cylinder, Re =200.
  - Flow around an inclined flat plate, Re = 10,000, where the boundary layer is disattached and forms a turbulent wake.

Chapter 4

- PIV visualization of the velocity and the vorticity fields around an inclined flat plate, for different angles of attack and Re = 30,000-120,000.
- Pressure reconstruction using a pressure Poisson solver.

- 2D calculation of lift and drag using PIV velocities, and comparison of results with those provided by a high sensitive balance.

Chapter 5

- SPIV visualization of the cross sectional velocity fields along a HAWT blade, operating both in axial and yawed flow conditions, with tip Re = 275,000.
- Pressure reconstruction around the blade, using a pressure Poisson solver.
- 3D calculation of normal and tangential forces using SPIV velocities, and comparison of the results with those obtained through a numerical panel method model.

Chapter 6

- TRPIV visualization of the near vortex wake of a HAWT operating at low Reynolds number, i.e, tip Re = 16,000.
- Characterization of the velocity and vorticity fields present in the tip region, and in a cross sectional plane at midspan of the blade.

7.2 Discussion

In the beginning of the dissertation, it was decided to offer a brief overview of the BEM theory and its limitations, since it represents a good way of introducing the basic concepts of the aerodynamics of a wind turbine. Besides, this theory was used to design the two scaled-down turbine models constructed for this project, and served as means of checking the consistency, at a first stage, of the results obtained experimentally.

One of the main goals of this research project was to consolidate the feasibility of measuring the forces, impinged by the flow on a body, out of PIV velocities. The methodology consisted in a ME contour-based formulation, combined with a pressure Poisson solver. As a first step, this PIV-Loads approach was validated using DNS data, that reproduced the unsteady laminar flow around a circular cylinder (Re = 200), and the flow around an inclined flat plate (Re = 10,000) that formed a turbulent wake. DNS data that had been resampled to match the resolution of a conventional PIV system.

The pressure and force results, calculated out of PIV velocities, showed very close agreement with those provided by DNS. The results concluded that, having accurate velocity data, well resolved along all the field, the PIV-Loads methodology offers a reliable way of measuring forces, independent of the integration path chosen. Nevertheless, results were slightly more accurate if the integration path avoided the area close to the boundary layer (in the case of the cylinder) or the area crossing the turbulent shear layer (in the case of the flat plate).

Regarding the influence of the different terms inside the ME for both test cases, it was observed that convective terms were the most important contributors, followed by Reynolds stress terms (in the case of turbulent flow), whereas viscous terms had a very small influence.

Once the methodology and its implementation had been validated with DNS data, the first experimental campaign was undertaken with the aim of proving the feasibility of measuring lift and drag in an inclined flat plate out of real 2D-PIV velocities ($Re = 30,000 - 120,000$). Simultaneously, these aerodynamic forces were measured with a high sensitive balance. The calculated results showed good consistency with those provided by the balance, although the differences encountered were bigger than those found in the DNS validation.

These differences were mainly due to PIV uncertainties (lack of resolution, velocity gradients inside the interrogation window chosen, and laser reflections). Thus, the biggest disagreements were encountered calculating drag, specially when dealing with higher angles of attack. Theses cases were directly connected with the turbulent wake, where velocity gradients were higher and not completely captured by the available PIV system.

In addition, the study provided with means for characterizing the stalling conditions of the flat plate and its vorticity shedding, at different Re and angles of attack. The results were contrasted with DNS data, RANS data and existing literature experimental data. The flat plate flow disattachement started near the trailing edge and expanded towards the leading edge with increasing angle of attack. For fully separated flow, vortices started to come off the leading edge with a frequency of f = 350Hz.

At last, after having measured forces out of PIV velocities in a stationary, bidimensional problem, the next step was to calculate the forces impinged on a wind turbine with a similar methodology; goal that, at the end of the day, had been the Leitmotiv all throughout this research project. Therefore, phase-locked sectional SPIV velocity fields were acquired along the blade of a HAWT operating both in axial and in yawed flow (Re = 275,000). Normal and tangential forces were calculated with the same PIV-Loads methodology, this time using 3D formulation.

In the case of axial flow conditions, a non inertial moving frame of reference was considered for the formulation. The convenience of this election lied on the azimuthal symmetry of the flow around the rotating blade, which allowed to use an steady formulation. The results showed very good consistency with those provided by a panel code implementation: regarding lift, there was a small offset near the tip region, and for the rest, the curve tendencies were in close agreement. On the other hand, tangential force values results had good consistency with the panel code ones, although the curve tendency was less smooth.

Moreover, in the case of yawed flow conditions, it was proved that using a stationary frame of reference was more convenient for this case, where unsteadiness of the flow had to be considered, irrespective of the frame of reference chosen. Due to laser reflections near the model and lack of resolution in the wake, the volume integral associated to the unsteady terms introduced large errors in the final results. In order to avoid these errors, a derivative-moment transformation (DMT) was introduced in the formulation, converting the volume integral into a surface integral, and providing a less error-prone methodology. Final results using a stationary frame of reference together with DMT found good consistency with those provided by the panel code.

In conclusion, a new way of measuring aerodynamic loads with a non intrusive technique on a wind turbine has been provided. It allows to experimentally measure forces without the need of pressure taps, which are complicated to implement and, in some cases where the model is small, unfeasible. Also, the method provides with consistent pressure fields around the blade together with a complete insight of the velocity field around the airfoil. Main problems encountered are due to PIV uncertainties such as peak locking, lack of

spatial resolution in the wake region, and laser reflections.

Finally, the near vortex wake of a HAWT operating at low Reynolds (Re = 18,000) was visualized via TRPIV. The study focused on areas where current wake modeling requires more attention, in particular, the characterization of the trailing tip vortex, specially interesting for the load prediction on the rotor blades. The results gave a good concordance with previous publications: axial and tangential velocities measured in the near wake and across the rotor were in good agreement with data available in the literature. However, values obtained via BEM were slightly different: the simplifications assumed by this theory and the fact that the aerodynamics coefficients available were based on a slight different Re, may explain these differences. In addition, the whole velocity and vorticity fields around a rotating blade element situated at mid-span of the blade was resolved by means of TRPIV.

7.3 Recommendations on Future Work

With this dissertation, the feasibility of estimating forces on a wind turbine with a non intrusive technique has been demonstrated, both for axial and yaw cases. However, as has just been discussed, uncertainties due to PIV such as peak loacking, laser reflections or lack of resolution, represent the major drawback when computing forces out of PIV velocities. Therefore, any future improvements in this direction would certainly lead to a more reliable implementation of the method.

The technique could be used to test the efficiency of active load control methods, or to study rotational effects. Besides, it would be interesting to check its efficiency in a blade that undergoes stall. Moreover, in the future, it could be used together with Light Detection And Ranging (LIDAR) velocities, instead of PIV velocities, and thus bring load information of the HAWT in its real working conditions.

Finally, it would be interesting to use this methodology in order to deeper investigate the relation between shed vorticity and unsteady loading.

Bibliography

[1] R. J. Adrian. Twenty years of particle image velocimetry. *Experiments in Fluids*, 39(2), 2005.

[2] T. Albrecht, F Marlow, H Metzkes, and J Stiller. DNS and LES of separation control using oscillating lorentz forces. *Proceedings of the 6th International Conference on Electromagnetic Processing of Materials*, 2009.

[3] T. Albrecht and J. Stiller. Control of separated flow using an oscillating lorentz force: Comparison of DNS, LES, and experiments. *Progress in Turbulence III*, page 247_250, 2009.

[4] T. Albrecht, T. Weier, G. Gerbeth, H. Metzkes, and J. Stiller. A method to estimate the planar, instantaneous body force distribution from velocity field measurements. *Physics of Fluids*, 23:021702, 2011.

[5] J.D. Anderson. *Fundamentals of aerodynamics*. McGraw-Hill New York, 2001.

[6] A. Betz. *Schraubenpropeller mit geringstem Energieverlust*. Gottinger Nachr., 1919.

[7] H. M. Blackburn and S. J. Sherwin. Formulation of a galerkin spectral element fourier method for three dimensional incompressible flows in cylindrical geometries. *Journal of Computational Physics*, 197(2):759_778, 2004.

[8] T. Burton, D. Sharpe, N. Jenkins, and E. Bossanyi. *Wind energy: handbook*. Wiley Online Library, 2001.

[9] J. M. Chen and Y. C. Fang. Strouhal numbers of inclined flat plates. *Journal of wind engineering and industrial aerodynamics*, 61(2):99â112, 1996.

[10] R. de Kat, B.W. van Oudheusden, and F. Scarano. Instantaneous planar pressure field determination around a square-section cylinder based on time-resolved stereo-PIV. In *14 th International Symposium on Applications of Laser Techniques to Fluid Mechanics, Lisbon, Portugal*, 2008.

[11] K. Dixon. The near wake structure of a vertical axis wind turbine. *Master Thesis, TUDelft*, 2008.

[12] The European Wind Energy Association EWEA. *Wind Energ: The Facts. A guide to the technology, economics and future of wind power*. Earthscan, 2009.

[13] A. Fage and F. C. Johansen. On the flow of air behind an inclined flat plate of infinite span. *Proceedings of the Royal Society of London. Series A, Containing Papers of a Mathematical and Physical Character*, 116(773):170â197, 1927.

[14] S. Franchini and O. Lopez Alegria. *Introduccion a la ingenieria aeroespacial.* IDR. 2nd edition, 2011.

[15] N. Fujisawa, Y. Nakamura, F. Matsuura, and Y. Sato. Pressure field evaluation in microchannel junction flows through muPIV measurement. *Microfluidics and Nanofluidics*, 2(5):447_453, 2006.

[16] I. Grant, X. Pan, M. Mo, P. Parkin, J. Powell, H. Reinecke, K. Shuang, F. Coton, and D. Lee. An experimental and numerical study of the vortex filaments in the wake of an operational horizontal axis wind turbine. *Journal of wind engineering and industrial aerodynamics*, 2000.

[17] P. Guiguere and M.S. Selig. Design of a tapered and twisted blade for the NREL combined experiment rotor. *NREL Documentation*, 1999.

[18] W. Haans, T. Sant, G. van Kuik, and G. van Bussel. HAWT near-wake aerodynamics, part i: axial flow conditions. *Wind Energy*, 11(3):245_264, 2008.

[19] R. Hain, C. J. Kahler, and C. Tropea. Comparison of CCD, CMOS and intensified cameras. *Experiments in fluids*, 42(3):403_411, 2007.

[20] M. O. L. Hansen. *Aerodynamics of wind turbines.* Earthscan/James & James, 2008.

[21] H. Hirahara, M.Z. Hossain, M. Kawahashi, and Y. Nonomura. Testing basic performance of a very small wind turbine designed for multi-purposes. *Renewable Energy*, 2007.

[22] T. Jardin, L. Chatellier, A. Farcy, and L. David. Correlation between vortex structures and unsteady loads for flapping motion in hover. *Experiments in fluids*, 47(4):655_664, 2009.

[23] T. Jardin, L. David, and A. Farcy. Characterization of vortical structures and loads based on time resolved PIV for asymmetric hovering flapping flight. *Experiments in fluids*, 46(5):847_857, 2009.

[24] B. M. Jones. Measurement of profile drag by the pitot traverse method. *ARC R&M*, 1688, 1936.

[25] J. Katz and A. Plotkin. *Low speed aerodynamics.* Cambridge University Press, 2001.

[26] R. D. Keane and R. J. Adrian. Theory of cross-correlation analysis of PIV images. *Applied scientific research*, 49(3):191_215, 1992.

[27] D. F. Kurtulus, F. Scarano, and L. David. Unsteady aerodynamic forces estimation on a square cylinder by TR-PIV. *Experiments in fluids*, 42(2):185_196, 2007.

[28] M. Lara, D. Del Campo, and V. Del Campo. Estudio de metodos no intrusivos de determinaacion de cargas aerodinamicas sobre perfiles mediante CFD. Technical report, 2011.

[29] Tim Lee and L. S. Ko. PIV investigation of flowfield behind perforated gurney-type flaps. *Experimental Fluids*, 2008.

[30] J. Lighthill. Fundamentals concerning wave loading on offshore structures. *Journal of Fluid Mechanics*, 173(667_681):71, 1986.

[31] J. C. Lin and D. Rockwell. Force identification by vorticity fields: techniques based on flow imaging. *Journal of fluids and structures*, 10(6):663_668, 1996.

[32] X. Liu and J. Katz. Instantaneous pressure and material acceleration measurements using a four-exposure PIV system. *Experiments in fluids*, 41(2):227_240, 2006.

[33] F. Massouh and I. Dobrev. Exploration of the vortex wake behind of a wind turbine rotor. *Journal of Physics*, 2007.

[34] G. B. McCullough and D. E. Gault. *Examples of three representative types of airfoil-section stall at low speed.* National Advisory Committee for Aeronautics, 1951.

[35] J. Meseguer Ruiz and A. Sanz Andres. *Aerodinamica basica.* 2005.

[36] D. Micallef, M. Kloosterman, C. Ferreira, T. Sant, and G. J. W. van Bussel. Validating BEM, direct and inverse free wake models with the MEXICO experiment. In *Wind Energy Symposium Paper AIAA_2010_0462*, 2010.

[37] A. Mohebbian and D. E. Rival. Assessment of the derivative-moment transformation method for unsteady-load estimation. *Experiments in fluids*, page 1_12, 2012.

[38] F. Noca, D. Shiels, and D. Jeon. A comparison of methods for evaluating time-dependent fluid dynamic forces on bodies, using only velocity fields and their derivatives. *Journal of Fluids and Structures*, 13(5):551_578, 1999.

[39] J. Nogueira, A. Lecuona, and P. A. Rodriguez. Limits on the resolution of correlation PIV iterative methods. fundamentals. *Experiments in fluids*, 39(2):305_313, 2005.

[40] M. Raffel, C.E. Willert, and J. Kompenhans. *Particle image velocimetry: a practical guide.* Springer Verlag, 1998.

[41] D. Ragni, A. Ashok, B. W. van Oudheusden, and F. Scarano. Surface pressure and aerodynamic loads determination of a transonic airfoil based on particle image velocimetry. *Measurement Science and Technology*, 20:074005, 2009.

[42] D. Ragni, B. W. van Oudheusden, and F. Scarano. Non intrusive aerodynamic loads analysis of an aircraft propeller blade. *Experiments in fluids*, 51(2):361_371, 2011.

[43] D. Ragni, BW van Oudheusden, and F. Scarano. 3D pressure imaging of an aircraft propeller blade-tip flow by phase-locked stereoscopic PIV. *Experiments in fluids*, 52(2):463_477, 2012.

[44] F. Scarano and M. L. Riethmuller. Advances in iterative multigrid PIV image processing. *Experiments in Fluids*, 29:51_60, 2000.

[45] H. Schlichting and K. Gersten. *Boundary-layer theory.* Springer Verlag, 2000.

[46] S. Schreck and M. Robinson. Wind turbine blade flow fields and prospects for active aerodynamic control. In *Conference Paper NREL/CP_500_41606, August*, 2007.

[47] S. Schreck, T. Sant, and D. Micallef. Rotational augmentation disparities in the MEXICO and UAE phase VI experiments. In *3rd Torque 2010 The Science of making Torque from Wind Conference,(FORTH, Heraklion, Crete, Greece)*, 2010.

[48] F. J. Schrijer and F. Scarano. Effect of predictor corrector filtering on the stability and spatial resolution of iterative PIV interrogation. *Experiments in fluids*, 45(5):927_941, 2008.

[49] C. J. Simao Ferreira. *The near wake of the VAWT: 2D and 3D views of the VAWT aerodynamics*. PhD thesis, TUDelft, 2009.

[50] H. Snel, J G Schepers, and B. Montgomerie. The MEXICO project (model experiments in controlled conditions): The database and first results of data processing and interpretation. *Journal of Physics*, 2007.

[51] J. L. Tangler. Nebulous art of using wind tunnel airfoil data for predicting rotor performance. *ASME Wind energy conference*, 2002.

[52] M. F. Unal, J. C. Lin, and D. Rockwell. Force prediction by PIV imaging: a momentum based approach. *Journal of Fluids and Structures*, 11(8):965_971, 1997.

[53] H. C. van de Hulst. *Light scattering by small particles*. Dover publications, 1981.

[54] G. van Kuik, B. Ummels, and R. Hendriks. Perspectives of wind energy. *Europe*, 50(60):70, 2006.

[55] B. W. Van Oudheusden. Principles and application of velocimetry-based planar pressure imaging in compressible flows with shocks. *Experiments in fluids*, 45(4):657â674, 2008.

[56] B. W. Van Oudheusden, F. Scarano, and E.W.F. Casimiri. Non-intrusive load characterization of an airfoil using PIV. *Experiments in fluids*, 40(6):988_992, 2006.

[57] B. W. van Oudheusden, F. Scarano, E.W.M. Roosenboom, E.W.F. Casimiri, and L.J. Souverein. Evaluation of integral forces and pressure fields from planar velocimetry data for incompressible and compressible flows. *Experiments in Fluids*, 43(2):153_162, 2007.

[58] L. J. Vermeer, J. N. Sorensen, and A. Crespo. Wind turbine aerodynamics. *Progress in Aerospace Sciences*, 2003.

[59] D. Violato, P. Moore, and F. Scarano. Lagrangian and eulerian pressure field evaluation of rod airfoil flow from time-resolved tomographic PIV. *Experiments in fluids*, 50(4):1057_1070, 2011.

[60] J. Whale, C. G. Anderson, R. Bareiss, and S. Wagner. An experimental and numerical study of the vortex structure in the wake of a wind turbine. *Journal of Wind Engineering and Industrial Aerodynamics*, 84(1):1_21, 2000.

[61] F. M. White. *Fluid mechanics*. McGraw-Hill Inc, 1994.

[62] J. Z. Wu, Z. L. Pan, and X. Y. Lu. Unsteady fluid dynamic force solely in terms of control-surface integral. *Physics of Fluids*, 17:098102, 2005.

[63] J. Xiao, J. Wu, L. Chen, and Z. Shi. Particle image velocimetry (PIV) measurements of tip vortex wake structure of wind turbine. *Applied Mathematics and Mechanics*, 32(6):729_738, 2011.